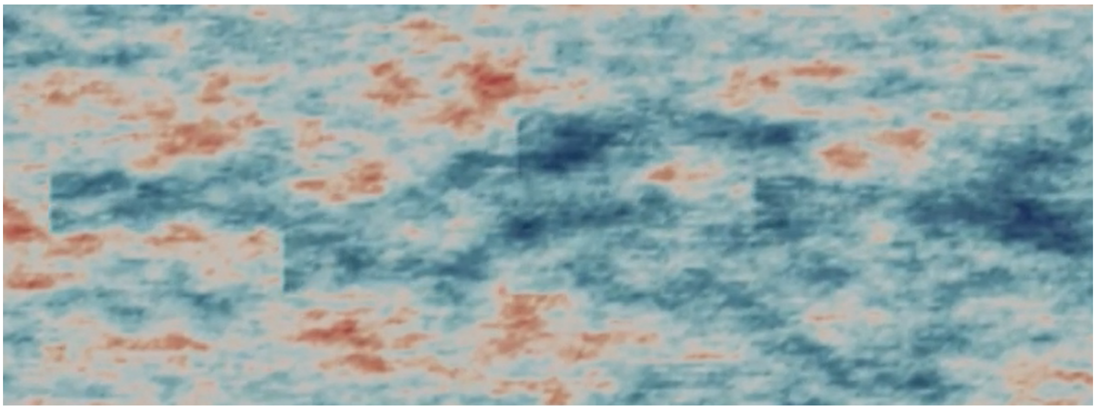

# Offshore floating wind farms cost reduction assessment

**Jakub Grzegorz Strąg**

Thesis to obtain the Master of Science Degree in

## Energy Engineering and Management

| | |
|---|---|
| Supervisors: | Dr. Juan Carlos Chong Portillo |
| | Prof. Luís Manuel de Carvalho Gato |

### Examination Committee

| | |
|---|---|
| Chairperson: | Prof. Luís Filipe Moreira Mendes |
| Supervisor: | Dr. Juan Carlos Chong Portillo |
| Member of the Committee: | Prof. Ricardo Balbino Santos Pereira |

**December 2022**

# Declaration

I declare that this document is an original work of my own authorship and that it fulfills all the requirements of the Code of Conduct and Good Practices of the Universidade de Lisboa.

## Acknowledgements

I would like to express my sincere gratitude to Prof. Juan Portillo for continuous and extensive help throughout the thesis development and for suggesting the topic of this work. Thank you for your time, dedication and constant availability. Your enthusiastic and very professional attitude made the whole thesis preparation process enjoyable.

Thank you to Prof. Luís Gato for the possibility of writing the thesis and for the supervision of my work.

Thank you to Prof. Tadeusz Olkuski for being my supervisor at AGH University of Science and Technology in Poland.

I cannot express my appreciation enough to my parents Anna and Grzegorz, and my grandparents Adam and Lucyna for being there for me and providing me with immeasurable help and encouragement. Thank you for planting the seeds of curiosity and persistence in me and helping them grow throughout all of these years. I am sure you will always be there for me.

Thank you to EIT InnoEnergy Master's School for giving me this unique opportunity and to all of the people I have met during the program for making this experience unforgettable.

# Abstract

The need for a faster energy transition towards a carbon-neutral society has accelerated the support and development of offshore floating wind technologies. However, the necessity for cost reductions to make offshore energy projects viable and more attractive to developers require further research on new strategies for wind farm cost reductions and performance enhancements. The main objective of this work is to evaluate techno-economically some of these strategies. The goals of this work were achieved through aero-hydro-servo-elastic numerical simulations and cost-modelling of twenty-five different wind farm case studies, considering variations in turbine spacing distances, turbine hub heights, farm layouts and the floating platform size. The main farm evaluation factors addressed in this work are the annual electricity production, farm energy losses due to the wake effects, farm capacity factor, the levelized cost of energy (LCOE) and an energy yield density factor that is introduced in this thesis. Based on this study, it can be noticed that turbine hub height variations do not necessarily show promising LCOE reductions due to lower wind resources and insignificant cost reductions. The platform size reduction was estimated to have a low impact on the wind farm LCOE. Different wind farm layouts, on the other hand, can significantly decrease the wake losses and the LCOE by up to 17.2%. This study provides a good base for further techno-economic analysis of different wind farm configurations, including the wind turbine row spacing, turbine hub heights and wind farm layouts. It also presents recommendations for cost-reduction analysis tools and methodologies.

**Keywords:** Offshore wind energy, floating offshore wind turbines, LCOE, techno-economic assessment, cost reductions, wake effects

# Resumo

A necessidade de uma transição energética mais rápida para uma sociedade neutra em carbono tem acelerado o apoio e o desenvolvimento de tecnologias eólicas flutuantes offshore. No entanto, a necessidade de reduções de custos para tornar os projetos de energia offshore viáveis para os promotores requer mais investigação sobre novas estratégias para a redução dos custos dos parques eólicos. O principal objetivo deste trabalho é avaliar tecno-economicamente algumas destas estratégias. Os objetivos deste trabalho foram alcançados através de simulações numéricas aero-hidro-servo-elásticas e de custos de vinte e cinco estudos de caso de parques eólicos flutuantes, considerando variações nas distâncias de separação das turbinas, alturas das mesmas, e disposições espaciais dos aerogeradores, assim como o tamanho da plataforma flutuante. Os principais fatores de avaliação dos parques eólicos considerados neste trabalho são a produção anual de energia, as perdas associadas às esteiras dentro do parque eólico, o *fator de capacidade*, o *custo nivelado da energia* (LCOE), e o fator de densidade do rendimento energético. Os resultados evidenciam que as variações de alturas das turbinas não mostram reduções promissoras de LCOE. Estimou-se que a redução do tamanho da plataforma tenha um baixo impacto no LCOE do parque eólico. Porém, diferentes disposições das turbinas em parques eólicos podem diminuir significativamente as perdas associadas às esteiras e o LCOE até 17.2%. Este estudo fornece uma boa base para uma análise técnico-económica mais aprofundada de diferentes configurações de parques eólicos. Este trabalho apresenta recomendações sobre as ferramentas e metodologias para a análise de redução de custos.

**Palavras-Chave:** Energia eólica offshore, turbinas eólicas flutuantes, LCOE, avaliação técnico-economica, redução de custos, efeitos de esteiras

# Contents

**Contents** xi

**List of Figures** xv

**List of Tables** xvii

**Nomenclature** xxiii

**1 Introduction** 1
- 1.1 Motivation . . . 1
- 1.2 Objective . . . 2
- 1.3 Methodologies and limitations . . . 3
- 1.4 Structure of the thesis . . . 4

**2 Theoretical Background and state-of-the-art** 5
- 2.1 Offshore wind energy . . . 5
- 2.2 Offshore wind turbines . . . 6
- 2.3 Offshore structures for wind turbines . . . 6
  - 2.3.1 Bottom-fixed wind turbines . . . 7
  - 2.3.2 Floating wind turbines . . . 7
- 2.4 Offshore wind farms: Lifecycle and development process . . . 9
- 2.5 Offshore market outlook . . . 10
  - 2.5.1 Floating offshore wind markets . . . 10
  - 2.5.2 Floating offshore wind projects . . . 11
- 2.6 Costs of offshore wind farms . . . 12
  - 2.6.1 Levelized cost of energy . . . 12
  - 2.6.2 LCOE for floating offshore wind . . . 12
  - 2.6.3 CAPEX, OPEX, and DECEX of FOW projects . . . 12
- 2.7 Cost reduction of floating offshore wind farms . . . 13
  - 2.7.1 Cost reduction factors . . . 14
  - 2.7.2 Wind farm layout . . . 16
  - 2.7.3 Tower hub height . . . 17

2.7.4 Floating platform cost reduction . . . . . . . . . . 17
2.8 Blade element momentum theory . . . . . . . . . . 18
2.9 Wake models used for farms' assessment . . . . . . . . . . 20
2.9.1 Jensen Wake Model . . . . . . . . . . 21
2.9.2 Jensen-2D_k Wake Model . . . . . . . . . . 21
2.9.3 Frandsen Wind Deficit Model . . . . . . . . . . 22
2.9.4 CFD-aided Wake Models . . . . . . . . . . 22
2.9.5 Larsen Wake Model . . . . . . . . . . 23
2.9.6 Dynamic Wake Meandering Model . . . . . . . . . . 23
2.10 Tools and software . . . . . . . . . . 24
2.10.1 OpenFAST . . . . . . . . . . 24
2.10.2 FAST.Farm . . . . . . . . . . 25
2.10.3 FAST.Farm wake dynamics (WD) model . . . . . . . . . . 25

**3 Description of the reference base case 27**
3.1 Floating platform . . . . . . . . . . 27
3.1.1 Platform mooring system . . . . . . . . . . 28
3.2 Wind turbine . . . . . . . . . . 28
3.3 Wind farm location . . . . . . . . . . 30
3.4 Wind and wave resource characterization . . . . . . . . . . 31
3.5 Wind farm layout . . . . . . . . . . 32

**4 Techno-economic assessment methodology 35**
4.1 FAST.Farm simulation description . . . . . . . . . . 38
4.1.1 Turbine and wind data interpolation domains placement . . . . . . . . . . 38
4.1.2 Simulation settings and results . . . . . . . . . . 39
4.2 Energy and wake losses calculation . . . . . . . . . . 39
4.3 Wind farm costs and LCOE calculation . . . . . . . . . . 40
4.3.1 Material CAPEX evaluation . . . . . . . . . . 41
4.3.2 Installation CAPEX . . . . . . . . . . 42
4.3.3 OPEX calculation methodology . . . . . . . . . . 43
4.3.4 DECEX calculation methodology . . . . . . . . . . 44
4.4 Wind farm evaluation factors . . . . . . . . . . 44

**5 Results and discussion 46**
5.1 Simulation cases description . . . . . . . . . . 46
5.2 Base case results . . . . . . . . . . 48
5.2.1 Power generation and energy yield results . . . . . . . . . . 48
5.2.2 Base case cost analysis . . . . . . . . . . 49
5.2.3 Base case LCOE values . . . . . . . . . . 52

5.3 Turbine spacing variations . . . . . . . . . . . . . . . . . . . . . . . . . . . . . . . . . . . . . . . 52
5.4 Turbine hub height variations . . . . . . . . . . . . . . . . . . . . . . . . . . . . . . . . . . . . . 54
    5.4.1 Hub height variations: Platform motions and tower base loads . . . . . . . . . . . 55
    5.4.2 Hub height variations: AEP and LCOE results . . . . . . . . . . . . . . . . . . . . . . 57
5.5 Wind farm layout variations . . . . . . . . . . . . . . . . . . . . . . . . . . . . . . . . . . . . . . 60
5.6 Floating platform size variations . . . . . . . . . . . . . . . . . . . . . . . . . . . . . . . . . . . 63
5.7 Results summary . . . . . . . . . . . . . . . . . . . . . . . . . . . . . . . . . . . . . . . . . . . . . 64

**6 Conclusions** **65**

**Bibliography** **69**

# List of Figures

2.1 Energy-related $CO_2$ emissions' (Gt $CO_2$/year) reduction forecast [9]. . . . . . . . . . . . . 6

2.2 Offshore wind turbines size and capacity development over the years [22]. . . . . . . . . . 7

2.3 Types of bottom-fixed and floating mounting systems used in offshore wind energy wind turbines. From the left: monopole, gravity-based, jacket, tripod, spar-buoy, semi-submersible, tension-leg [26]. . . . . . . . . . . . . . . . . . . . . . . . . . . . . . . . . . . . . . . . . . . 8

2.4 Lifecycle and development process of a wind farm [14]. . . . . . . . . . . . . . . . . . . . . 9

2.5 Cumulative installed capacity of floating offshore wind farms forecast based on already announced projects by 2026 [16]. . . . . . . . . . . . . . . . . . . . . . . . . . . . . . . . . . 11

2.6 Global LCOE forecasts for floating offshore wind energy projects [16]. . . . . . . . . . . . 13

2.7 CAPEX, OPEX and DECEX with their subcomponents for a floating offshore wind farm [44]. 14

2.8 Contribution of different cost components to LCOE for floating offshore wind reference farm operating for 25 years [47]. . . . . . . . . . . . . . . . . . . . . . . . . . . . . . . . . . . . 15

2.9 Wind turbines hub height optimization concept to reduce the wake effects [61]. . . . . . . 17

2.10 Blade element momentum theory [66]. The left picture shows the 1D streamtube used in the axial momentum theory, where: 1 is the far upstream location, 2 and 3 are placed at an infinitely small distance upstream and downstream from the disc, and 4 represents the far downstream location. The picture on the right presents the lift, drag, and velocity diagram of the blade element theory. . . . . . . . . . . . . . . . . . . . . . . . . . . . . . . . . . . 19

3.1 Design of the NREL semi-submersible platform with 5 MW NREL turbine. Left: Side-view overall design; right: Top view plan of the platform [88]. . . . . . . . . . . . . . . . . . . . . 28

3.2 Wind farm and the onshore substation location with its distance from the shore [91]. . . . 30

3.3 Chosen location's wind speed probability distribution with a fitted Weibull distribution function. 32

3.4 Proposed layout of the base case wind farm, where D is the turbine rotor diameter (D=126 m) and $y_D$ is the distance between rows measured in multiples of rotor diameter D. . . . . . . 33

3.5 A schematic diagram showing transmission system layout used in the wind farms simulated in this thesis. Prepared based on [99]. . . . . . . . . . . . . . . . . . . . . . . . . . . . . . . 34

4.1 Simulation and energy performance calculation methodology diagram. . . . . . . . . . . . 36

4.2 Cost model and LCOE calculation methodology diagram. . . . . . . . . . . . . . . . . . . . 37

4.3 Initial FAST.Farm turbine layout with low and high resolution domains defined. ”WT” stands for wind turbine; ”Low” stands for the low resolution domain boundary; and High-TX stands for high resolution domain for turbine X. . . . . . . . . . . . . . . . . . . . . . . . . . . 39

5.1 Diamond-2R wind farm layout case diagram. ”WT” stands for wind turbine; ”Low” stands for the low resolution domain boundary; and High-TX stands for high resolution domain for turbine X. . . . . . . . . . . . . . . . . . . . . . . . . . . . . . . . . . . . . . . . . 47
5.2 Dephased-2R wind farm layout case diagram. ”WT” stands for wind turbine; ”Low” stands for the low resolution domain boundary; and High-TX stands for high resolution domain for turbine X. . . . . . . . . . . . . . . . . . . . . . . . . . . . . . . . . . . . . . . . . 48
5.3 Base case wind turbine power simulations results. The left diagram shows the mean power generated by the first turbine (WT1) with the errorbars based on standard deviation. The right diagram shows the mean calculated values for every turbine. . . . . . . . . . . . . . 49
5.4 Base case wind turbine blade pitch and rotational speed results. The left diagram shows the mean rotational speed and the right one presented the first blade pitch of the first turbine (WT1) with the errorbars based on standard deviation. . . . . . . . . . . . . . . . . . . . 49
5.5 Base case total wind farm expenditures percentage shares estimated based upon the cost model in this thesis. . . . . . . . . . . . . . . . . . . . . . . . . . . . . . . . . . . . . . . 51
5.6 LCOE, capacity factor, AEP wake losses and energy yield density results for different wind turbine spacings in relation to the base case 4.3D. . . . . . . . . . . . . . . . . . . . . . 53
5.7 Simulated maximum and minimum platform movements for turbines with the 90 m, 102 m, and 109 m hub heights. . . . . . . . . . . . . . . . . . . . . . . . . . . . . . . . . . . . 56
5.8 Platform motions dependent mooring loads analysis for the OC4 semi-submersible platform performed by NREL [88]. . . . . . . . . . . . . . . . . . . . . . . . . . . . . . . . . . . . 56
5.9 Maximum moments on the base of the turbine tower in the $x$-direction for turbines with 90 m, 102 m, and 109 m hub heights. . . . . . . . . . . . . . . . . . . . . . . . . . . . . . 57
5.10 Maximum moments on the base of the turbine tower in the $y$-direction for turbines with 90 m, 102 m, and 109 m hub heights. . . . . . . . . . . . . . . . . . . . . . . . . . . . . . 57
5.11 Maximum moments on the base of the turbine tower in the $z$-direction for turbines with 90m, 102m, and 109m hub heights. . . . . . . . . . . . . . . . . . . . . . . . . . . . . . . . 58
5.12 LCOE, capacity factor, AEP wake losses and energy yield density results for different wind turbine hub height variations in relation to the base case 4.3D (ALLTRB_90m). . . . . . . 58
5.13 LCOE, capacity factor, AEP wake losses and energy yield density results for the 2R Dephased and Diamond wind farm layouts in relation to the base case 4.3D. . . . . . . . 61
5.14 LCOE, capacity factor, AEP wake losses and energy yield density results for different R-dephasing values of the 4.3D Dephased farm layout in relation to the base case 4.3D. . 62
5.15 LCOE, capacity factor, AEP wake losses and energy yield density results for different turbine spacings in the 2R-Dephased farm layout in relation to the base case 4.3D. . . . . 63

# List of Tables

3.1 NREL OC4 semi-submersible platform structural and hydrodynamic properties [88]. . . . 27
3.2 NREL OC4 semi-submersible platform mooring lines properties [88]. . . . . . . . . . . . 28
3.3 NREL 5 MW wind turbine specifications [89]. . . . . . . . . . . . . . . . . . . . . . . . . . 29
3.4 NREL 5 MW turbine rotor speed and pitch angle values for different wind speed classes that are used as the simulations' initial conditions [89]. . . . . . . . . . . . . . . . . . . . . 29
3.5 Semi-submersible platform-adjusted NREL 5 MW wind turbine structural specifications [88]. 30
3.6 Characteristic wave-wind climate in the northwest coast of Portugal. For each wind speed class, $u$, is presented the associated sea state conditions in terms of significant wave height, $H_\mathrm{s}$, and peak period, $T_\mathrm{p}$. The probability of occurrence of each wind class, $\xi_u$, is also presented. Data for $H_\mathrm{s}$ and $T_\mathrm{p}$ represent 5% trimmed mean values. . . . . . . . . . . . . . 31
3.7 Reference case wind farm specifications. . . . . . . . . . . . . . . . . . . . . . . . . . . 33

4.1 Specification of the low-resolution and high-resolution domains in the simulated cases. LR stands for low-resolution, and HR stands for high-resolution. . . . . . . . . . . . . . . . . 38
4.2 Input variables values considered in the wind farm cost model with their corresponding references. . . . . . . . . . . . . . . . . . . . . . . . . . . . . . . . . . . . . . . . . . 41
4.3 Repair time, failure rate, technicians and vessels needed in case of specific wind farm maintenance works. CTV stands for crew transfer vessel; and CLV represents the cable laying vessel [107]. . . . . . . . . . . . . . . . . . . . . . . . . . . . . . . . . . . . . 44
4.4 Material and repair costs of different maintenance works [107]. . . . . . . . . . . . . . . 44

5.1 Study cases summary. . . . . . . . . . . . . . . . . . . . . . . . . . . . . . . . . . . . . 47
5.2 Electricity generation, wake losses, capacity factor and the energy yield density values for the base case simulation. . . . . . . . . . . . . . . . . . . . . . . . . . . . . . . . . . . 49
5.3 CAPEX: material and installation costs calculated for the base case. . . . . . . . . . . . 50
5.4 OPEX and DECEX calculated for the base case. . . . . . . . . . . . . . . . . . . . . . . 51
5.5 Comparison of selected costs components' shares between this thesis and NREL Report [47] for the cost model validation. . . . . . . . . . . . . . . . . . . . . . . . . . . . . . . 52
5.6 Net annual electricity farm production for different turbine spacing variations. . . . . . . 53
5.7 Tower height, approximate tower mass and semi-submersible platform center of mass relative to the sea water level (SWL) for turbines with different hub heights used in the thesis. 55

5.8 Net annual electricity farm production for different turbine hub height variations. . . . . . . 59
5.9 Net annual electricity farm production for different wind farm layout variations. . . . . . . . 60
5.10 Net annual electricity farm production for different turbine spacing in the 2R-Dephased wind farm layout. . . . . . . . . . . . . . . . . . . . . . . . . . . . . . . . . . . . . . . . . 62
5.11 Platform size reduction impact on LCOE based on the ALLTRB_78m case. . . . . . . . . . 64
5.12 Selection of the best simulation cases in each of the conducted simulation sets. The AEP increase and LCOE reduction rows represent the relative differences in the mentioned values in comparison to the base case. . . . . . . . . . . . . . . . . . . . . . . . . . . . . 64

# Nomenclature

## Latin symbols

| | |
|---|---|
| $a_{\mathrm{BEM}}$ | BEM theory axial induction factor (-) |
| $a'_{\mathrm{BEM}}$ | BEM theory tangential induction factor (-) |
| $A_{\mathrm{OWF}}$ | Total wind farm area ($\mathrm{km}^2$) |
| $A_{\mathrm{R}}$ | Rotor area ($\mathrm{m}^2$) |
| $AEP_{\mathrm{farm,net}}$ | Net annual electricity farm production (GWh/year) |
| $AEP_{\mathrm{farm.gross}}$ | Gross annual electricity production of the simulated wind farm (GWh/year) |
| $AEP_i$ | Annual electricity production in year i (GWh) |
| $AEP_{\mathrm{ideal}}$ | Annual electricity production for a wind farm operating without wake losses (GWh/year) |
| $AEP_{\mathrm{Uw}}$ | Annual electricity production for a specific wind speed (GWh/year) |
| $AEP_{\mathrm{WT}}$ | Total annual electricity generated for each turbine (GWh/year) |
| $b_{\mathrm{DWM}}$ | Instantaneous wake half width in the DWM model (m) |
| $c$ | Airfoil chord line (m) |
| $c_d$ | Drag coefficient (-) |
| $c_l$ | Lift coefficient (-) |
| $c_{\mathrm{Weibull}}$ | Weibull function scale parameter (-) |
| $C_{\mathrm{Condition}}$ | Condition monitoring cost (M€/year) |
| $C_{\mathrm{Facilities}}$ | Operating facilities yearly cost (M€/year) |
| $C_{\mathrm{HSE}}$ | Health, safety and environment (HSE) monitoring cost (M€/year) |
| $C_{\mathrm{Insurance}}$ | Farm insurance yearly cost (M€/year) |
| $C_{\mathrm{Landlease}}$ | Landlease cost (M€/year) |
| $C_{\mathrm{Mgmt,marine}}$ | Marine operations management cost (M€/year) |
| $C_{\mathrm{Mgmt}}$ | Onshore wind farm management cost (M€/year) |
| $C_t$ | Thrust coefficient (-) |
| $C_{\mathrm{T}}$ | Total cost of the turbines (M€) |
| $C_{\mathrm{Weather}}$ | Weather monitoring cost (M€/year) |
| $D$ | Turbine rotor diameter (m) |

| | |
|---|---|
| $f_{\text{Weibull}}$ | Weibull probability for specific wind class (%) |
| $F_1, F_2$ | Downstream distance-dependent filter functions ($\frac{\text{m}^2}{\text{s}}$) |
| $F_{\text{ax}}$ | Axial force exerted on an actuator disc (N) |
| $F_{\text{L}}$ | Drag force (N) |
| $F_{\text{L}}$ | Lift force (N) |
| $H_{\text{s}}$ | Significant wave height (m) |
| $I_{\text{Amb}}$ | Hub height ambient intensity of the turbulence (%) |
| $k_{\text{Amb}}$ | Constant for calibration in the DWM model (-) |
| $k_{\text{DWM}}$ | Flow field constant in the DWM model (-) |
| $k_{\text{Frandsen}}$ | Shape parameter in the Frandsen model (-) |
| $k_{\text{Jensen}}$ | Semi-empirical wake decay constant (-) |
| $k_{\text{Weibull}}$ | Weibull function shape parameter (-) |
| $\dot{m}$ | Fluid mass flux ($\frac{\text{kg}}{\text{m}^2 \cdot \text{s}}$) |
| $n_{\text{rows}}$ | Number of the turbine rows in the wind farm (-) |
| $n_{\text{T}}$ | Total number of turbines in the wind farm (-) |
| $p$ | Pressure (Pa) |
| $P_{\text{disc}}$ | Energy absorbed by an actuator disc (J) |
| $P_{\text{t,nom}}$ | Nominal turbine power (MW) |
| $P_{\text{Uw}}$ | Power generated on the wind turbine for a specific wind speed (MW) |
| $P_{\text{WF}}$ | Total nominal power of the wind farm (MW) |
| $r$ | Discount rate (%) |
| $r_1$ | Expanded wake radius immediately after the turbine rotor (m) |
| $r_d$ | Turbine rotor radius (m) |
| $r_{\text{Jensen}}$ | Radial distance from the wake center in the Jensen model (m) |
| $r_x$ | Wake radius at the x distance from the turbine (m) |
| $R$ | Rotor radius (m) |
| $T$ | Lifetime of the project (years) |
| $T_{\text{p}}$ | Peak wave period (s) |
| $u$ | New model wake velocity ($\frac{\text{m}}{\text{s}}$) |
| $u^*$ | Wake velocity at a distance $x$ from the turbine ($\frac{\text{m}}{\text{s}}$) |
| $u_0$ | Undisturbed inflow wind velocity ($\frac{\text{m}}{\text{s}}$) |
| $U_{\text{d}}$ | Fluid velocity at an actuator disc ($\frac{\text{m}}{\text{s}}$) |
| $U_{\text{def,min}}$ | Minimal wake velocity ($\frac{\text{m}}{\text{s}}$) |
| $U_{\text{H}}$ | Hub height wind speed ($\frac{\text{m}}{\text{s}}$) |
| $U_i$ | Velocity components in direction i ($\frac{\text{m}}{\text{s}}$) |

| | |
|---|---|
| $V_{\text{avg}}$ | Mean wind speed ($\frac{\text{m}}{\text{s}}$) |
| $V_{\text{eff}}$ | Effective wind velocity ($\frac{\text{m}}{\text{s}}$) |
| $V_r$ | Mean velocity in the radial direction r ($\frac{\text{m}}{\text{s}}$) |
| $V_{\text{ref}}$ | Reference wind velocity ($\frac{\text{m}}{\text{s}}$) |
| $V_{\text{w}}$ | Streamtube inflow wind velocity ($\frac{\text{m}}{\text{s}}$) |
| $V_z$ | Wind speed at the elevation above the sea level ($\frac{\text{m}}{\text{s}}$) |
| $z$ | Height of the wind turbine hub (m) |
| $z_0$ | Surface roughness of the terrain (m) |

## Greek symbols

| | |
|---|---|
| $\alpha$ | Blade angle of attack (°) |
| $\alpha_{\text{Frandsen}}$ | Expansion constant (-) |
| $\alpha_{\text{roughness}}$ | Roughness coefficient (-) |
| $\beta_{\text{Frandsen}}$ | Initial expansion rate coefficient (-) |
| $\Delta AEP_{\text{airfoil}}$ | Airfoil damage lossess (%) |
| $\Delta AEP_{\text{availability}}$ | Availability of the wind farm due to maintenance (%) |
| $\Delta AEP_{\text{transmission}}$ | Transmission system losses (%) |
| $\Delta AEP_{\text{wake}}$ | Wake losses on the annual electricity production of the wind farm (%) |
| $\mu$ | Viscosity of the molecules (Pa ·s) |
| $\nu_t$ | Eddy viscosity ($\frac{\text{m}^2}{\text{s}}$) |
| $\Omega$ | Rotational speed of the turbine (rad/s) |
| $\phi$ | Wind inflow angle (°) |
| $\rho$ | Density of air ($\frac{\text{kg}}{\text{m}^3}$) |
| $\sigma$ | Local solidity of the blade element (-) |
| $\sigma_v$ | Standard deviation of wind data ($\frac{\text{m}}{\text{s}}$) |
| $\tau_{ij}$ | Stress tensor ($\frac{\text{N}}{\text{m}^2}$) |
| $\xi_w$ | Wind speed occurrence probability (%) |

## Acronyms & Abbreviations

| | |
|---|---|
| AEP | Annual electricity production |
| AHV | Anchor handling vehicle |
| ALLTRB | Wind farm heaving all of the turbines |
| AWAE | Ambient wind and array effects |
| BEMT | Blade element momentum theory |

| | |
|---|---|
| BET | Blade element theory |
| CAPEX | Capital expenditures |
| CF | Capacity factor |
| CFD | Computational fluid dynamics |
| CLV | Cable laying vessels |
| CM | Center of mass |
| CTV | Crew transfer vessel |
| DECEX | Decommissioning expenditures |
| DWM | Dynamic wake meandering |
| EYD | Energy yield density |
| FOW | Floating offshore wind |
| GHG | Greenhouse gases |
| HR | High-resolution domain |
| IEA | International Energy Agency |
| Inc. | Incorporated |
| IRENA | International Renewable Energy Agency |
| JUV | Jack-up vessel |
| KFWind | The Korea floating wind |
| LCOE | Levelized cost of energy |
| LES | Large eddy simulation |
| LR | Low-resolution domain |
| MSL | Mean sea level |
| MT | Momentum theory |
| NOAA | National Oceanic and Atmospheric Administration |
| NREL | National Renewable Energy Agency |
| NVP | Net presents value |
| O&M | Operations and maintenance |
| OPEX | Operational expenditures |
| RANS | Reynolds-averaged Navier-Stokes |
| RES | Renewable energy sources |
| SB | Offshore substation |
| SC | Super-controller |
| SCADA | Supervisory control and data acquisition |
| SDG | Sustainable Development Goals |
| SGS | Sub-grid scaling |

| | |
|---|---|
| SS | Semi-submersible platform |
| UN | United Nations |
| WACC | Weighted average cost of capital |
| WT | Wind turbine |

# Chapter 1

# Introduction

## 1.1 Motivation

Human-induced climate change is being recognized as one of the biggest problems humanity may face in the upcoming years or even decades. It has been observed that it had led to extreme weather conditions, damages to different ecosystems, higher disease risks, degradation of forests, sea level rising or biodiversity losses [1]. Although most of the climate changes in the history of the Earth were induced by natural factors, they were not as rapid as they are now. For the last few centuries, humanity has impacted the environment through greenhouse gases (GHG) production by power generation, agriculture, or transportation, deforestation by land development, and raw material usage in such a way that these changes are too fast for different biomes to adapt to [2].

Since the 19th century, global greenhouse gas emissions have been rising, reaching the highest peak in 2019. Fossil fuels had the highest contribution to the GHG emission levels, reaching 36.71 billion tons in 2019. The largest share of these emissions (34%) was produced by the energy sector for energy generation purposes. In years 2020 and 2021, COVID-19 pandemic resulted in a decrease in GHG emissions [3, 4].

Increasing concerns about rising GHG emissions and climate change consequences led to establishment of the international Paris Agreement in 2015. In the agreement, the acceding countries agreed to introduce long-term measures to reduce GHG emissions and increase the resilience to climate change while maintaining sustainable development and economic growth. The Agreement included a goal of limiting the global temperature increase to 2°C, preferably 1.5°C in comparison to the pre-industrial stage [4, 5, 6].

In addition, the United Nations (UN) organization introduced 17 Sustainable Development Goals (SDGs) along with The 2030 Agenda for Sustainable Development, which present guidelines for every country in the world to protect the planet and to reach peaceful and prosperous lives for every person on the Earth. SDG 7 “Ensure access to affordable, reliable, sustainable and modern energy for all” and SDG 13 “Take urgent action to combat climate change and its impacts” are important considering the topic of this thesis. In SDG 7 it is stated that modern renewable energy action acceleration is required and it is important to increase its share in the final energy consumption. Complementary SDG 13 declares the need to shift economies towards carbon neutrality to reduce the average global temperature rise, which already is at 1.2°C level [7].

Considering the above-presented concerns, it is important to continue the development and technological sophistication of renewable energy solutions. They can help in decarbonization of the energy sector and in supplying people's electricity needs. In the renewable energy sector, the two most common renewable energy sources (RES) are solar and wind systems [8], which have a high variability in electricity production. According to 2021 UN report, it is estimated that new solar and wind projects had already achieved lower electricity production costs than new coal technologies [8].

Out of the available renewable energy sources, wind energy is estimated to have the highest $CO_2$ reduction capability by the year 2050 [9]. Due to increasing onshore wind limitations [10], offshore wind energy is getting more recognition, providing better exploitation of wind resources, the possibility of larger turbine utilization and lower environmental impacts [11, 10, 12]. It is estimated, that the worldwide technical offshore wind energy potential is equal to 120 000 GW of power, being able to generate over 420 000 TWh of electricity per year, which is enough to meet 11 times the expected global electricity demand in 2040 [13]. Among the offshore wind energy solutions, floating offshore wind farms are showing promising outcomes, thanks to, for example, the ease of installation, onshore manufacturing and assembly, or the ability to be installed in deep water conditions [14, 15]. However, the investment costs, as well as levelized cost of energy (LCOE) values of floating offshore wind projects are still high, compared to the other wind energy solutions and remaining renewable energy sources [16, 17]. Therefore, there is still more research and development to be done to reduce the costs of floating offshore wind projects. Leading global offshore wind-related companies, such as Shell and RWE [18], General Electric [19], or Siemens Gamesa [20] have started new research projects to reduce the offshore wind projects costs. In this sense, this thesis is aiming to research different ways of potential floating offshore wind energy cost reductions.

## 1.2 Objective

The main objective of this thesis is to investigate the potential levelized cost of energy reduction factors in floating offshore wind farms. It aims to identify and evaluate techno-economically different strategies that can contribute to the overall performance and profitability improvements of floating offshore wind farms. These goals are achieved by aero-hydro-servo-elastic numerical simulations and cost-modeling of different wind farm configurations, varying in turbine spacing distances, turbine hub heights, farm layouts, and the floating platform size. The main farm evaluation factors addressed in this thesis are the annual electricity production, farm energy losses due to the wake effects, farm capacity factor, the levelized cost of energy, and an energy yield density factor, introduced in this thesis. Another important objective of this thesis is to provide recommendations for future research on potential LCOE reduction strategies, and techno-economical floating offshore wind farm assessment methodologies.

## 1.3 Methodologies and limitations

In this thesis, a reference wind farm (base case) is defined. The definition of the case includes the selection of the turbine, floating platform, transmission system, and other main components. A specific farm location, off the port of Leixões, is selected and its wave and wind resource characterization are determined. The reference farm layout is based on an existing wind farm. The base case is then used to define twenty-five case studies, that are divided into four sets, in which different variables are analyzed. The first set of case studies considers the variations in the turbine spacing within the wind farm row. The second one addresses different configurations of turbine hub heights in a wind farm row. The third set considers different wind farm layout variations and the fourth set studies the impact of turbine spacing in one of the wind farm layouts. Finally, the platform size reduction impact on the LCOE is estimated by a cost-modeling approach, based on an already simulated case with low turbine hub heights.

For each of the defined cases, power generation simulations are done using FAST.Farm software [21] for different wind speeds ranging from 3 m/s to 25 m/s. The generated power results are then used to calculate the annual electricity production, the wind farm's annual energy wake losses, the farm capacity factor, and the energy yield density. In addition, a literature-based wind farms' cost model including the CAPEX, OPEX, and DECEX was prepared and used to estimate the LCOE values for every studied case.

The simulation results are verified by comparing the farm capacity factor and energy losses due to the wake effects results with information available in the literature. The model is also verified by comparing the power, blade pitch angle, and rotational speed curves obtained from the simulations with the values presented in the reference turbine definition document. The cost-modeling approach is verified based on the obtained cost components shares and the levelized cost of energy values with different literature sources.

The limitations of this study are listed below.

- Due to computational power and time limitations, the simulations were done for only one row of a wind farm. Therefore, the exact impact of the turbines in the other rows could not be determined.

- As the manufacturers of wind farm components and firms specializing in offshore wind installation do not publicly provide the prices of their products and services, the values used in the cost model in this thesis are based on estimates from different literature sources. Therefore, the costs calculations represent only an approximation of the real wind farm costs.

- The wind farm cost model presented in this thesis includes material cost reductions for the turbines and the floating platforms but does not consider additional potential costs reductions associated with the manufacturing and labor, which may impact the levelized cost of energy values. Therefore, a more detailed, commercially-based cost model for different turbine hub heights and floating platform sizes would need to be further researched.

## 1.4 Structure of the thesis

The thesis consists of 6 chapters, which are organized as follows:

- Chapter 1 describes the motivation, main objectives, methodologies, and limitations of this study.
- Chapter 2 presents the theoretical background and state-of-the-art for floating offshore wind farms, which include the wind turbines and foundation descriptions, farm development process, offshore wind market outlook, and cost reduction methods outline. It also describes the different wake models available in the literature for farm assessment, including the model used in this thesis and the tools used.
- Chapter 3 contains a description of a reference wind farm case with its layout and location, chosen site with its wind and wave resources characterization, and the farm's main components.
- Chapter 4 outlines the simulations approach description, along with the wind farm's costs model and energy calculation methodology used in the study. It also contains information on evaluation factors used for the cost of energy and performance assessment.
- Chapter 5 presents the results for all simulated cases, comparing their annual electricity production, LCOE, capacity factor, wake losses, and energy density.
- Chapter 6 summarizes the findings, concludes, and provides recommendations for wake losses reductions in wind farms.

# Chapter 2

# Theoretical Background and state-of-the-art

In this Chapter a theoretical background and state-of-the-art of floating offshore wind farms is presented. It includes the wind turbines and foundations descriptions, farm development process, offshore wind market outlook, cost reduction methods, wake models and tools used in this thesis.

## 2.1 Offshore wind energy

According to the International Renewable Energy Agency's (IRENA) "Future of Wind – A Global Energy Transformation" report, onshore and offshore wind energy systems could become the most notable RES by 2050, generating around 35% of the total electricity demand. Figure 2.1 presents the energy-related $CO_2$ emissions reduction forecast by RES for 2050 compared to 2018. It showcases a possible emissions reduction of 27% by reaching 6044 GW of wind power by the year 2050, which represents the highest share out of all renewable energy sources. This makes wind energy one of the most prominent contributors in climate change impacts reduction out of the available renewable energy technologies [9].

Onshore wind energy sources may reach a development limit due to increasing difficulties in finding appropriate sites for future wind farms, as they produce visual and noise impacts. Offshore technologies allow higher exploitation of natural wind resources, delivering capacity factors ranging from 40% up to 60%. They allow installations of larger turbines, generating more power and a higher electricity production compared to onshore sites. In addition to that, offshore wind sites have lower wind shear due to the ground roughness and higher mean wind speeds than the onshore sites [11, 10, 12].

Taking into consideration possible onshore wind farms development limits and higher capacity factors and lower environmental impacts of offshore wind farms, it is important to focus on further development of offshore technologies.

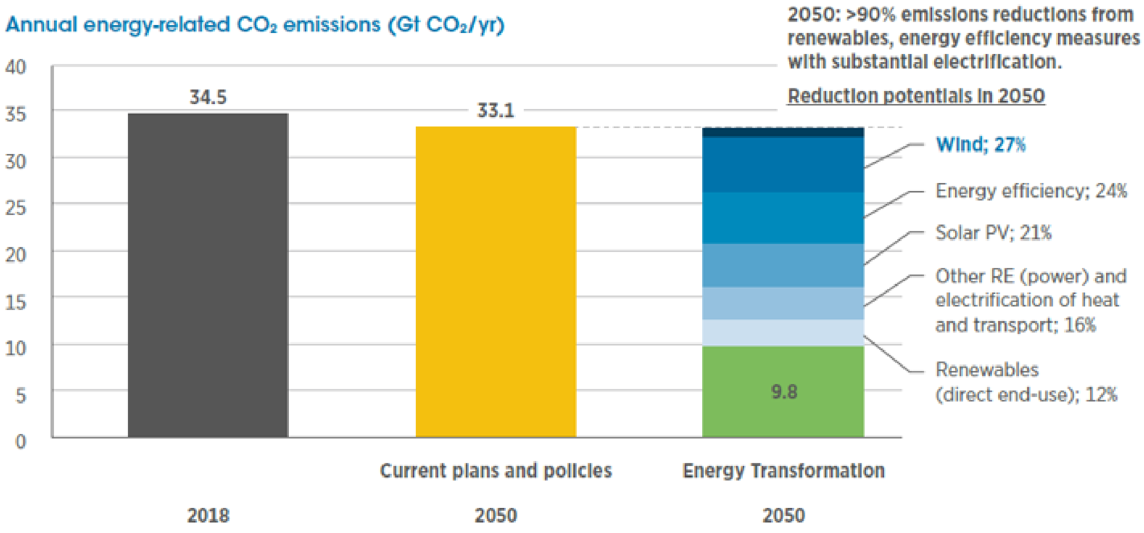

**Figure 2.1:** Energy-related $CO_2$ emissions' (Gt $CO_2$/year) reduction forecast [9].

## 2.2 Offshore wind turbines

The history of the offshore wind industry dates back to 1991 when Vindeby [11, 22] developed the first offshore wind turbine with a power capacity equal to 0.45 MW, with the diameter and tower height equal to 35 m. Since then, the technological advancements and industry expansion lead to a gradual increase in the turbine sizes and their power capacities. Figure 2.2 showcases this trend in the previous years and presents how the increase in size enabled to achieve higher power capabilities of offshore wind turbines [22]. In 2022, the biggest commercially available turbines on the market reached 12-15 MW of power with 220 m in the turbine diameter. It is expected, that the upcoming turbine models will achieve even 15-20 MW with over 230 m of turbine diameters in the years 2025-2030 [9].

## 2.3 Offshore structures for wind turbines

Nowadays, offshore wind energy turbines may be either mounted by a bottom-fixed structure or floating. Floating wind platforms are a relatively new technology, as the first deployed commercial project using floating platforms was commissioned in 2017 in Scotland with 30 MW of rated power. Therefore, the current offshore market is mostly comprised of bottom-fixed systems. However, recent developments and cost reductions of floating offshore wind (FOW) systems paved the way to their further deployments [23, 24]. According to different sources, about 58% in the US [25] or even up to 80% in Europe [11] of wind resources potential is based in water depths exceeding 60 m. Under these conditions, bottom-fixed turbines become too challenging to deploy and floating wind platforms may become more cost-effective and generate more power in the regions far from shore [24]. Figure 2.3 presents different bottom-fixed and floating wind turbine foundations [26].

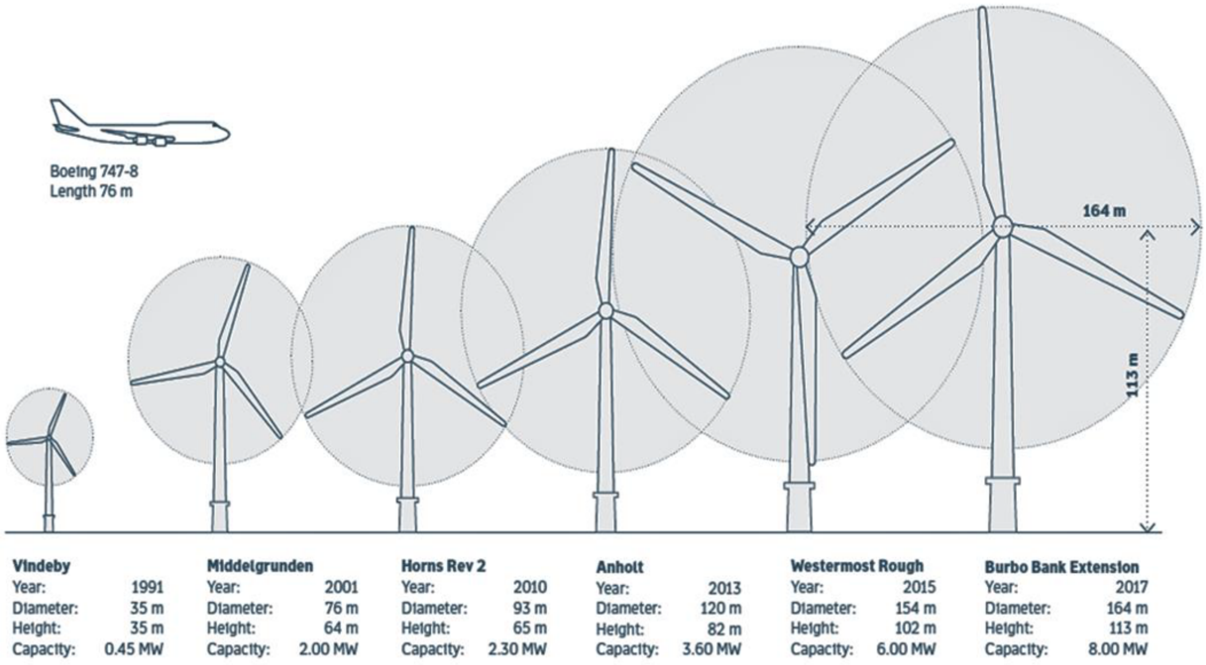

**Figure 2.2:** Offshore wind turbines size and capacity development over the years [22].

### 2.3.1 Bottom-fixed wind turbines

Bottom-fixed wind turbines require mounting to the bottom of the water reservoir, that is why they become more costly with the increasing water depth. Also, they heavily depend on the soil quality and conditions. On the other hand, their construction is simpler and less challenging than floating structures [24].

The monopile type is the simplest foundation, consisting of one steel pile installed in the seabed. It is applicable for water depths ranging from 20 m to 40 m [24]. Tripod systems are more stable and stiff compared to monopiles and can be mounted in deeper waters. Jacket foundations are steel-framed structures, which are very robust and are viable for depths of 50-70 m [24]. Jacket structures also have lower soil dependency and are not impacted by external loads that much, compared to the other types [27]. Suction-based anchors can support all of the three aforementioned types of foundations by using suction cups that stick to the seabed due to pumping out water from the suction caisson. Gravity-based foundations use gravity forces to lay on the bottom of the sea, are applicable in clay, sandy, or rock seabed conditions and are not viable for depths higher than 10 m [28, 29].

### 2.3.2 Floating wind turbines

Floating wind turbines enable the utilization of wind resources in deep waters, as they do not require being directly mounted to the seabed. They use buoyancy, ballasting, or mooring stabilization [14, 15]. The turbines with the platforms are mainly constructed onshore and then assembled offshore after towing the platform and mounting the turbine on them on the site [14]. However, new platform designs are being conceived to be fully assembled at ports, like the WindFloat platform concept [30]. The platforms require mooring and anchoring to the seabed so as not to drift away. The mooring systems, however, are not that

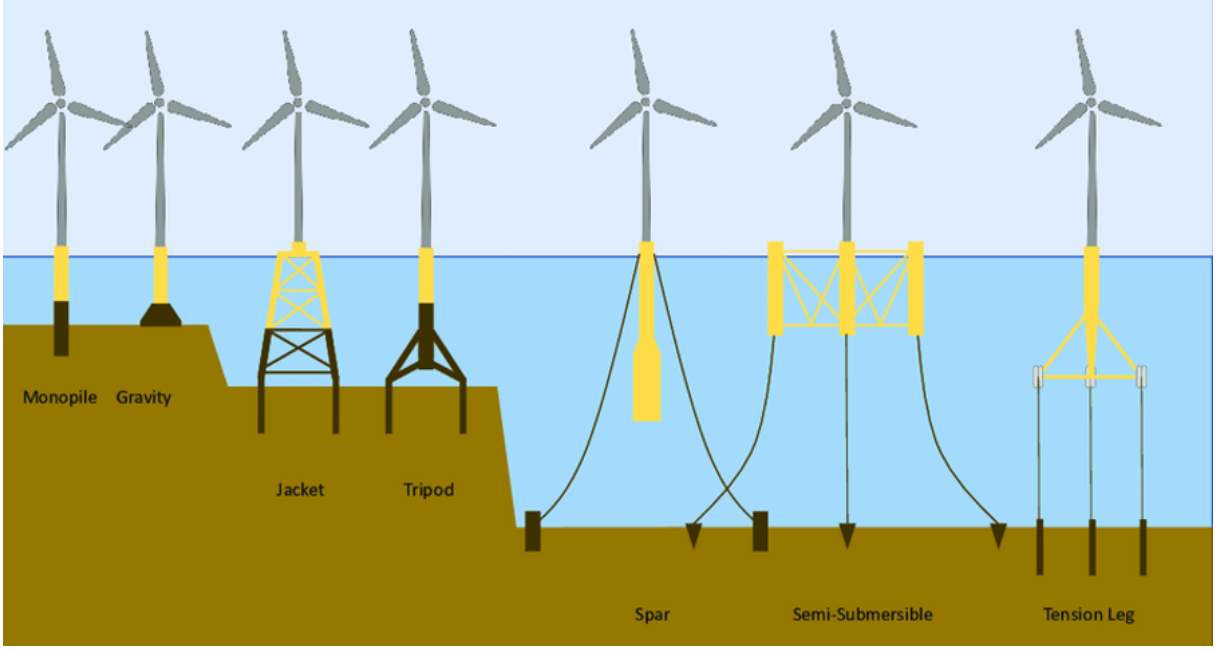

**Figure 2.3:** Types of bottom-fixed and floating mounting systems used in offshore wind energy wind turbines. From the left: monopole, gravity-based, jacket, tripod, spar-buoy, semi-submersible, tension-leg [26].

challenging to install in comparison to the bottom-fixed turbines [24, 31].

Spar-buoy type platforms are ballast-stabilized, cylindrical-shaped structures that float on water. Their center of gravity is usually lower than their center of buoyancy. Their design is relatively simple and they are relatively stable, compared to the other floating foundations [11]. On the other hand, the assembly of the turbine needs to be on the site and may be challenging and time-consuming [14]. They also have high costs and high loads on the tower base and they require specialized installation vessels [14].

Semi-submersible (SS) platforms are buoyancy-stabilized and their stabilizing righting moment is obtained by having a large second moment of area respective to its rotational axis, acquired by a large waterplane area or smaller cross-sectional areas distanced from the platform central axis [14, 15]. These systems can be used in shallow and deep water conditions and they can be assembled onshore without any special vessels requirements and towed to the wind farm site with tugboats [11, 14, 31]. The mooring and anchoring system is simpler compared to the other floating types. On the other hand, they have high structural mass and a complicated design and manufacturing [24, 31, 15].

The tension leg platform is a mooring-stabilized structure that uses highly tensioned mooring lines to generate a restoring moment when the platform is inclined [15]. They have low mass, high stability, and the structure is simple [24, 14, 15]. They can be assembled onshore and the material usage is reduced in comparison with semi-submersible solutions. However, they experience high loads on the mooring and anchoring systems, which translates to higher operational risks during their malfunctions [9, 11].

## 2.4 Offshore wind farms: Lifecycle and development process

The lifecycle and development process of a wind farm can be divided into different stages presented in Figure 2.4 [14].

**Figure 2.4:** Lifecycle and development process of a wind farm [14].

The planning and production stage's purpose is to conduct the financial and economic feasibility analysis, select the site and the contractors, gather data on possible impacts of the wind farm, and secure consents for farm deployment. One of the most important parts in this stage is selecting the proper site, which is supported by resource assessment, geological, hydrographical and meteorological surveys [14, 32]. Their purpose is to analyze the seabed, water depth, and meteorological resources to establish potential electricity production and describe the construction process and operating conditions of the farm. Additionally, different environmental assessments are done to define the potential impact of the construction on the marine and air animals as well as communities living near the coastal areas [32, 33].

In the production and acquisition stage, the wind turbines design, foundation types, gearbox and generator assessment, mooring systems, and others take place. Analyses are done to determine the potential electricity production of different turbine and farm designs, the balance of the plant, mooring systems spatial arrangement of the turbines, the wake effect impacts, and others [32]. The materials used for the construction are selected and cable paths determined. After the design stage, the components of the wind farm are manufactured.

Installation and commissioning stage consists of the foundation installation or the floating platforms towing to the location, turbine and platform assembly, cabling running and installation, and mooring systems connection [14, 32]. In the case of semi-submersible platforms, they can be constructed and assembled onshore and then towed to the designated location using tugboats and connected to pre-installed mooring systems [14]. After installation and conducting electrical and mechanical tests, the wind farm is ready to be connected to the onshore supporting facility and commissioned [32].

The purpose of the operation and maintenance stage activities is to ensure that the wind farm is operating in safe conditions and the electricity production is optimized according to the resources and conditions on the site [34]. During the operation stage of the wind farm, the site is remotely monitored and controlled, and repaired in case of failures. Health and safety inspections as well as main components inspections are done. In this stage of the wind farm lifecycle, the farm is in its operational stage and generates electricity [32, 33].

The lifespan of offshore wind farms is around 20-25 years [35, 36]. After this time, the installation must be decommissioned by the contractors. In this stage, the turbines, foundations and platforms, cables and mooring systems need to be removed and shipped onshore. After removal and shipping, following assets' lifecycle, the components must be recycled, reused or disposed, so the maximum possible value can be extracted sustainably [34, 32]. The circular economy requirements for the sector have been reinforced by the European Commission through the Circular Economy action plan that now involves the European Green Deal [37].

## 2.5 Offshore market outlook

According to IRENA's Renewable Energy Capacity Statistics 2021, the cumulative offshore wind power capacity installed worldwide by the end of 2020 was equal to 34 367 MW with Europe leading the market with 24 920 MW installed, followed by Asia with 9 418 MW (with China having installed the majority, about 8 990 MW) and the US with 29 MW of installed capacity [38]. The global growth of the total installed capacity in 2020 was equal to 5 519 MW owing to new deployments by China, the Netherlands, the UK, Belgium and Germany as the biggest contributors [16].

The manufacturers of wind turbines: Siemens Gamesa, GE and Vestas have announced they started working on the design of new offshore wind turbines of capacities ranging from 12-15 MW. According to them, the turbines will be available for commercial usage in 2024 or sooner [16].

### 2.5.1 Floating offshore wind markets

In 2020, the future potential for FOW tripled compared to the previous year, growing from 7 663 MW to 26 529 MW, as many new projects started their planning stage then [16]. This shows that the floating offshore market is going to develop in the coming years with more and more projects being commissioned and planned. In 2022, there are 12 operating FOW projects, having a total of 129 MW of capacity installed [16]. Additionally, there are 14 projects of 243 MW capacity in total, which are under construction or received approval for development and 87 projects in the planning stages which will have a total of 26 078 MW capacity [16, 39]. The majority of the offshore structures used in the planned projects are semi-submersible platforms representing a share of 64% of all of the planned installations. Less commonly used types are spar-buoy (13%), barge (10%), tension-leg (7%) and semi-spar (4%) platforms [11]. Figure 2.5 presents a forecast of the cumulative installed capacity of floating offshore wind (FOW) farms by country based on the already announced projects with the year of completion by 2026 [16].

Looking at Figure 2.5, it can be noticed that the highest share of floating wind capacity in 2026 will be held by South Korea, Saudi Arabia, Spain, and France. However, these projects are still in the planning stage, so not all of them might be commissioned due to economic feasibility [16].

According to the Offshore Wind Outlook 2019 [13], the offshore wind market is going to become a $1 trillion business with at least a 15-fold increase by 2040, compared to 2019. According to IRENA Future of Wind report [9], it is estimated that around 5 GW up to 30 GW of floating offshore wind capacity may be installed by 2030. Based on various regions development pace, FOW could reach 5% to 15% share in the installed global offshore wind capacity, totalling to 1000 GW, by 2050 [9]. According to different countries strategies, the Chinese government aims to reach a 1 GW of floating offshore wind installed capacity by 2030 and Japan expects to install 18 GW of FOW power by 2050 [9]. In the US, around $1

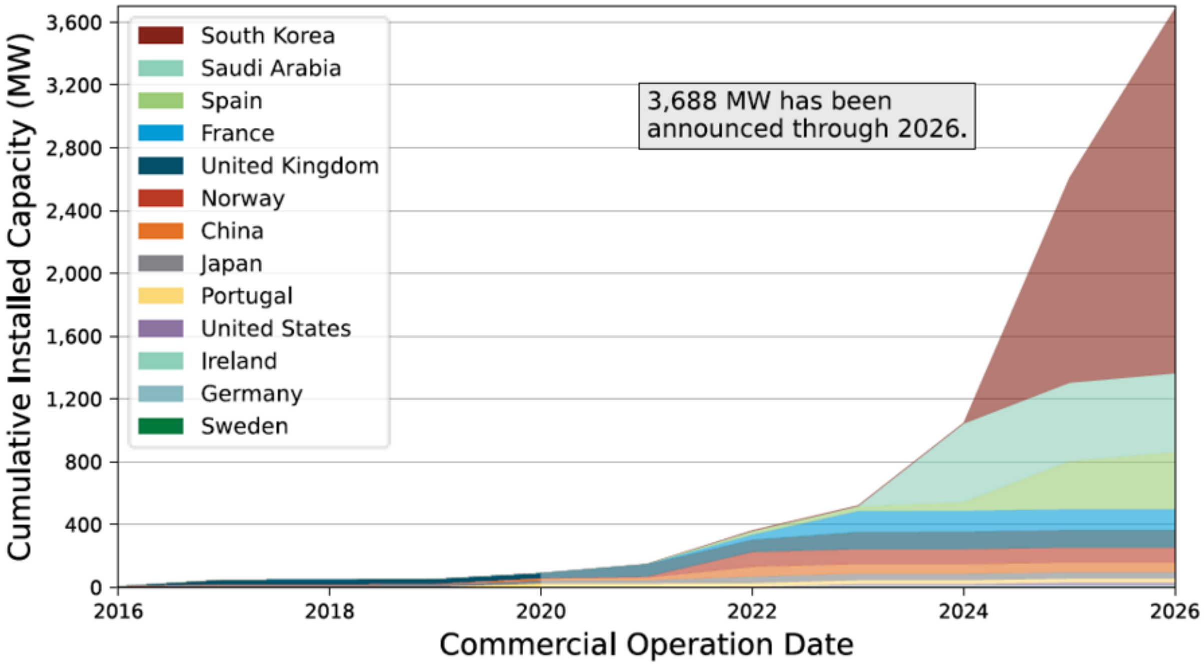

**Figure 2.5:** Cumulative installed capacity of floating offshore wind farms forecast based on already announced projects by 2026 [16].

billion of investments have been done in order to launch new FOW demonstration plants [9] and reach 30 GW by 2030 and 110 GW by 2050 offshore wind capacity goals [16]. In Europe, it is expected to continuously deploy floating offshore wind projects, in order to reach its 450 GW by 2030 offshore wind target [9]. Among European countries that have declared their offshore wind energy capacity goals are Germany with its 15 GW - 20 GW by 2030 and 40 GW by 2040 goal; Poland having declared 28 GW of offshore wind power installed by 2050; or the UK setting a 40 GW of offshore wind and 1 GW of FOW capacity by 2030 goal [11].According to the Global Wind Energy Council report [11], the FOW levelized cost of energy values will decline by 17-40% from 2035 to 2050.

### 2.5.2 Floating offshore wind projects

The largest currently operating FOW farm is the Kincardine project Scotland deployed by Bourbon Subsea & Vryhof and other partners, installed along the east coast of Scotland [39]. It hosts five 9.5 MW Vestas V164 turbines and is installed 15 km from the shore at a water depth of 60-80 m. The type of foundation used is a semi-submersible platform. The farm was commissioned in October 2021 [39]. Other bigger floating offshore wind projects currently operating are Hywind Scotland (30 MW) in the UK operating since 2017, Windfloat Atlantic (25 MW) in Portugal operating since July 2020, and SEM-REV test site at Le Croisic (2 MW) in France operating since 2018 [16, 40].

The largest commercial project to be commissioned in the future is the Korea Floating Wind (KFWind) farm which is to be deployed near the coast of Ulsan City, 65 km from the shore at a water depth equal to 250 m [41]. The farm is estimated to be completed in 2026 and provide 1 000 MW of capacity. The companies working on the farm are Principle Power Inc. and Wind Power Korea.

Another interesting project is the Redwood Coast Offshore Wind Project, which is expected to be finished in 2026 by a consortium including Principle Power, Ocean Winds, Aker Offshore Wind, H. T. Harvey & Associates and Herrera Environmental Consultants Inc. [42]. The estimated capacity is 100-150 MW and it is going to be deployed 40 km from the coast of Eureka, California in the US. An interesting thing about this project is the water depth of the selected site ranging from 700 to 900 m.

## 2.6 Costs of offshore wind farms

### 2.6.1 Levelized cost of energy

One of the main parameters to assess the feasibility of an energy project is the levelized cost of energy (LCOE). It is a ratio of a sum of discounted costs in a whole lifetime of an energy project to the total of the discounted annual energy produced. It can be used to determine the minimal price of electricity that a certain plant produces to cover its investment and operational costs. LCOE can be calculated using Equation 2.1 below [43, 44].

$$LCOE = \frac{\sum_{i=1}^{T}(CAPEX_i + OPEX_i + DECEX_i)\cdot(1+r)^{-i}}{\sum_{i=1}^{T} AEP_i \cdot (1+r)^{-i}}, \tag{2.1}$$

where: $LCOE$ is the levelized cost of energy; $CAPEX_i$ represents the capital expenditures in year i; $OPEX_i$ represents the operational expenditures in year i; $DECEX_i$ is the decommissioning expenditures in year i; $AEP_i$ is the annual electricity production in year i; $r$, the discount rate; $T$, the lifetime of the project.

### 2.6.2 LCOE for floating offshore wind

Recent developments in the offshore wind industry enabled to reduce the average LCOE values of offshore wind energy from 162 USD/MWh in 2010 to 84 USD/MWh in 2020 [17]. When it comes to the floating offshore market, the average LCOE was equal to 160 USD/MWh in 2020, but it is estimated that the costs will drop to 60-105 USD/MWh in 2030 according to different research organizations as it is stated in the Offshore Wind Market Report 2021 [16]. Figure 2.6 shows global LCOE per MWh forecasts for floating offshore wind projects according to different expert surveys [16]. The graph shows a significant decline in the cost of energy in the next years in all expert forecasts considered. The potential factors for costs reductions will be discussed in section 2.7 of this thesis.

### 2.6.3 CAPEX, OPEX, and DECEX of FOW projects

The total costs of floating offshore wind projects (FOW) are divided into CAPEX (capital expenditures), OPEX (operational expenditures), and DECEX (decommissioning expenditures). These costs with their specific components are presented in Figure 2.7 [44].

CAPEX are mostly fixed costs incurred in the design and installation phase of the project. They include the price of the materials and components as well as the costs of installation of turbines, floating platforms,

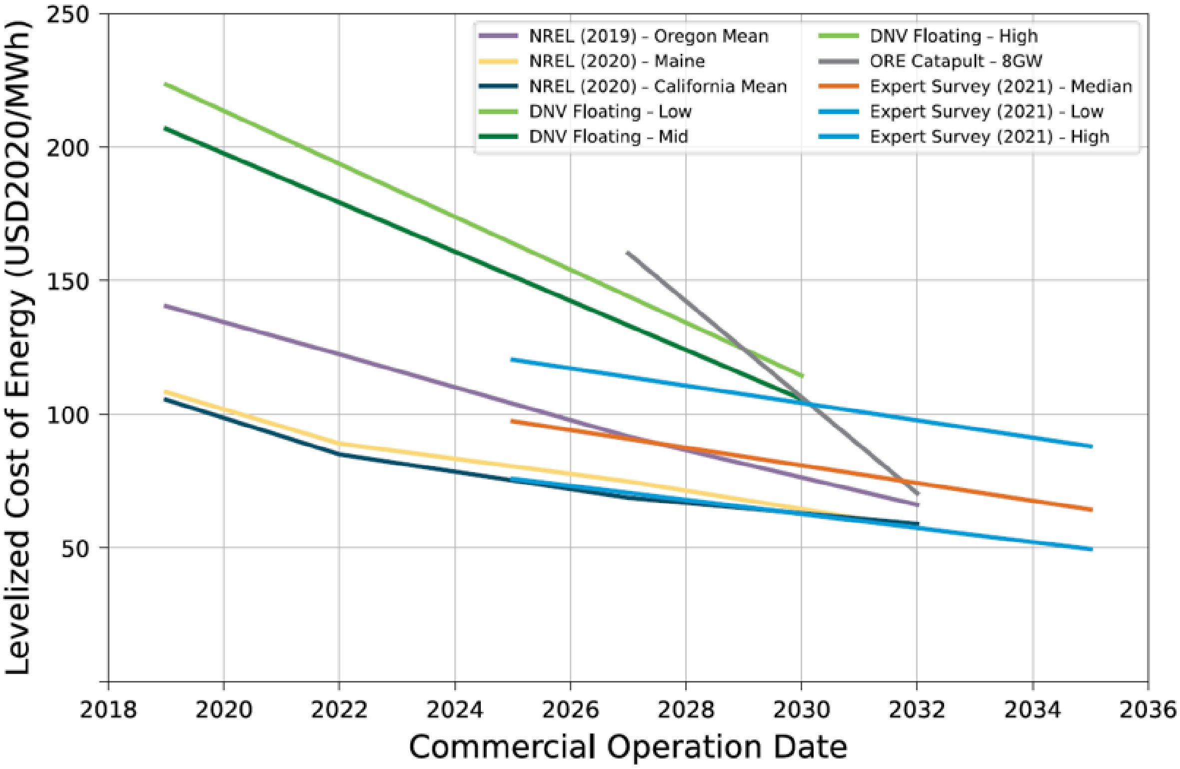

**Figure 2.6:** Global LCOE forecasts for floating offshore wind energy projects [16].

cabling, mooring, anchoring and offshore and onshore substations. The OPEX are mainly variable costs associated with the maintenance, repairs and operation. DECEX expenditures are related to the final decommissioning of the farm, which includes, for example, the disassembly, material utilization and area clearance [43, 44].

## 2.7 Cost reduction of floating offshore wind farms

Floating offshore wind technologies are still new to the commercial market, but they are becoming a highly promising and effective source of electricity. FOW will enable farm installations in deeper waters, where the wind resources are richer, thus providing more electricity and higher capacity factors. However, the overall costs and LCOE factors of floating offshore are still too high to commercially compete with fixed turbine installations [45]. Therefore, cost reduction in FOW is important to achieve. According to an expert survey led by Ryan Wiser [46], it is predicted that reductions in the LCOE will be higher in the offshore market compared to onshore wind. Additionally, the experts predict that the price gap between fixed mounting and floating platforms installations will narrow in 2035 and floating wind will become less costly than fixed-bottom installations in 2020 [46].

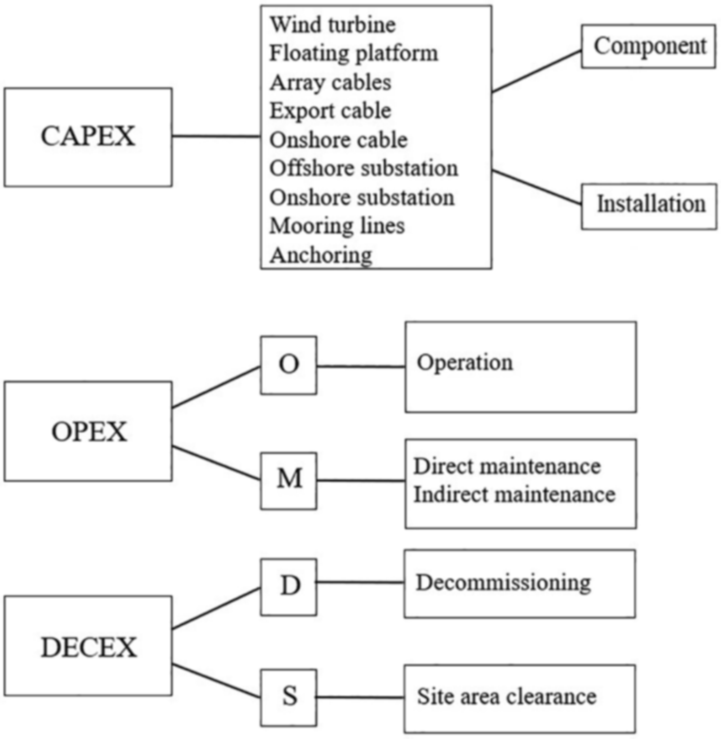

**Figure 2.7:** CAPEX, OPEX and DECEX with their subcomponents for a floating offshore wind farm [44].

### 2.7.1 Cost reduction factors

Reductions in costs of future floating offshore wind installations can accelerate through the use of innovations and experience, as well as the utilization of supply chains derived from already existing fixed-bottom turbines. FOW also allows to reduce the complexity of the construction at sea by the ability to assemble the platforms and turbines in onshore facilities. In addition to that, modularization and automation of production along with optimization of the floating offshore platforms are aiding in the reduction of the costs of manufacturing and installation [16].

Figure 2.8 shows the contribution of different cost components in every stage of a floating offshore wind farm operation with a lifetime of 25 years to the total LCOE. According to NREL's "2020 Cost of Wind Energy Review" [47], the highest contribution (27.5%) to the LCOE values are due to the OPEX. Next are the substructure and foundation (27.1%), turbines (17.6%) and electrical infrastructure (9.2%) costs, which represent the capital expenditures.

O&M are OPEX fixed and variable costs. The variable costs of O&M are dependent on the weather conditions, country, labor and energy policies, or malfunctions of the system. That is why, they may vary between the operational sites, or be difficult to predict [43]. Therefore, it may be easier to focus on the reduction of CAPEX or fixed O&M costs, such as the substructure and foundation, turbine and other components, as well as manufacturing and design processes or servicing and technical inspection costs. A study conducted by A. Martinez and G. Iglesias [43] analyses how different parameters' changes affect the LCOE of a floating offshore farm. The main factors presented in the paper that contribute to a

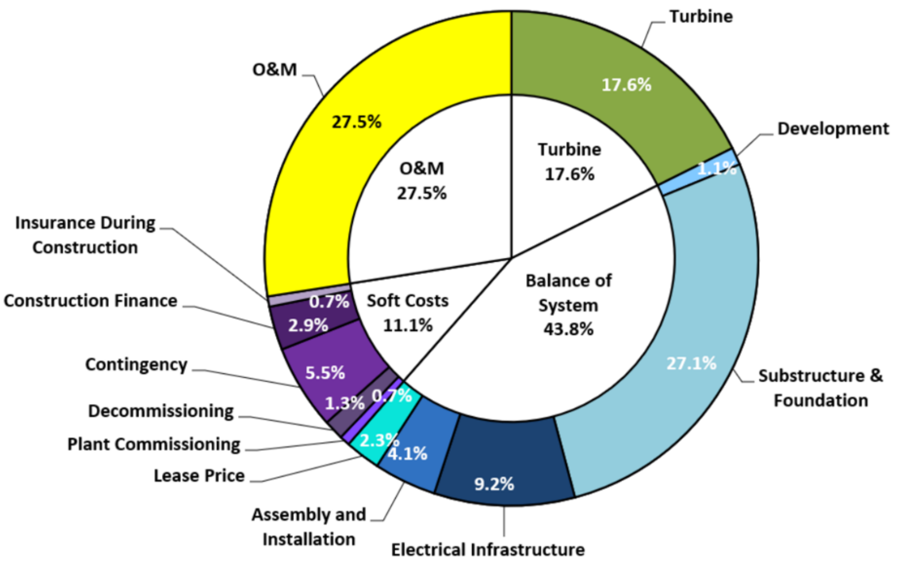

**Figure 2.8:** Contribution of different cost components to LCOE for floating offshore wind reference farm operating for 25 years [47].

reduction of the levelized cost of energy are turbine nominal power, project lifetime, cost of the turbines, cost of the substructures, fixed OPEX components, and discount rates [43].

Turbine innovations and upscaling for the offshore wind sector are being done by different producers. The most relevant factors in turbine innovations when it comes to LCOE reduction are improvements in blade design and manufacturing, modularity for easier assembly, increased lifetime of the design, or new turbine-substructure connections [48]. Another important aspect is a smart and integrated wind farm design and control that consider wake effects [49].

Apart from the above aspects, other important technology-related, cost-reduction factors include manufacturing and material costs of floating platforms; higher voltage cables, to reduce transmission losses; shared mooring and anchoring systems for several platforms in a farm; standardization of supply chain; innovation in cable installation methods; specialized vessels and tugboats for installation [48, 50].

Fixed O&M costs can be reduced by: integrated monitoring systems, which operate on a condition-based principle with different sensors and data for every turbine; digitalization of the monitoring system; repair and monitoring using drones and robots; commissioning a floating service island, which can significantly reduce the distance from the wind farm to the nearest maintenance point and enables easier access to the installation [48].

Discount rates, mentioned in Equation 2.1 also have a significant impact on the LCOE values in a wind project. The most commonly used discount rate is calculated as the weighted average cost of capital (WACC) [48]. It is used to measure the cost of capital and net present value (NPV) of a project and indicate the risk of an investment. It is estimated that the risk of FOW investments and consequently the WACC values will decrease from 8% to 4% in 2040 in advanced economies [48]. However, the present (2022) economic situation combined with the post-COVID-19 influence and the Russian invasion on Ukraine may have a significant impact on the cost of capital values [51]. These potential effects are not considered in this work.

### 2.7.2 Wind farm layout

One of the factors that have the highest significant impact on LCOE values is the amount of electricity produced. Therefore, increasing the energy yield from a wind farm enables a substantial decrease in the levelized costs of energy. One of the ways to do it, identified in the literature [43, 45, 48], is the upscaling of wind turbines which increases their nominal power. Other solutions revolve around mitigating the energy losses caused by environmental factors (blades icing or soiling), electrical losses, technical losses (rotor misalignments, hysteresis) and wake losses.

Wake losses and turbine interactions between each other can significantly impact the energy yield from a system by reducing the power generation by 10-20% [52]. Wake is created behind a wind turbine when it uses the wind momentum to move its blades. It results in reduced wind speed and an increase in wind turbulence downstream from the turbine. These impose lower power generation and increased fatigue loads in turbines that are in the wake of other turbines [45, 52]. Proper wind farm layout and design that includes the wake effect and interactions between turbines in a farm can reduce the energy losses and therefore increase the energy yield in the whole system [48].

Several studies [53, 54, 55] take into consideration the variations in the turbine spacing in a wind farm as a solution to the wake losses reduction. As with the increasing distance from the turbine, the turbulence in the wind starts to recover under the ambient wind influence, increasing the turbine spacing in subsequent rows of a farm can reduce wake losses [56, 57]. Michael F. Howland et al. [54] have found that the optimal turbine streamwise spacing is 10D - 15D (D standing for the turbine rotor diameter), when it comes to the wake losses reduction. However, extending the distance between turbines leads to increased costs of the transmission lines and landlease, which based on the research [54] leads to an optimal 6D to 10D turbine spacing. Al-Addous Mohammad et al. [55] have shown that increasing the turbine spacing distance from 2.5D to 5D can decrease the wake losses by 8.29% to 8.46%, depending on the farm layout. Andrew P.J. Stanley et al. [53] have examined the turbine spacing impact, using different wind shear exponents and different turbine heights and in each of the analyzed cases, increasing the turbine spacing resulted in a decrease in wake losses and LCOE values, considering spacings of 2D up to 10D.

Another wake losses and LCOE values reduction factor examined in literature [55, 58, 59, 60] is the different geometrical layout of wind farms. The research done by Al-Addous Mohammad et al. [55] that different shapes of wind farms can have an impact on total electricity generation and wind farm wake losses. Niranjan S. Ghaisas and Cristina L. Archer [58] have shown that non-orthogonal wind farm layouts may decrease the wake losses and increase the energy yield from a farm. However, the LCOE values, impacted by transmission lines and other factors have not been exactly determined in this study. Ajit C. Pillai et al. [60] study examined different wind turbines arrays and has shown that the wind farm layout has a great impact on the annual electricity production and LCOE values.

### 2.7.3 Tower hub height

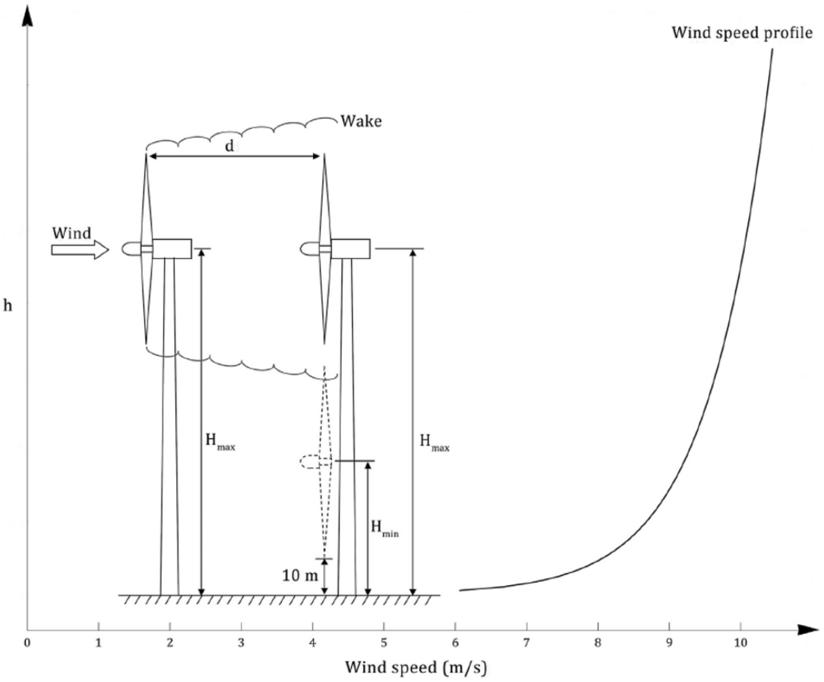

**Figure 2.9:** Wind turbines hub height optimization concept to reduce the wake effects [61].

Ahmadreza Vasel-Be-Hagh et al. [61] mention different studies aiming to minimize the wake effect in wind farms by differentiation in turbines hub height. Lowering the hub height of the next turbine in a line makes it partially reduces the wake streamtube superposition created by a preceding turbine. However, a lower turbine experiences lower wind speeds due to the shear effect of the surface, which reduces the electricity production by this turbine. Figure 2.9 illustrates the concept of wake losses reduction by hub height optimization [61]. As the wake mixes with free-stream layers outside of the wake streamtube, at some distance the wake is mitigated and the stream is the same as the free-stream wind [45]. Therefore, theoretically, the next turbine in a line can have the same height as the first turbine, with the turbine hub heights alternating from a higher to a lower one. Using the two different hub heights, simulations done by Ahmadreza Vasel-Be-Hagh et al. [61] resulted in a potential average power production increase in a wind farm by around 9.5%.

### 2.7.4 Floating platform cost reduction

Floating structures, especially semi-submersible platforms, in order to satisfy their design requirements and provide a good foundation that can hold the weight of the turbine and system components, require an extensive amount of materials, such as steel, ballast material, concrete or welds and flanges [50]. The material costs depend on the mass of the platforms, and the unit price of the materials [44]. Reduction of the size of the platforms can significantly reduce the CAPEX, thus reducing the LCOE values for floating offshore platforms. Initial costs of the platform are related to the labor costs, which include preparation, prefabrication, construction of the platform, and the employees' salaries [44]. Industrialization and upscaling of manufacturing processes can help reduce the component preparation costs for the platform.

Size reduction of FOW platforms has to be done, however, in such a way that they maintain their stability, comply with their operating conditions' requirements and are able to withstand extreme weather conditions. The most important factors to consider in the floating platforms' costs reductions are their metacentric height, static pitch angle, floating equilibrium, dynamic and static stability [50]. Additionally, the platforms need to be able to hold the whole system and turbines weight. During the rapid development and upscaling of offshore wind turbines, their weight will increase, which may require larger and more robust platforms [50].

Efforts in the design and testing of new ”light” platforms have been made in order to reduce foundation costs in new floating offshore wind projects. One of the examples is the Hexicon [62] TwinWind floating platform concept, which enables the installation of two turbines on one platform, increasing the wind farm power density and reducing the environmental impact of wind farms. It can support different major offshore wind turbines ranging from 3 MW to 16 MW of power [62]. Another example is the X1Wind [63], which came up with a light and scalable platform, that, due to a single point mooring system and a downstream wind turbine, can self-orientate itself to the wind direction, thus increasing the utilization of wind resources. Another company worth mentioning is Stiesdal [64], which presented the TetraSub, TetraTLP, and TetraSpar solutions, which are based on the semi-submersible, tension-leg, and spar-buoy platforms, respectively. They aim to reduce floating platforms costs by creating platforms that are fast-assembled in port, enable easy turbine installation, and their production is based on industrial manufacturing using an existing supply chain [64].

## 2.8 Blade element momentum theory

Blade element momentum theory (BEMT) is a combination of the general momentum theory (MT) and the blade element theory (BET) and is a model used to evaluate the performance of a moving turbine based on its geometric and mechanical properties, and the inflow wind characteristics [65].

In the axial momentum theory, the conservation laws of mass, axial momentum and energy, presented on Equations 2.2, 2.3 and 2.4 [66], respectively, are applied to a 1D streamtube, presented in Figure 2.10 [66], where the rotor is modelled as a hypothetical disc, that exerts an axial force on the flow [66]. The main purpose of this theory is to find the axial force on the disc and axial induced velocity (velocity reduction in the rotor plane caused by the energy extracted by the actuator disc), represented by an axial induction factor $a_{\text{BEM}}$.

$$\dot{m} = \rho U_1 A_1 = \rho U_{\text{d}} A_{\text{R}} = \rho U_4 A_4, \tag{2.2}$$

$$\dot{m}(U_4 - U_1) = F_{\text{ax}}, \tag{2.3}$$

$$\dot{m}\left(\frac{1}{2}U_1^2 - \frac{1}{2}U_4^2\right) = P_{\mathrm{disc}} = F_{\mathrm{ax}}U_{\mathrm{d}}, \tag{2.4}$$

where $\dot{m}$ is the mass flux; $U_X$ at the $X$ position, $A_X$ at the $X$ position, $A_{\mathrm{R}}$ (rotor area), $F_{\mathrm{ax}}$ (axial force), $U_{\mathrm{d}}$ (fluid velocity at the disc) are defined based in Figure 2.10, and $P_{\mathrm{disc}}$ equals to the energy absorbed by the actuator disc. The mass flux in the streamtube can be written as:

$$\dot{m} = \rho V_{\mathrm{w}}(1 - a_{\mathrm{BEM}})A_{\mathrm{R}}, \tag{2.5}$$

where $V_{\mathrm{w}}$ is the inflow wind velocity.

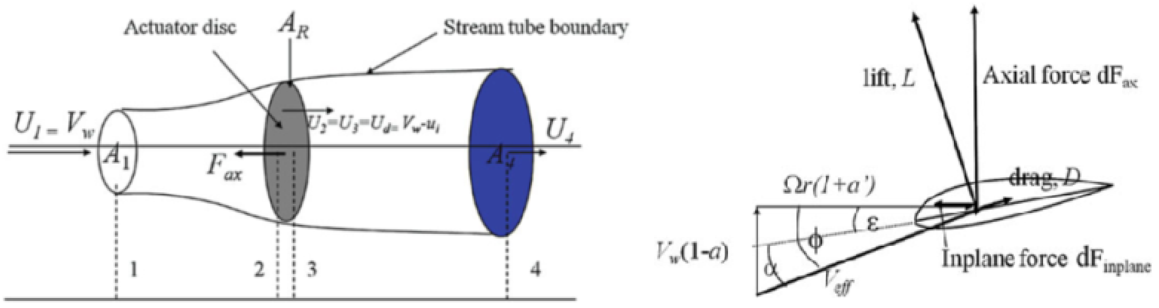

**Figure 2.10:** Blade element momentum theory [66]. The left picture shows the 1D streamtube used in the axial momentum theory, where: 1 is the far upstream location, 2 and 3 are placed at an infinitely small distance upstream and downstream from the disc, and 4 represents the far downstream location. The picture on the right presents the lift, drag, and velocity diagram of the blade element theory.

Combining the equations above leads to a relation between the axial force and the axial induction factor [66] presented as

$$F_{\mathrm{ax}} = \rho V_{\mathrm{w}}^2 2a_{\mathrm{BEM}}(1 - a_{\mathrm{BEM}})A_{\mathrm{R}}. \tag{2.6}$$

The power coefficient $C_{\mathrm{p}}$ and the axial induction factor relation can be represented as

$$C_{\mathrm{p}} = 4a_{\mathrm{BEM}}(1 - a_{\mathrm{BEM}})^2, \tag{2.7}$$

where $C_{\mathrm{p}}$ is defined as

$$C_{\mathrm{p}} = \frac{P}{\frac{1}{2}\rho V_{\mathrm{w}}^3 A_{\mathrm{R}}}. \tag{2.8}$$

In the blade element theory, the lift and drag forces on specific turbine blade elements are calculated based on the airfoil lift $c_l$ and drag $c_d$ coefficients [66, 67]. The coefficients are a function of the angle of attack $\alpha$ (angle between the incoming wind and the airfoil chord line $c$), the Reynolds, and Mach number. The lift force $F_{\mathrm{L}}$ and the drag force $F_{\mathrm{D}}$ on the blade elements are presented in Equations 2.9 and 2.10 respectively [66].

$$F_{\mathrm{L}} = c_l(\alpha)\frac{1}{2}\rho V_{\mathrm{eff}}^2 c, \tag{2.9}$$

$$F_{\mathrm{D}} = c_d(\alpha)\frac{1}{2}\rho V_{\mathrm{eff}}^2 c, \tag{2.10}$$

where $V_{\mathrm{eff}}$ is the effective velocity found from a so-called velocity triangle, presented in Figure 2.10. The drag force leads to a velocity change in the wake behind the blade element, which is not considered to be part of the induced velocity. Therefore, it may not be included in the axial force calculation [66]. Then, the lift force is used to compute the axial force on a ring formed by rotating a specific blade element as

$$dF_{\mathrm{ax}} = F_{\mathrm{L}} \cos(\phi)\, dr, \tag{2.11}$$

where dr is the blade element, $\phi$ is the inflow angle, calculated based on the velocity triangle, presented in Figure 2.10, and rotational speed of the actuator $\Omega$, as

$$\phi = \arctan[V_{\mathrm{w}}(1 - a_{\mathrm{BEM}})/\Omega r]. \tag{2.12}$$

Combining the axial momentum theory and BET, an axial blade element momentum relation is derived and presented as

$$4a_{\mathrm{BEM}}(1 - a_{\mathrm{BEM}})V_{\mathrm{w}}^2 = \sigma V_{\mathrm{eff}}^2 c_l(\alpha)\cos(\phi), \tag{2.13}$$

where $\sigma$ is the local solidity of the blade element.

In the general momentum theory, the angular momentum theory is added to the axial theory. The angular momentum theory considers the rotational motion of the actuator disc, which impacts the rotational component of the wind flow in the streamtube. The theory uses a tangential induction factor $a'_{\mathrm{BEM}}$, which relates to the tangential induced velocity due to the rotational speed of the rotor [66, 68]. The rotational wind flow component impacts the calculations of axial force (thrust) and tangential force (torque) acting on the actuator disc. The angular momentum theory is based on the laws of conservation of mass, angular momentum, and energy [66, 69].

Combining the angular momentum theory and BET, a tangential blade element momentum relation, presented in Equation 2.14, is derived [66].

$$4a'_{\mathrm{BEM}}(1 - a_{\mathrm{BEM}})V_w \Omega r = \sigma V_{\mathrm{eff}}^2 c_l(\alpha)\sin(\phi). \tag{2.14}$$

Based on the axial 2.12 and tangential 2.14 BEM equations, the axial and tangential induction factors are solved iteratively [67, 66].

## 2.9 Wake models used for farms' assessment

The study of wind turbine wakes usually involves two distinctive regions, one being close to the rotor (near wake) and another one being farther from the rotor (far wake). Near wake is the turbulence occurring right behind the rotor and extending to around 2-4 rotor diameters [56] or even up to 6D [70] downstream. It is influenced by rotor geometry, blade aerodynamics, the number of blades, or stall effects. Far wake is the turbulence occurring farther downstream of the rotor, and it influences other turbines in a farm. At the far wake distance, the turbulence in the wind starts to recover under the ambient wind influence. In the far wake, the most important aspects are the wake interaction and turbulence physics, which include reduced wind speeds and increased turbulence [56, 57].

One can distinguish many wake effect models, which include both simpler analytical, and more complex, computer-aided solutions. Analytical models examples include the Jensen model, the Jensen-2D model, or the Frandsen model [56]. Computer-aided models require the usage of computational fluid dynamics (CFD) simulations and are commonly based on either Reynold's-averaged Navier-Stokes (RANS) or Large Eddy Simulation (LES) models [71, 72]. Examples of the RANS-based models include the Larsen Model or Dynamic Wake Meandering (DMW) model [56].

### 2.9.1 Jensen Wake Model

The Jensen wake model is a solution created in the 1980s based on Jensen's (1983) [73] and Katic's (1987) [74] published works. It is a simple analytical turbulence model that considers a top-hat, linear expansion of the wake radius described by Equation 2.15 [75]. It is one of the most popular engineering wake models due to its simplicity and practicality [56]. It is used in many commercial software packages, such as WindSim, OpenWind, or WindPRO [76].

$$r_x = r_d + k_{\text{Jensen}}, \tag{2.15}$$

where $r_x$ is the wake radius at the $x$ distance from the turbine; $r_d$ is the turbine rotor radius; $k_{\text{Jensen}}$ is a semi-empirical wake decay constant, typically valued at 0.05 for offshore application [76]. It can be calculated using Equation 2.16 [76].

$$k_{\text{Jensen}} = \frac{0.5}{\ln(\frac{z}{z_0})}, \tag{2.16}$$

where $z$ is the height of the wind turbine hub and $z_0$ is the surface roughness of the terrain.

Wake velocity at an $x$ distance can be expressed using the axial induction factor $a$ derived from the thrust coefficient $C_t$ and a semi-empirical wake decay constant. It is represented by Equation 2.17 [75].

$$u^* = u_0 \left( 1 - \frac{2a}{(1 - \frac{k_{\text{Jensen}}}{r_1})^2} \right), \tag{2.17}$$

where $u^*$ is the wake velocity at a distance $x$ from the turbine; $u_0$ is the undisturbed inflow wind velocity and $r_1$ is the expanded wake radius immediately after the turbine rotor.

### 2.9.2 Jensen-2D_k Wake Model

Réthoré [77] highlighted that the original Jensen model appeared to be very inaccurate in the near wake region, but it showed proper results after 6 rotor diameters' distance. Carrying out a more detailed wake investigation and representing accurate near wake distribution required advancements to the Jensen model. In 2015, Tian et al. [75] proposed a correction to the Jensen model, in which they derived the velocity profile using a sinusoidal distribution rather than a top-hat one [75]. It is based on three assumptions added to the original Jensen model. The first assumption states that the wake radius is derived in the same way as in the original model. The second assumption implies that the mean wind velocity reaches the free-stream wind velocity whenever the radial distance from the wake center tends to the outer boundary of the wake region. The last assumption considers the mass flow rate calculated in the 2D_k model to be the same as the one estimated in the original model [75]. The 2D_k model takes two steps: calculating the wake speed using the first Jensen model; and then, applying it to the 2D_k model velocity cosine function, which can be described using Equation 2.18 [75].

$$u = (u_0 - u^*)\cos\left(\frac{\pi}{r_x} r_{\text{Jensen}} + \pi\right) + u^*, \tag{2.18}$$

where $u$ is the new model wake velocity; and $r_{\text{Jensen}}$ is the radial distance from the wake center.

### 2.9.3 Frandsen Wind Deficit Model

The Frandsen wind deficit model [78] is another top-hat, linear wake expansion model commonly used in different engineering applications, that is based on an analysis of control volume [76]. The model's wake expansion radius $r_x$ at the distance $x$ from the turbine is given by Equation 2.19 [79].

$$r_x = r_d \left(\beta_{\text{Frandsen}}^{k_{\text{Frandsen}}/2} + \alpha_{\text{Frandsen}} \frac{x}{2r_d}\right)^{1/k_{\text{Frandsen}}}, \tag{2.19}$$

where $\beta_{\text{Frandsen}}$ is an initial expansion rate coefficient dependent on the thrust coefficient $C_t$ described by Equation 2.20 [79]; $k_{\text{Frandsen}}$=2 is the shape parameter and $\alpha_{\text{Frandsen}}$ is the expansion constant, which needs to be calibrated [76].

$$\beta_{\text{Frandsen}} = \frac{1 + \sqrt{1 - C_t}}{2\sqrt{1 - C_t}}. \tag{2.20}$$

Wake velocity $u$ in the Frandsen model is described by Equation 2.21 [79].

$$\begin{aligned} u &= \frac{u_0}{2}\left(1 + \sqrt{1 - 2\frac{A_0}{A}}\right) \quad a <= 0.5 \\ u &= \frac{u_0}{2}\left(1 - \sqrt{1 - 2\frac{A_0}{A}}\right) \quad a > 0.5 \end{aligned} \tag{2.21}$$

where $A_0 = \pi r_d^2$ and $A = \pi r_x^2$.

### 2.9.4 CFD-aided Wake Models

In the past 40 years CFD solutions have gained the interest of scientists when it comes to modeling the aerodynamics of wind turbines. With the aid of high-performance computers, they enabled the researchers to gain more insight into more complex physics of wind turbulence near the turbine blades and develop quick aerodynamics models. The basics of CFD solutions include proper solving grid generation, boundary layer turbulence modeling, and solution of flow equations [71]. CFD wake models are usually based on RANS or LES solutions. RANS uses Reynolds averaging which allows the simplification of the Navier-Stokes (NS) equations [71]. LES introduces sub-grid scale turbulence modeling in order to directly solve Navier-Stokes equations in larger scales [72]. RANS solutions are commonly applied in industrial applications, where fast and simple results are expected, whereas LES solutions are mainly used in research studies to thoroughly analyze the wake flow mechanisms and wake interactions [80].

In the LES solutions, due to a dense grid and sub-grid Scaling (SGS), which can represent small-scale fluid turbulences, the analytical reduction of the equations can be simpler. However, because of the small scale of the solution, high computational power is needed and the simulations can take much longer compared to RANS solutions [71].

### 2.9.5 Larsen Wake Model

The Larsen wake model was proposed by Gunner Larsen in 1988 [81] and further developed by the same author in 2009 [82]. It is a model based on the thin shear layer approximation of the axis-symmetric form of the RANS equations [56]. The later version of the model defines two empirically-derived boundary conditions: at the rotor plane and at a distance of $R_{9.6}$=9.6 turbine diameters downstream. The radius of the wake $r_x$ is represented by Equation 2.22 [56] and the axial wake velocity $u_x$ is found using Equation 2.23 [56].

$$r_x = \left(\frac{35}{2\pi}\right)^{1/5} \left(3c_1^2\right)^{1/5} \left(C_t A(x+x_0)\right)^{1/3}, \tag{2.22}$$

$$u_x = -\frac{U_0}{9}\left(C_t A(x+x_0)^{-2}\right)^{1/3}\left(r^{3/2}(3c_1^2 C_t A(x+x_0))^{-1/2} - (\frac{35}{2\pi})^{3/10}(3c_1^2)^{-1/5}\right)^2, \tag{2.23}$$

where $c_1$ is determined by Equation 2.24; $x_0$ can be found using Equation 2.25; and $d_1$ used in Equation 2.25 can be obtained using Equation 2.26 [56].

$$c_1 = \left(\frac{105}{2\pi}\right)^{-1/2}\left(\frac{d_1 D}{2}\right)^{5/2}\left(C_t A x_0\right)^{-5/6}, \tag{2.24}$$

$$x_0 = \frac{9.6D}{\left(\frac{2R_{9.6D}}{d_1 D}\right)^3 - 1}, \tag{2.25}$$

$$d_1 = \sqrt{\frac{1+\frac{1}{\sqrt{1-C_t}}}{2}}. \tag{2.26}$$

### 2.9.6 Dynamic Wake Meandering Model

The Dynamic Wake Meandering model is based on passive-tracing of the wake caused by the large-scale turbulence structures. It is divided into three main components: quasi-steady wake deficit, wake meandering, and small-scale rotor-induced turbulence [56, 83].

The wake velocity deficit part is based on Navier-Stokes equations with their pressure components in the thin shear layer neglected. The resulting equations are presented in Equation 2.27 and Equation 2.28

[56].

$$U \frac{\partial U}{\partial x} + V_r \frac{\partial U}{\partial r} = \left(\frac{\nu_t}{r}\right) \frac{\partial}{\partial r} \left[ r \frac{\partial U}{\partial r} \right], \tag{2.27}$$

$$\frac{1}{r} \frac{\partial}{\partial r} (r V_r) + \frac{\partial U}{\partial x} = 0, \tag{2.28}$$

where $V_r$ is the mean velocity in the radial direction $r$. Eddy viscosity used in the model can be determined using Equation 2.29 [56].

$$\nu_t = F_2 k_{\text{DWM}} \left( \frac{b_{\text{DWM}}}{r} \right) \left( 1 - \frac{U_{\text{def,min}}}{U_{\text{H}}} \right) + F_1 k_{\text{Amb}} I_{\text{Amb}}, \tag{2.29}$$

where $k_{\text{DWM}}$ is the flow field constant in the DWM model; $b_{\text{DWM}}$ is the instantaneous wake half width; $U_{\text{def,min}}$ is the minimal wake velocity; $U_{\text{H}}$ is the hub height wind speed; $I_{\text{Amb}}$ is the hub height ambient intensity of the turbulence; $k_{\text{Amb}}$ is a constant for calibration in the DWM model, and $F_1$ and $F_2$ are downstream distance-dependent filter functions [56].

Another component of the DWM model is wake meandering, which is based on the large scales of turbulence in the ambient wind flow. Wake position deficits are dependent on the fluctuations of wind speed in horizontal $y$ and vertical $z$ distance at the hub height. It is described by Equations 2.30 and 2.31 for the horizontal and vertical direction respectively [84].

$$\frac{dy(t)}{dt} = v(t), \tag{2.30}$$

$$\frac{dz(t)}{dt} = w(t). \tag{2.31}$$

The last element of the DWM model is the small-scale, rotor-induced turbulence. It is modeled with the Mann turbulence box and the intensity of added turbulence does not influence the previous two components of the model [56]. The additional turbulence is caused by root and tip blades' vortexes [84].

## 2.10 Tools and software

### 2.10.1 OpenFAST

OpenFAST is an open-source wind turbine simulation software developed by the National Renewable Energy Laboratory (NREL) in the U.S. Department of Energy [85]. It is used to conduct computational simulations of wind turbines and floating offshore wind platforms operation with regards to aerodynamics, hydrodynamics of offshore structures, electrical system, and structural dynamics components. It enables dynamic simulations of inter alia: wind turbine's generated power, torque on the generator, force moments exerted on the turbine tower, or floating platform displacements considering several degrees of freedom. It is combined with pre- and post-processors, such as the TurbSim package, which can generate turbulent wind inflow conditions' models for OpenFAST simulations [85, 86]. In this thesis, OpenFAST v3.1.0 was used to conduct simulations of different turbine and floating platform combinations in order to determine the power generated on the turbine and the dynamics of the platform in several wind speed conditions.

### 2.10.2 FAST.Farm

FAST.Farm is an open-source tool developed by NREL that supplements OpenFAST to dynamically simulate power performance and structural loads of turbines in a wind farm [21]. OpenFAST software is used to simulate the dynamics of each turbine in a farm and then FAST.Farm additionally takes into account the physics of wind farms, such as ambient wind, controllers, wake effects and losses on each turbine, deflection, advection, merging, and meandering. The tool can be used to determine wind farm electricity generation, its under-performance due to environmental losses, or the impact of turbines on each other; enhance the efficiency of the wind farm; optimize the topology of wind farms; and increase the wind farm environment performance. It can simulate wake-deficit evolution that is used to determine performance and wake-added turbulence used to calculate additional loads on the turbines [21]. In this thesis, FAST.Farm is used to determine the performance of wind farms in different operating conditions and with diversified farm layouts.

### 2.10.3 FAST.Farm wake dynamics (WD) model

FAST.Farm WD module operating principles rely on the dynamic wake meandering model, described in the previous section of this chapter. It is based on the three main DWM model principles, namely wake-deficit, wake meandering, and near-wake correction [21].

The wake deficit is modeled by the thin shear-layer approximation of the RANS equations in axi-symmetric coordinates under quasi-steady-state conditions and the turbulence is modeled using the eddy viscosity approach. This wake-deficit model is only valid in far wake [21], so in order to improve the far-wake accuracy, near-wake correction is added in the inlet boundary conditions.

The wake meandering model is extended to address wake deflection and wake advection in the passive tracer solution. The extensions are introduced by, inter alia, calculating velocities for different wake planes, orientating the wake planes with the rotor centerline, and low-pass filtering local rotor conditions to account for inflow transients, turbine control and turbine motion [21].

Near-wake correction in FAST.Farm accounts for wind speed drops and radial expansions of the wake in the pressure-gradient zone behind the rotor. It is computed differently for low- ($C_t < \frac{24}{25}$) and high-thrust ($1.1 < C_t \leq 2$) conditions with the zone between those regions being blended linearly based on the $C_t$ value. At low-thrust conditions, the axial and radial wake-velocity deficits are derived from axial induction factor $a_{\text{BEM}}$, derived from the blade element momentum theory (BEMT), and low-pass time-filtered rotor-disc-averaged relative wind speed. At high-thrust conditions, the axial wake-velocity deficit is derived by a Gaussian fit to LES solutions at high thrust [21]. The FAST.Farm Wake Dynamics model additionally addresses different DWM model limitations and provides solutions for them. In order to examine them, see the FAST.Farm manual chapter: 4.2.15.7. FAST.Farm Theory [21].

In addition to the Wake Dynamics module, FAST.Farm uses a super-controller (SC) and an ambient wind and array effects (AWAE) module [21]. The SC module is a controlling module that can reduce the turbine mechanical loads and decrease the wake effects on turbines' performance by changing the blade pitch, generator torque, and nacelle's yaw or tilt. The AWAE module is used to determine the ambient wind and wake interactions, which include the wake-merging and ambient wind submodels, in the wind farm. The ambient wind submodel uses the InfloWind module in the software, which can utilize synthetically generated wind data, using TurbSim software, that can simulate a full-field turbulent wind across a selected grid. Compared to the other commercially available turbulence intensity models, the ambient wind AWAE submodel uses a uniform three-vector components spatial average. Because of that, the ambient wind averaging can be omitted, which leads to decreased computational memory requirements. The spatial averaging allows the atmospheric shear and other ambient wind attributes to influence the wake-deficit and the eddy viscosity evolution in the wake dynamics module. The usage of the AWAE module enables two-way wake-merging interactions, which were not used in the previous DWM implementations. It identifies the overlaps of wakes across the analyzed wind farm and uses the RSS method, described in [87], to sum the local kinetic energies of the wake axial deficits for each wake at a specific wind data point. The AWAE model computes the deflection, advection and meandering velocity of different wake planes as the weighted spatial average of the disturbed wind velocity [21].

FAST.Farm uses two domains - a low- and a high-resolution one to simulate different aerodynamic properties. A high-resolution domain is used nearby the turbine rotor to simulate the rotor yawing, blade deflection, and the support structure motion along with its loads. The low-resolution domain is needed because of the spatial averaging across different wake planes and in order to save computational power in the wind farm regions that do not require a dense grid and detailed wind and turbulence interpolations.

# Chapter 3

# Description of the reference base case

The purpose of this Chapter is to describe the reference wind farm case (base case). The Chapter presents the floating platform and the turbine used in the reference case, the selected wind farm location, and the wind and wave resource characteristics of the location. It also shows the reference wind farm layout, connection, and specifications.

## 3.1 Floating platform

The floating platform used in this work is the OC4 semi-submersible platform proposed by NREL [88]. The platform consists of a main column of 6.5 m in diameter, which poses as the base of the turbine tower and is connected by structural members to three offset columns in a triangle formation. The columns' diameter is equal to 12 m. Each of the columns has a larger, 24 m in diameter, cylinder which helps to minimize the heave, sway, pitch, roll and surge motions. The offset columns are filled with ballast water in order to improve the platform stabilization. In order to secure them, each of the platforms is connected to three mooring lines which are mounted to the seabed using anchors. The structural design of the platform with its main dimensions is presented in Figure 3.1 [88]. The summary of structural and hydrodynamic platform properties is presented in Table 3.1 [88].

**Table 3.1:** NREL OC4 semi-submersible platform structural and hydrodynamic properties [88].

| Property | Value | Unit |
|---|---|---|
| Platform mass, including ballast kg | $1.347 \times 10^7$ | kg |
| Total structure mass | $3.852 \times 10^6$ | kg |
| CM location below SWL | 13.5 | m |
| Platform roll inertia about CM | $6.827 \times 10^9$ | $kg \cdot m^2$ |
| Platform pitch inertia about CM | $6.827 \times 10^9$ | $kg \cdot m^2$ |
| Platform yaw inertia about CM | $1.226 \times 10^{10}$ | $kg \cdot m^2$ |
| Platform draft | 20.0 | m |

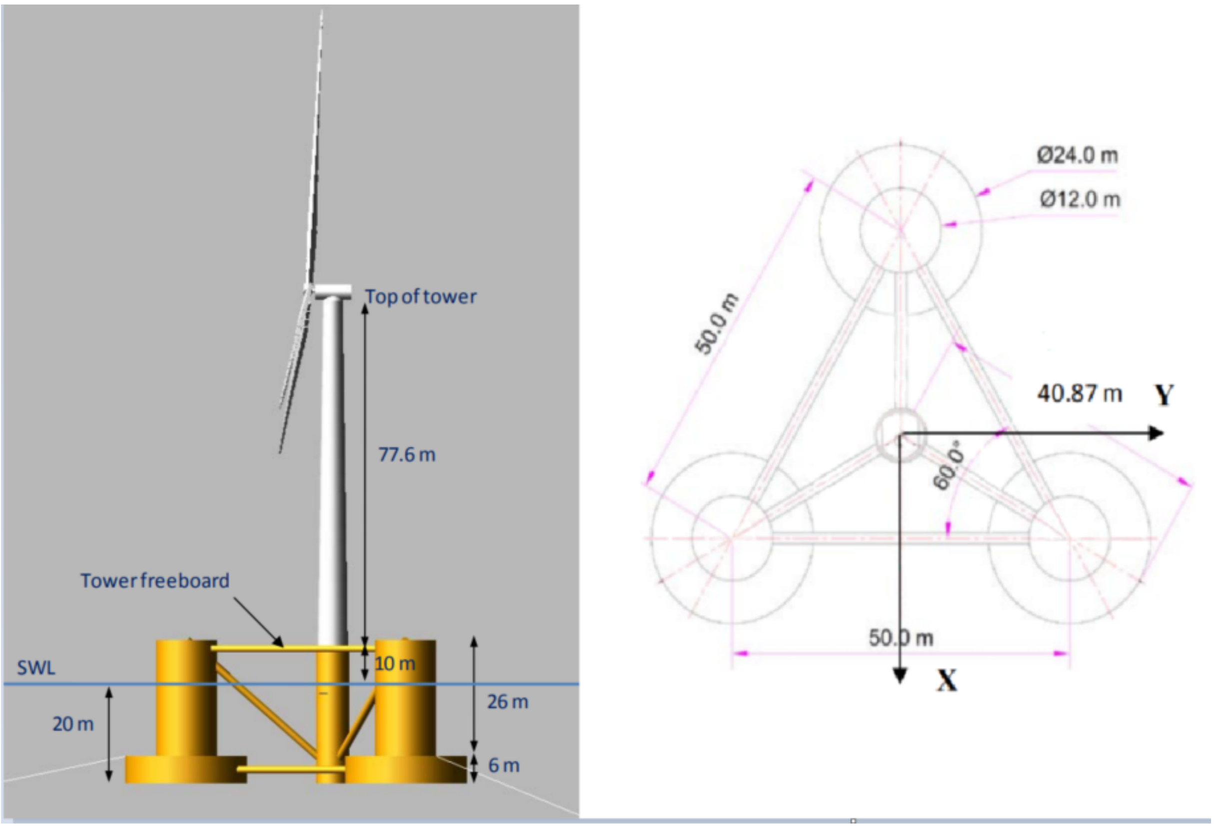

**Figure 3.1:** Design of the NREL semi-submersible platform with 5 MW NREL turbine. Left: Side-view overall design; right: Top view plan of the platform [88].

### 3.1.1 Platform mooring system

In order to secure the platform, three catenary lines are symmetrically spread about the platform $z$-axis. The angle between the mooring lines is $120^o$. Each of the mooring lines has a length equal to 835.5 m and their mass density is equal to 113.35 kg/m [88]. The main mooring lines' properties are presented in Table 3.2.

**Table 3.2:** NREL OC4 semi-submersible platform mooring lines properties [88].

| **Property** | **Value** | **Unit** |
|---|---|---|
| Number of mooring lines | 3 | - |
| Angle between the mooring lines | 120 | $^o$ |
| Mooring lines' length | 835.5 | m |
| Mooring lines' diameter | 0.0766 | m |
| Mooring line mass density | 113.35 | kg/m |
| Mooring line mass density in water | 108.63 | kg/m |
| Mooring line extensional stiffness | 753.6 | MN |

## 3.2 Wind turbine

The U.S. National Renewable Energy Laboratory (NREL) 5 MW reference horizontal axis wind turbine, was selected for the analysis in this study. The NREL 5 MW reference turbine has been extensively investigated in both onshore and offshore conditions [89]. The data in Table 3.3 shows some of the main specifications of the turbine, including the rotor, hub, and tower of the turbine, as well as information on the cut-in and cut-out Wind Speed [89].

**Table 3.3:** NREL 5 MW wind turbine specifications [89].

| Property | Value | Unit |
|---|---|---|
| Power rating | 5 | MW |
| Rotor diameter | 126 | m |
| Hub diameter | 3 | m |
| Hub height | 90 | m |
| Cut-in wind speed | 3 | m/s |
| Rated wind speed | 11.4 | m/s |
| Cut-out wind Speed | 25 | m/s |
| Cut-in rotor Speed | 6.9 | rpm |
| Cut-out rotor Speed | 12.1 | rpm |

The length of the turbine tower is equal to 87.6 m and the diameter of its base is equal to 6 m. The distance between the center of the rotor and the top of the tower is 2.4 meters. This means that its hub is placed at a height of 90 m measured from its base. It is equipped with three blades, each being 61.5 meters long. The turbine is controlled by two independently operating systems: a generator torque controller and a rotor-collective blade-pitch controller [89].

The turbine nominal rotor speed and blade pitch angle for each wind speed class is presented in Table 3.4 [89]. The values are going to be used later in FAST.Farm as turbine initial conditions.

**Table 3.4:** NREL 5 MW turbine rotor speed and pitch angle values for different wind speed classes that are used as the simulations' initial conditions [89].

| Wind speed (m/s) | Rotor speed (rpm) | Pitch angle (°) |
|---|---|---|
| 3.0 - Cut-In | 6.97 | 0.00 |
| 4.0 | 7.18 | 0.00 |
| 5.0 | 7.51 | 0.00 |
| 6.0 | 7.94 | 0.00 |
| 7.0 | 8.47 | 0.00 |
| 8.0 | 9.16 | 0.00 |
| 9.0 | 10.30 | 0.00 |
| 10.0 | 11.43 | 0.00 |
| 11.0 | 11.89 | 0.00 |
| 12.0 | 12.10 | 3.82 |
| 13.0 | 12.10 | 6.60 |
| 14.0 | 12.10 | 8.67 |
| 15.0 | 12.10 | 10.45 |
| 16.0 | 12.10 | 12.05 |
| 17.0 | 12.10 | 13.54 |
| 18.0 | 12.10 | 14.92 |
| 19.0 | 12.10 | 16.23 |
| 20.0 | 12.10 | 17.47 |
| 21.0 | 12.10 | 18.70 |
| 22.0 | 12.10 | 19.94 |
| 23.0 | 12.10 | 21.18 |
| 24.0 | 12.10 | 22.35 |
| 25.0 - Cut-Out | 12.10 | 23.47 |

The turbines are placed on the OC4 semi-submersible platform, described above, with their bases elevated at a 10 meters height above mean sea level. Therefore, keeping the same hub height elevation, the turbine tower height for SS platforms needs to be adjusted to 77.6 m, taking into consideration all of its structural properties. In addition to that, the tower base diameter needs to be adjusted from 6 m to 6.5 m to match the size of the main column of the platform. In the SS platform floating case, the turbine has the tower base thickness equal to 0.027 m. The top diameter of the turbine is equal to 3.87 m with a thickness of 0.019 m [88]. A summary of the platform-adjusted 5 MW NREL turbine properties is presented in Table 3.5 [88].

**Table 3.5:** Semi-submersible platform-adjusted NREL 5 MW wind turbine structural specifications [88].

| Property | Value | Unit |
|---|---|---|
| Elevation to tower base (platform top) above SWL | 10 | m |
| Elevation to tower top (yaw bearing) above SWL | 87.6 | m |
| Turbine tower height | 77.6 | m |
| Overall (integrated) tower mass | 249,718 | kg |
| CM location of tower above MSL along tower centerline | 43.4 | m |
| Tower base diameter | 6.5 | m |
| Tower base thickness | 0.027 | m |
| Top of the tower diameter | 3.87 | m |
| Top of the tower thickness | 0.019 | m |

## 3.3 Wind farm location

The wind farm location selected for the analysis is near the port of Leixões (Atlantic Ocean). The Leixões port is one of Portugal's main ports, located in the north-western regions of the country, in close proximity to the city of Porto [90]. It is situated at the coordinates 41°10'27"N 9°03'50"W. The wind farm will be situated at about 35 km distance from the shore and the port. The mean water depth at the location is about 145 m [91]. The wind farm location in reference to the onshore substation location (Leixões) is presented in Figure 3.2 [91].

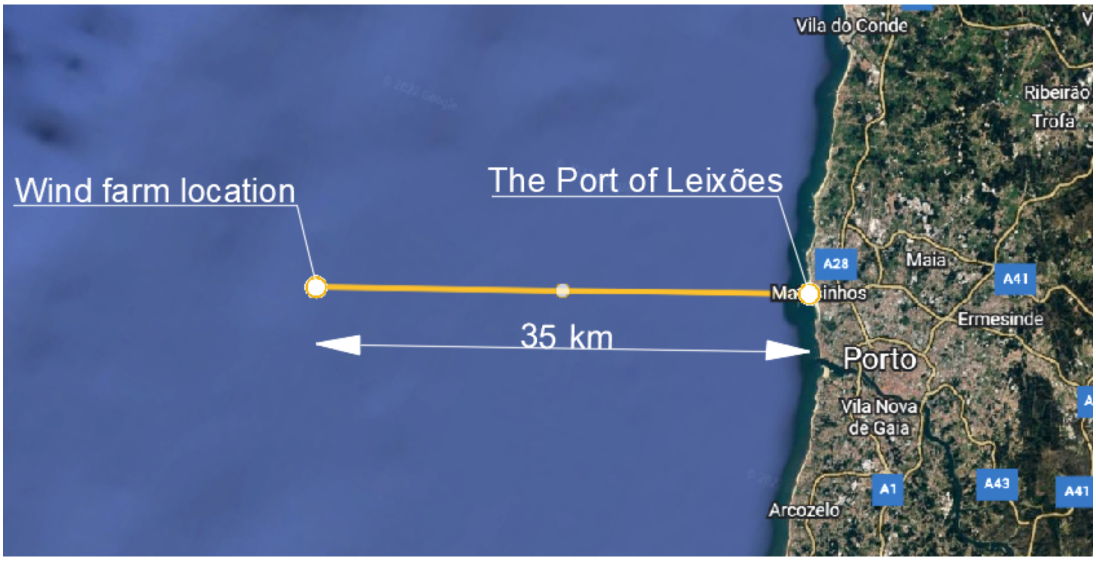

**Figure 3.2:** Wind farm and the onshore substation location with its distance from the shore [91].

## 3.4 Wind and wave resource characterization

The characteristic wind-wave climate in the location was estimated based on wind and wave data from the years 1979-2009 taken from the National Oceanic and Atmospheric Administration (NOAA) [92] and reported in [93]. The data were aggregated to represent the wind speed probability of occurrence $\xi_u$, significant wave height $H_s$, and peak wave period $T_p$ for each wind class. The wind data was represented at 10 m elevation above the mean sea level (MSL) and had to be recalculated to match the wind speed at the hub height using Equation 3.1 [94].

$$V(z) = V_{\mathrm{Ref}} \left( \frac{z}{z_{\mathrm{Ref}}} \right)^{\alpha_{\mathrm{roughness}}}, \tag{3.1}$$

where $V(z)$ is the wind speed at the $z$ elevation above the sea level; $V_{\mathrm{Ref}}$ is the reference wind velocity at $z_{\mathrm{Ref}}$ elevation, and $\alpha_{\mathrm{roughness}}$ is the surface roughness coefficient assumed to be equal to 0.12 [95]. Data obtained from the above mentioned calculations is presented in Table 3.6.

**Table 3.6:** Characteristic wave-wind climate in the northwest coast of Portugal. For each wind speed class, $u$, is presented the associated sea state conditions in terms of significant wave height, $H_s$, and peak period, $T_p$. The probability of occurrence of each wind class, $\xi_u$, is also presented. Data for $H_s$ and $T_p$ represent 5% trimmed mean values.

| $u$ (m/s) | $H_s$ (m) | $T_p$ (s) | $\xi_u$ (%) |
|---|---|---|---|
| 1 | 1.66 | 11.37 | 1.76 |
| 2 | 1.67 | 11.34 | 3.19 |
| 3 | 1.68 | 11.32 | 4.88 |
| 4 | 1.69 | 11.27 | 6.60 |
| 5 | 1.76 | 11.30 | 7.93 |
| 6 | 1.80 | 11.22 | 8.87 |
| 7 | 1.88 | 11.26 | 9.25 |
| 8 | 1.98 | 11.21 | 8.89 |
| 9 | 2.11 | 11.24 | 8.14 |
| 10 | 2.23 | 11.16 | 7.57 |
| 11 | 2.34 | 11.04 | 6.88 |
| 12 | 2.49 | 10.94 | 6.11 |
| 13 | 2.64 | 10.90 | 5.01 |
| 14 | 2.87 | 10.92 | 4.04 |
| 15 | 3.06 | 10.86 | 3.17 |
| 16 | 3.34 | 11.02 | 2.39 |
| 17 | 3.56 | 11.11 | 1.75 |
| 18 | 3.81 | 11.20 | 1.25 |
| 19 | 4.01 | 11.36 | 0.83 |
| 20 | 4.39 | 11.46 | 0.54 |
| 21 | 4.71 | 11.68 | 0.37 |
| 22 | 4.89 | 11.79 | 0.22 |
| 23 | 5.32 | 11.95 | 0.14 |
| 24 | 5.43 | 12.00 | 0.10 |
| 25 | 5.64 | 11.88 | 0.04 |

In order to verify the wind speed probability of occurrence $\xi_u$, a Weibull distribution function was calculated using the methodology reported in [96]. The Weibull distribution equation is calculated as follows [96],

$$f_{\mathrm{Weibull}}(v) = \left( \frac{k_{\mathrm{Weibull}}}{c_{\mathrm{Weibull}}} \right) \left( \frac{v}{c_{\mathrm{Weibull}}} \right)^{k_{\mathrm{Weibull}}-1} exp \left[ - \left( \frac{v}{c_{\mathrm{Weibull}}} \right)^{k_{\mathrm{Weibull}}} \right], \tag{3.2}$$

where $f_{\mathrm{Weibull}}(v)$ is the Weibull probability for specific wind class; $k_{\mathrm{Weibull}}$ is the function shape parameter, determined by Equation 3.3 and $c_{\text{Weibull}}$ is the function scale parameter, determined by Equation 3.4 [96].

$$k_{\text{Weibull}} = \left(\frac{\sigma_v}{V_{\text{avg}}}\right)^{-1.086}, \tag{3.3}$$

$$c_{\text{Weibull}} = V_{\text{avg}} \left(0.568 + \frac{0.433}{k_{\text{Weibull}}}\right)^{-\frac{1}{k_{\text{Weibull}}}}, \tag{3.4}$$

where $\sigma_v$ is the standard deviation of wind data and $V_{\text{avg}}$ is the mean wind speed. Based on the method explained above, the Weibull shape parameter $k_{\text{Weibull}}$=2.16 and the Weibull scale parameter $c_{\text{Weibull}}$=9.96 was determined. Figure 3.3 shows the calculated probability of specific wind classes for the chosen location along with the Weibull distribution function.

The predominant wind direction in the selected location is NW, which occurs over 40% of the time [97].

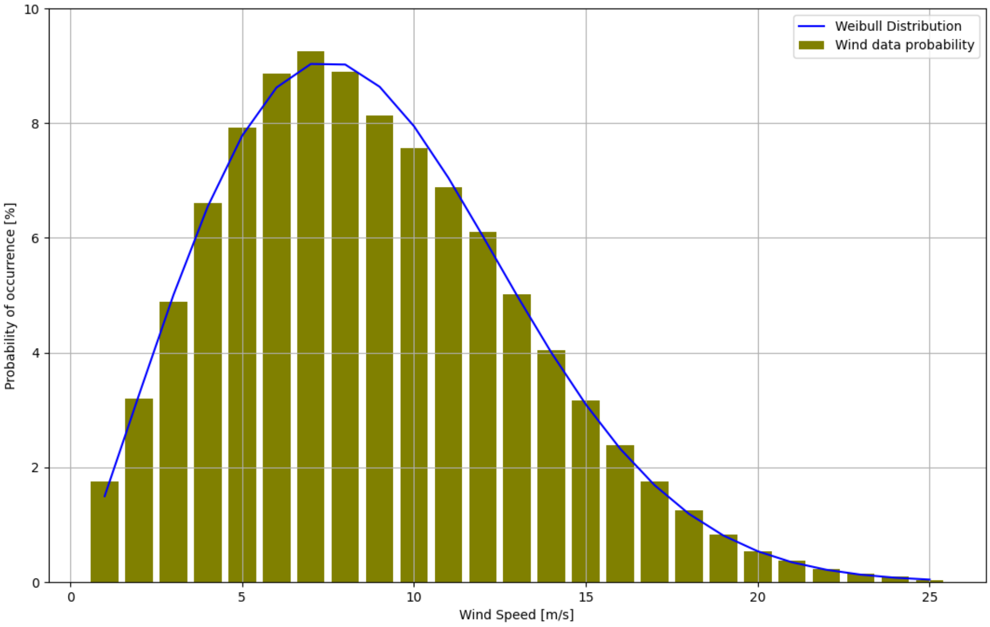

**Figure 3.3:** Chosen location's wind speed probability distribution with a fitted Weibull distribution function.

## 3.5 Wind farm layout

The orientation of the wind farm to the North-West was chosen, due to the north-westerly wind being the predominant direction in the selected location. Figure 3.4 shows the proposed layout of the analysis' reference case wind farm (base case). It consists of twenty turbines of 5 MW each distributed in five rows, each having four wind turbines. However, due to computational and time limitations, only one row of the presented farm is going to be used in the simulations. The spacing of consecutive turbines in a row is set to 4.3D and the spacing between each row is set to $y_D$, which is measured in turbine diameter D multiples. The spacing is based on the Lillgrund wind farm, reported in [98], for which the row spacing was chosen to be 3.3D. A very tight layout like this can lower the costs of array cables, land lease, and site clearance. However, the close proximity of the turbines may highly increase farm losses due to the wake on consecutive turbines [98]. The main specifications of the proposed wind farm are presented in Table 3.7.

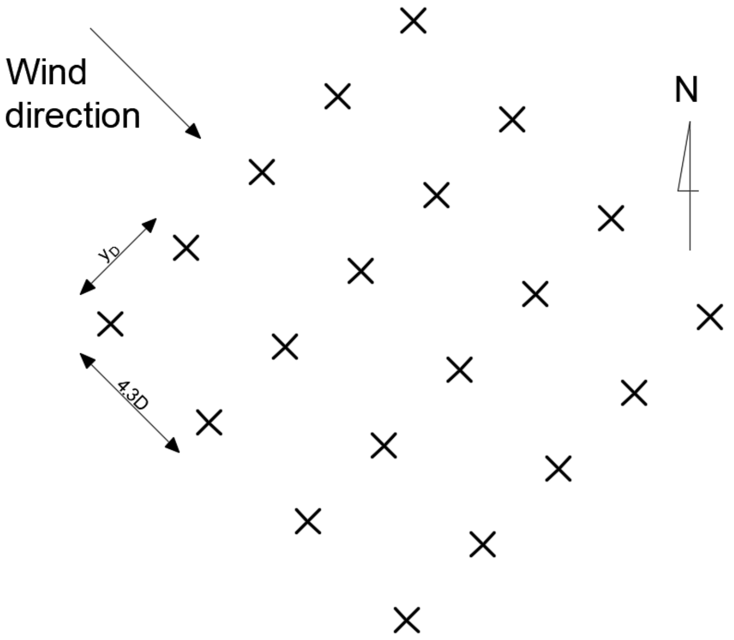

**Figure 3.4:** Proposed layout of the base case wind farm, where D is the turbine rotor diameter (D=126 m) and $y_D$ is the distance between rows measured in multiples of rotor diameter D.

**Table 3.7:** Reference case wind farm specifications.

| Property | Value | Unit |
|---|---|---|
| Number of turbines | 20 | - |
| Total wind farm power | 100 | MW |
| Distance from the farm to the onshore substation | 35 | km |
| Water depth | 145 | m |
| Turbine spacing | 4.3D | m |
| Row spacing | 3.3D | m |

The transmission system of the farm is assumed to comprise an onshore substation (SB), an offshore substation, a high-voltage export cable that connects the onshore SB and the offshore substation, medium-voltage (33kV) array cables, namely terminal cables, connecting each row of turbines, and inter-array cables, connecting each turbine within the row. The onshore substation is connected to the electrical grid by a high-voltage onshore cable [99]. A schematic diagram showing an example of the proposed transmission system layout is presented in Figure 3.5.

**Figure 3.5:** A schematic diagram showing transmission system layout used in the wind farms simulated in this thesis. Prepared based on [99].

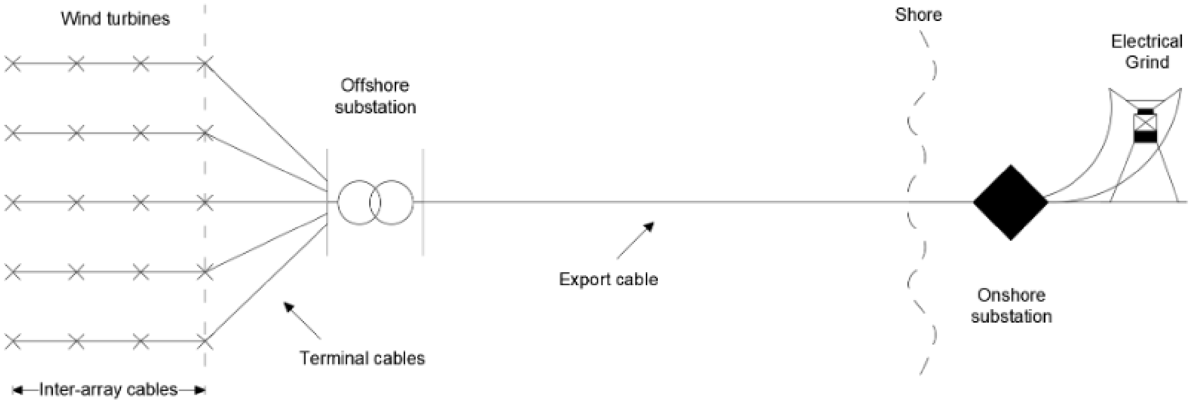

## Chapter 4

# Techno-economic assessment methodology

This Chapter presents the simulations' approach and describes the methodology of the farm annual electricity production, farm's energy losses due to wake effects, and capacity factor calculations. It also presents a cost modeling approach used to calculate the levelised cost of energy in this thesis. Finally, it defines an energy yield density factor, that presents the annual electricity production of the farm in relation to its total area. The methodology of simulations and energy performance calculations is presented in Figure 4.1. Additionally, the cost modeling and LCOE calculation approach is presented in Figure 4.2.

The energy performance calculation starts with the case study definition and FAST.Farm simulations setup, which includes the turbulent wind generation, farm layout setup, resolution domains, wake settings, initial conditions, and wave data setup. After conducting all of the simulations, power generation data for every turbine is averaged in the total simulation time, using Python and acquired for every wind speed case. Then, using the obtained data, the annual electricity production, farm energy losses due to wake effects, capacity factor, and energy yield density factors are calculated in order to evaluate the farms' performance and compare different selected case studies.

The cost modeling approach starts with the case study definition as well. Then, all of the wind farm costs, including the planning phase capital expenditures (CAPEX), material CAPEX, and installation CAPEX are calculated. Then, the operational expenditures (OPEX), comprising the maintenance and operational costs are calculated. Finally the decommissioning expenditures (DECEX), including the dismantling costs of wind farm's components, are calculated. Based on the aforementioned expenditures' values, and the annual electricity production values for a specific wind farm, the levelized cost of energy is calculated after discounting the total cost of the wind farm and the annual electricity production values in the total farm's lifetime, which is set to 25 years.

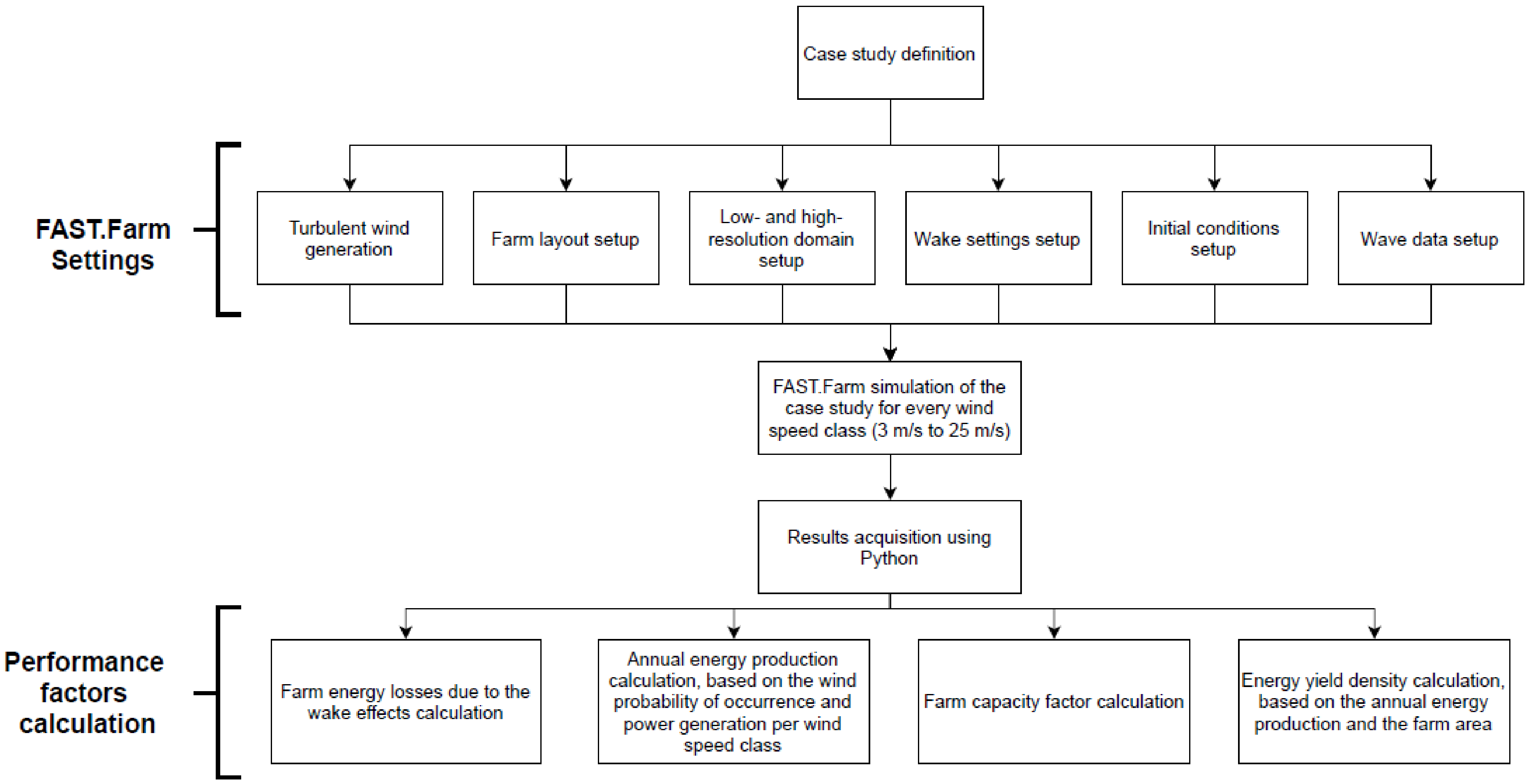

**Figure 4.1:** Simulation and energy performance calculation methodology diagram.

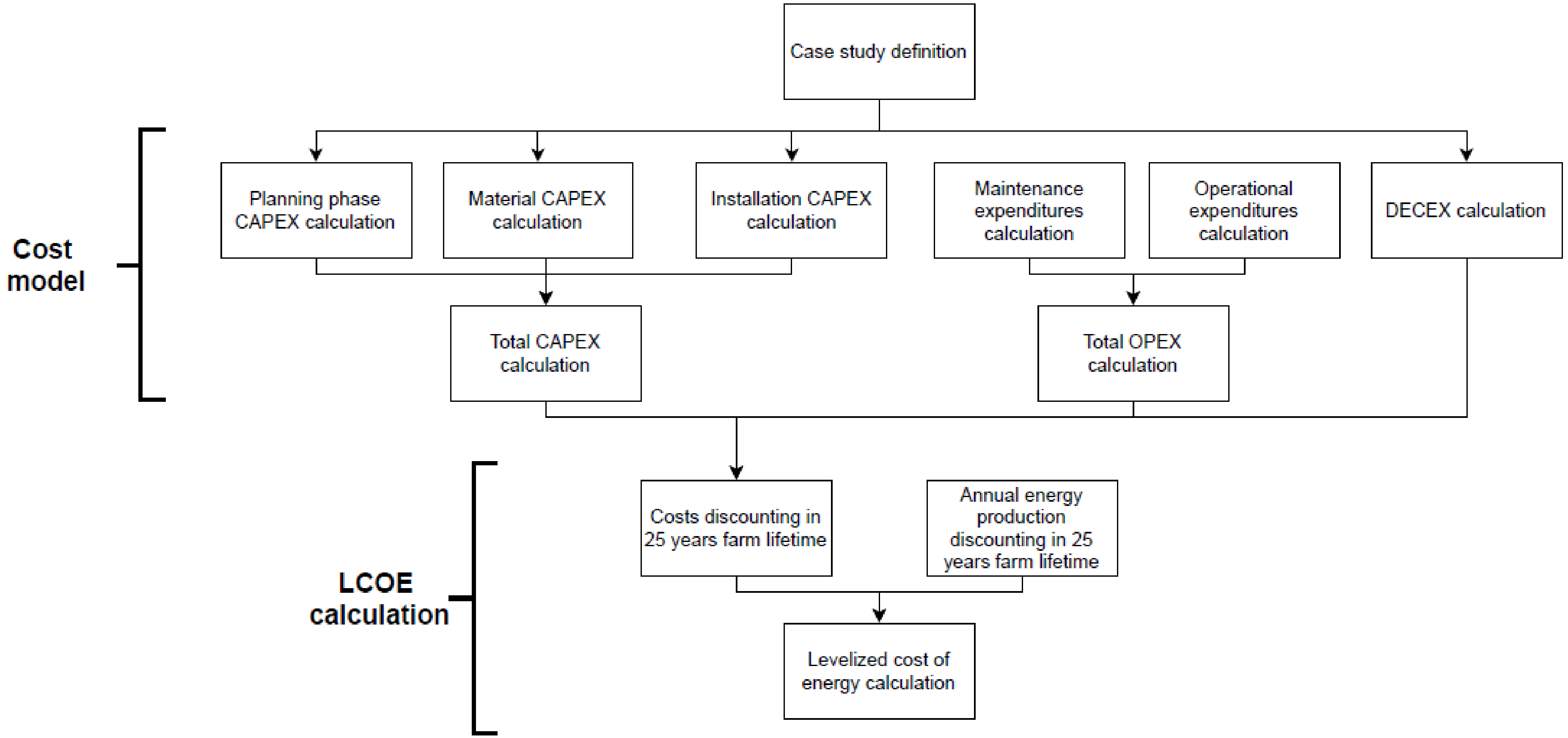

**Figure 4.2:** Cost model and LCOE calculation methodology diagram.

## 4.1 FAST.Farm simulation description

In order to estimate the power generation of the farm and the platform motions, simulations in NREL's FAST.Farm v3.1.0 software were conducted for every wind speed class, ranging from 3 m/s to 25 m/s in each of the analyzed cases. Because of the need for high computational power and very long duration of each of the simulations, one row of the wind farm was simulated. The total simulated time was chosen to be equal to 4200 s with the simulation timestep equal to 0.1 s.

Wind field data was obtained by using TurbSim v2.00.07 software. For each considered wind speed .bts files containing turbulent wind data were generated. The timestep of wind interpolation was equal to 0.1 s and the grid size of wind flow was equal to $y$ = 1000 m and $z$ = 340 m. The spectral wind model used in wind generation is the Kaimal model described in IEC 61400-1 [100]. The turbulence type used was the normal turbulence model, category ”B”, in accordance with the IEC standard [100]. The velocity spectra for this turbulence model and the category are also presented in the TurbSim user guide [101]. The wind profile type used was the power law model, described in [101], with the power law exponent equal to 0.12 [95].

### 4.1.1 Turbine and wind data interpolation domains placement

In FAST.Farm it is possible to specify the details for different wind data interpolation domains - low-resolution (LR) and high-resolution (HR) domains, which are described in section 2.10.3. For both of them, it is necessary to set the time step for wind data interpolation, the size of the grid, and the number along with the distance between spatial nodes of the grid. The size of the LR domain was equal to $x$ = 5000 m, $y$ = 1000 m, $z$ = 340 m and the size of the HR domains was equal to $x$ = 150 m, $y$ = 150 m, $z$ = 170 m. Other specifications of the domains are presented in Table 4.1. Wind turbines' placement with distances and LR, and HR domains are presented in Figure 4.3. The first turbine is placed 378 m after the start of the domain in the $x$-direction in order to make sure that the inflow wind at its rotor is fully developed and the aerodynamic induction is properly simulated, as recommended in [21]. LR domain span after the last turbine is equal to around 3000 m in order to allow the wake enough distance downwind of the last turbine for its propagation.

**Table 4.1:** Specification of the low-resolution and high-resolution domains in the simulated cases. LR stands for low-resolution, and HR stands for high-resolution.

| Specification | Value | Unit |
|---|---|---|
| LR domain data interpolation time step | 2.0 | s |
| HR domain data interpolation time step | 0.1 | s |
| LR domain nodes spacing | 10 | m |
| HR domain nodes spacing | 5 | m |
| LR domain X-direction nodes # | 501 | - |
| LR domain Y-direction nodes # | 101 | - |
| LR domain Z-direction nodes # | 35 | - |
| HR domain X-direction nodes # | 31 | - |
| HR domain Y-direction nodes # | 31 | - |
| HR domain Z-direction nodes # | 35 | - |

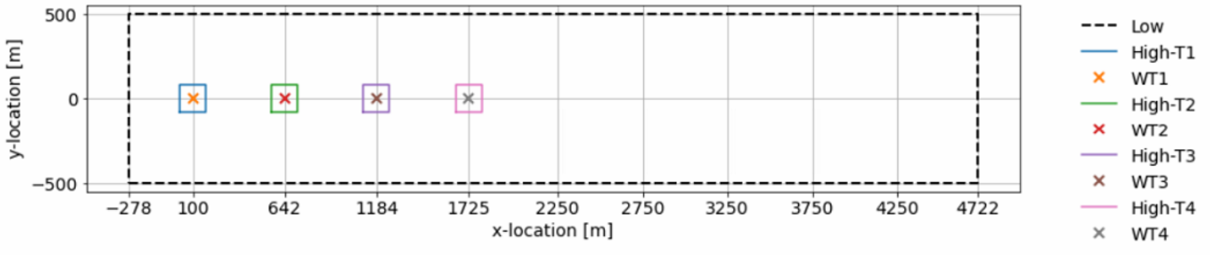

**Figure 4.3:** Initial FAST.Farm turbine layout with low and high resolution domains defined. ”WT” stands for wind turbine; ”Low” stands for the low resolution domain boundary; and High-TX stands for high resolution domain for turbine X.

### 4.1.2 Simulation settings and results

The hydrodynamics module in the simulations uses a JONSWAP/Pierson-Moskowitz spectrum to create the incident wave time series. For more information on the spectral models used in the program, see [102, 103]. Wave data was taken from Table 3.6. The model used for wake turbulence simulation was based on Blade Element Momentum Theory (BEMT), described in section 2.8. All of the wake meandering, wake diameter calculation, wake deflection correction, near-wake correction, shear layer, and eddy viscosity filter function parameters were set to default FAST.Farm settings, as during the software development, they were specified for the 5 MW NREL turbine, which is used in the simulations.

The results of the simulations for each of the turbines are generated in an output text file with all of the variable values for the selected output time step (0.1 s) and total simulation time (4200 s). The main output variables chosen are generated power; generator torque; platform surge, sway, heave, roll, pitch, and yaw motions; and forces acting on the turbine and the tower base. For each simulation, the last 3600 s of the simulations are considered, as the first 600 s are set for the development of the wind and wake profiles to the last of the turbines as well as to minimize the impact of initial numerical errors.

## 4.2 Energy and wake losses calculation

The averaged generated power simulation results were matched with the individual wind speeds and probabilities of their occurrence to calculate the Annual Electricity Production (AEP) for each of the turbines analyzed and consequently, for the whole wind farm. Equation 4.1 is used to calculate the $AEP_{\mathrm{Uw}}$ for each of the wind speed classes.

$$AEP_{\mathrm{Uw}} = \frac{P_{\mathrm{Uw}}\xi_w \cdot 8760}{1000}, \tag{4.1}$$

where $AEP_{\mathrm{Uw}}$ is the annual electricity production for a specific wind speed, represented in MWh, and $P_{\mathrm{Uw}}$ is the power generated on the wind turbine for a specific wind speed, represented in kW. The $AEP_{\mathrm{Uw}}$ values obtained for the analyzed turbines were summed up for all of the wind speeds, ranging from 3 m/s to 25 m/s and the total annual electricity generated for each turbine $AEP_{\mathrm{WT}}$ was obtained. The $AEP_{\mathrm{WT}}$ values are represented in GWh.

Afterwards, the total gross wind farm AEP needs to be calculated. Therefore, the $AEP_{\text{WT}}$ results for all of the turbines in a row are summed and then multiplied by the number of rows in the wind farm. It is presented in Equation 4.2,

$$AEP_{\text{farm.gross}} = \left( \sum_{i=1}^{4} AEP_{\text{WT}} \right) n_{\text{ rows}}, \tag{4.2}$$

where $AEP_{\text{farm.gross}}$ is the gross annual electricity production of the wind farm, represented in GWh and $n_{\text{ rows}}$ is the number of turbine rows in the farm.

In order to obtain the energy losses due to wakes, a reference AEP for an ideal farm needs to be calculated. As the first turbine in a row is not affected by the wake in the simulations, it is assumed that for the ideal farm, each of the turbines is generating the same amount of energy as WT1. In Equation 4.3, the $AEP_{\text{WT1}}$ calculated for the first wind turbine (WT1) is multiplied by the total number of turbines in the analyzed wind farm $n_{\text{T}} = 20$ to obtain the $AEP_{\text{ideal}}$ which is the annual electricity production for a wind farm operating without wake losses. When it comes to the tower hub height variation cases, the $AEP_{\text{ideal}}$ is calculated by taking both of the turbine hub heights as if they were unaffected by the wake losses and multiplying them by ten (standing for the number of turbines of the specific hub height).

$$AEP_{\text{ideal}} = AEP_{\text{WT}} \cdot n_{\text{T}}. \tag{4.3}$$

Calculations of the wake effect losses will help with the evaluation of wind farm cases' performance, considered in this work. The losses associated with the wake effects were calculated from Equation 4.4, as follows,

$$\Delta AEP_{\text{wake}} = \frac{AEP_{\text{ideal}} - AEP_{\text{farm.gross}}}{AEP_{\text{ideal}}} \cdot 100\%, \tag{4.4}$$

where $\Delta AEP_{\text{wake}}$ represents the wake losses on the annual electricity production of the wind farm.

Furthermore, to obtain the net annual electricity farm production $AEP_{\text{farm,net}}$, turbines annual availability equal to 95% [104]; transmission system losses $\Delta AEP_{\text{transmission}}$ equal to 3% [105]; and airfoil damage losses $\Delta AEP_{\text{airfoil}}$ equal to 2% [106] were also included. Equation 4.5 represents the calculation methodology,

$$AEP_{\text{farm,net}} = AEP_{\text{farm.gross}} (\Delta AEP_{\text{availability}} - \Delta AEP_{\text{airfoil}} - \Delta AEP_{\text{transmission}}). \tag{4.5}$$

## 4.3 Wind farm costs and LCOE calculation

One of the indicators to evaluate and compare the techno-economic feasibility of energy-related projects is the levelized cost of energy and it is considered a key indicator in this work. It is calculated using Equation 2.1, where an estimation of CAPEX, OPEX and DECEX are needed. In this study, an economic model evaluating all these costs was prepared, mostly based on references [44, 107]. Material CAPEX consists of the project development, construction insurance, and contingency costs of the farm; the turbine, SS platforms, transmission system, and mooring and anchoring material costs; and the installation

CAPEX, of the aforementioned components. OPEX are divided into the operating and maintenance (O&M) costs. DECEX costs involve the site clearance and wind farm components dismantling. The main input variables considered in the cost model with their references are presented in Table 4.2

**Table 4.2:** Input variables values considered in the wind farm cost model with their corresponding references.

| Input name | Value | Unit | Reference |
|---|---|---|---|
| Cost of steel | 2200 | €/ton | [50, 108] |
| Hourly cost of labor | 42 | €/h | [109] |
| Technicians' daily stake | 200 | €/day | [44] |
| MV array cables price | 279 | €/m | [44] |
| HV offshore export cables price | 336 | €/m | [44] |
| HV onshore export cables price | 83 | €/m | [44] |
| Daily rate of rock-dumping vessel | 156,000 | €/day | [107] |
| Cable scour protection speed | 600 | m/day | [107] |
| Mooring cables mass | 113.35 | kg/m | [88] |
| Mooring cables length | 835.5 | m | [88] |
| Mooring lines cost | 5.07 | €/kg | [44] |
| Hourly rate of port crane | 883 | €/h | [44] |
| Daily cost of port storage surface | 0.35 | €/($m^2$days) | [110] |
| Daily rate of tug vessel | 22,500 | €/day | [44] |
| Tug vessel mobilization cost | 37,000 | € | [44, 107] |
| Daily rate of MV array cable laying vessel | 91,000 | €/day | [44] |
| Cable laying vessel speed | 20 | km/h | [107] |
| Cable laying vessel mobilization costs | 572,000 | € | [107] |
| MV array cable laying vessel installation rate | 150 | m/day | [107] |
| Daily rate of the export cable laying vessel | 114,000 | €/day | [44] |
| Export cable laying vessel installation rate | 348 | m/day | [107] |
| Onshore cables installation cost | 194.50 | €/m | [44, 111] |
| Daily rate of anchor handling vehicle | 78,000 | €/day | [107] |
| Daily rate of jack-up vessel | 216,000 | €/day | [107] |
| Jack-up vessel speed | 26 | km/h | [107] |
| Daily rate of crew transfer vessel | 36,000 | €/day | [107] |
| Crew transfer vessel speed | 37 | km/h | [107] |
| Weather downtime factor | 1.25 | - | [107] |

### 4.3.1 Material CAPEX evaluation

The CAPEX components in the project preparation phase include the contingency, project development (engineering), and construction insurance costs. Based on [47], it is estimated that the contingency, project development, and construction insurance costs' shares amount to 5.5%, 1.1%, and 0.7% respectively in relation to the total wind farm costs. Therefore, these values are used to assess the aforementioned costs in the CAPEX model in this work.

Based on Maienza et. al. (2020) [44], the turbine cost is a function of the wind farm's nominal power and is represented by [44]

$$C_{\mathrm{T}} = (1.6P_{\mathrm{t,nom}} - 1.9) \cdot n_{\mathrm{T}} \tag{4.6}$$

where $C_{\mathrm{T}}$ is the total cost of the turbines and $P_{\mathrm{t,nom}}$ is the nominal turbine power.

Semi-submersible platform material costs comprise the structural steel cost, calculated by taking the structural platform mass and multiplying it by the price of manufactured steel; and direct labor cost based on the hourly rate of labor and total manufacturing time of the platforms [44].

The transmission system costs consist of the medium voltage array cables, high voltage export cables, and onshore export cables costs, calculated by multiplying the unit cost of the individual cables by their distances; the offshore substation costs comprised of the transformers, switchgear and foundation costs; the onshore substation; the supervisory control and data acquisition (SCADA) system; and grid connection costs [44, 107]. The onshore substation cost is estimated as half of the offshore substation expenditures [44, 107]. SCADA system cost has been calculated as the function of the turbines' number [107] and the grid connection total expenditures are assumed to be equal to 2 M€ [107]. In addition to the above, array cables' scour protection costs are considered. They are calculated on account of the daily rate of the rock-dumping vessel and the time in days needed to lay down rocks on the scour protection layer [107].

The last part of the material CAPEX calculations is the mooring and anchoring expenditures. Mooring lines' cost is calculated by taking the unit mass of the lines, their length, the unit price of the cables, and the total number of mooring lines and multiplying them. The number of mooring lines is calculated by taking the total number of turbines in the farm and multiplying them by three. As the offshore substation is assumed to be floating as well, additional four mooring lines are added. Anchoring costs are calculated by taking the unit costs of the anchors and multiplying them by the number of anchors, which is equal to the number of the mooring lines [44, 88, 107].

### 4.3.2 Installation CAPEX

Installation CAPEX consist of the turbine installation; floating platform installation, including the port-to-location transportation; transmission system installation, comprised of the cable laying and the substations' installation; and the mooring and anchoring installation costs.

As in the case of the SS platform, the wind turbines are installed onshore, there are no transport or construction vessels needed for the turbines' installation. The only costs associated with the installation of the turbines are port storage, and onshore turbine mounting on the platforms using a port crane that can be calculated with regards to the port storage surface unit cost, dimensions of the stored turbines, and port crane hourly costs [44].

Floating platform installation requires tugboats to transport the already assembled platforms to the wind farm site. SS platforms do not require any mounting offshore, as they are manufactured and assembled onshore. Therefore, the costs associated with the platforms' installation consist only of the port procedure costs, which require the port crane to launch the platforms into the ocean, calculated in the same manner as the turbine port crane mounting; and the transportation costs which are calculated with regard to the daily rate of tugboats and the time needed to transport all of the platforms [44, 107].

Transmission system installation costs take into consideration the offshore and onshore cables and the offshore and onshore substations' installation. Offshore cables installation is done by cable laying vessels (CLV). The total costs of cable laying depend on the daily rate of CLVs, the length of the cables, and the cable installation speed of the CLVs for specific cable types. The offshore substation is assumed to be floating, so its installation requires the usage of tugboats. Therefore, the costs associated with it consist of the daily rate of the tugboat multiplied by the total installation time, and additionally, of the offshore substation components port storage [107].

Installation of the mooring and anchoring system is done with the help of an anchor handling vehicle (AHV). Therefore, its costs are based on the daily rate of the AHV and the total installation time needed [107]. All of the installation costs that required the usage of different vessels were multiplied by a selected weather-dependent downtime factor, that simulates the inability of offshore installation actions due to bad weather conditions [107].

### 4.3.3 OPEX calculation methodology

The values obtained during the OPEX analysis consist of the annual operating and maintenance costs. The operating expenses include onshore wind farm management $C_{\text{Mgmt}}$; marine operations management $C_{\text{Mgmt,marine}}$; weather $C_{\text{Weather}}$, condition monitoring $C_{\text{Condition}}$; operating facilities yearly costs $C_{\text{Facilities}}$; health, safety ad environment (HSE) monitoring $C_{\text{HSE}}$; farm insurance $C_{\text{Insurance}}$; and landlease $C_{\text{Landlease}}$. The above mentioned values can be calculated according to [107] using equations shown in Equation 4.7. All of the calculated values are presented in M€/year.

$$\begin{aligned}
C_{\text{Mgmt}} &= 0.000832 \cdot P_{\text{WF}}, \\
C_{\text{Mgmt,marine}} &= 0.00125 \cdot P_{\text{WF}}, \\
C_{\text{Weather}} &= 0.000104 \cdot P_{\text{WF}}, \\
C_{\text{Condition}} &= 0.000832 \cdot P_{\text{WF}}, \\
C_{\text{Facilities}} &= 0.00135 \cdot P_{\text{WF}}, \\
C_{\text{HSE}} &= 0.000520 \cdot P_{\text{WF}}, \\
C_{\text{Insurance}} &= 0.0218 \cdot P_{\text{WF}}, \\
C_{\text{Landlease}} &= 0.005 \cdot P_{\text{WF}},
\end{aligned} \tag{4.7}$$

where $P_{WF}$ is the total nominal power of the wind farm.

OPEX related to maintenance and repair consist of the manual turbine controller reboot cost, minor turbine repair, medium turbine repair, major turbine repair, major replacement, minor foundation repair, minor substation repair, major substation repair, and cable repair. Factors affecting the maintenance costs are the repair time, failure occurrence rate, number of technicians needed, or the vessel used. All of the factors are shown in Table 4.3 [107].

Additionally, these costs also include material expenses, which are shown in Table 4.4. The total annual maintenance costs are calculated in two steps. The first step is to calculate the total time (days) of annual maintenance for a specific category, using the annual failure rate and unit repair time, multiplied by the number of components, namely turbines, platforms, and the substation; and the total transportation time of the vessel used [107]. Then, taking the daily rates of specific vessels and the technicians' daily

**Table 4.3:** Repair time, failure rate, technicians and vessels needed in case of specific wind farm maintenance works. CTV stands for crew transfer vessel; and CLV represents the cable laying vessel [107].

| Description | Repair time (h) | Failure rate (times/year) | Technicians | Vessel |
|---|---|---|---|---|
| Manual turbine controller reboot | 3 | 7.5 | 3 | CTV |
| Minor repair turbine | 7.5 | 3 | 3 | CTV |
| Medium repair turbine | 22 | 0.275 | 3 | CTV |
| Major repair turbine | 26 | 0.04 | 4 | Tugboat |
| Major replacement turbine | 52 | 0.08 | 5 | Tugboat |
| Minor foundation repair | 8 | 0.023 | 3 | CTV |
| Minor substation repair | 8 | 0.45 | 3 | CTV |
| Major substation repair | 48 | 0.05 | 4 | CTV |
| Cable repair | 32 | 0.0004 | 0 | CLV |

rates, the total repair cost is calculated. Moreover, the total repair material cost is calculated using the values presented in Table 4.4 [107].

**Table 4.4:** Material and repair costs of different maintenance works [107].

| Description | Material cost (% of turbine investment) | Cost (M€) |
|---|---|---|
| Manual turbine controller reboot | 0.004 | |
| Minor repair turbine | 0.09 | |
| Medium repair turbine | 0.3 | |
| Major repair turbine | 0.5 | |
| Major replacement turbine | 7.55 | |
| Minor foundation repair | | 0.0052 |
| Minor substation repair | | 0.0052 |
| Major substation repair | | 0.26 |
| Cable repair | | 0.36 |

Similarly to the installation CAPEX calculation methodology, the weather-dependent downtime factor was used in the vessel transportation and repair time calculations [107].

### 4.3.4 DECEX calculation methodology

The decommissioning expenditures (DECEX) were calculated with specific assumptions derived from Maienza et. al. (2020) [44]. It was assumed that the dismantling costs of the platforms, the cables, the substations, and the mooring and anchoring system are equal to 70%, 10%, 90%, and 90% of their total installation costs respectively [44].

## 4.4 Wind farm evaluation factors

Apart from the LCOE, other indicators can be used to evaluate the wind farm case studies. Annual energy losses due to the wake effects $\Delta AEP_{\text{wake}}$ were calculated based on Equation 4.4 for each of the simulation cases along with the annual wind farm electricity production $AEP_{\text{farm, net}}$ can be used to compare the cases in terms of their overall performance.

Another indicator that can be used to determine wind farms' performance is the capacity factor (CF).

It is calculated as a percentage, by taking the AEP of the analyzed wind farm and dividing it by the theoretical maximal energy yield from each farm. It shows how well the wind farm utilizes the available wind resources [112]. It is represented by

$$CF = \frac{1000 \cdot AEP_{\mathrm{farm,net}}}{P_{\mathrm{T}} n_{\mathrm{T}} \cdot 8760} \cdot 100\% \tag{4.8}$$

where $CF$ is the farm capacity factor; 8760 is the number of hours in a year and division by 1000 is used for units consistency.

The above-mentioned factors can showcase the profitability and performance of the wind farm, but may not be enough to properly evaluate different simulation cases. For example, increasing the spacing distance between the subsequent turbines in a wind farm may decrease the wake losses, therefore increasing the wind farm energy yield, but it also can increase the material and installation expenditures of the whole project, which influence the LCOE [98]. Additionally, a bigger area of the farm may increase the costs associated, for example, with maintenance, and licensing. For this reason, an energy yield density factor is defined here as the total annual electricity generated on the wind farm in relation to its area. It is calculated as

$$EYD = \frac{AEP_{\mathrm{farm,net}}}{A_{\mathrm{OWF}}}, \tag{4.9}$$

where $EYD$ is the energy yield density presented in (GWh/(year·km$^2$)) and $A_{\mathrm{OWF}}$ is the total wind farm area in km$^2$.

# Chapter 5

# Results and discussion

This Chapter describes different case studies and presents the results obtained from the simulations. A comparison of the annual electricity production, levelized cost of energy, energy wake losses, capacity factor, and energy yield density values for all case studies is presented and discussed here.

## 5.1 Simulation cases description

In this work, 25 different simulation cases were studied and grouped into four sets. Each case study comprises power generation simulation in FAST.Farm, cost modeling, and calculation of the annual electricity production, levelized cost of energy, capacity factor, wind farm energy wake losses due to wake effects, and energy yield density. Simulations for each studied case were done for 23 different wind speeds (from the turbine cut-in 3 m/s to the turbine cut-out 25 m/s wind speed), resulting in more than 575 simulations performed in this thesis.

The first set was done with the objective of studying the farm performance with respect to different turbine spacings in a wind farm row. The spacings selected were equal to 3D, 4.3D (base case), 6D, 8D, 10D, 12D, 14D, 16D, and 18D, with D being the rotor diameter. The second set of simulations had the same wind farm layout as the base case, with the objective of turbine hub heights' differentiation. Wind farms having all of the turbines (ALLTRB) hub heights at 78 m, 90 m (base case), 102 m and 109 m were simulated. Additionally, four more cases with WT1 and WT3 having a different hub height from the WT2 and WT4 turbines; and one case with WT1 and WT4 having a different hub height compared to WT2 and WT3 were prepared. The third set of cases considered different layouts of the wind farm. Two layouts: a diamond-shaped and a dephased-shaped with different dephasing values measured in rotor radius R multiples were considered. The diamond-2R layout is presented in Figure 5.1 and a dephased layout with 2R dephasing is presented in Figure 5.2. The diagrams represent the simulations cases, which include only one wind farm row. In the diamond-shaped layout, due to placing two turbines in the same $x$ location, the low-resolution domain in the $x$-direction was shortened in order to match the same distance left after the last turbine as in the base case. In the LCOE calculations for the whole wind farm, the row spacing was assumed to be equal to 3.3D between the outermost turbines of each row (WT2 in one and WT3 in the next row) in orthogonal $y$-direction. The potential losses due to wake effects between adjacent rows are not considered in this work, due to computational and time limitations. The last set of simulations was based on the dephased layout with 2R dephasing and considered different turbine spacing. All of the simulation cases are listed in Table 5.1.

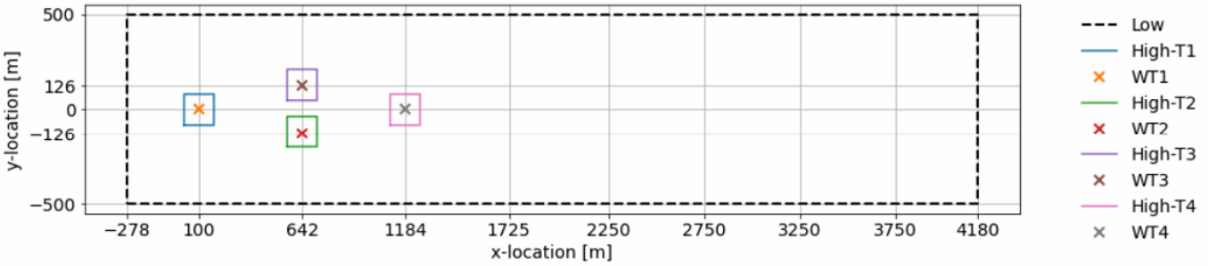

**Figure 5.1:** Diamond-2R wind farm layout case diagram. ”WT” stands for wind turbine; ”Low” stands for the low resolution domain boundary; and High-TX stands for high resolution domain for turbine X.

**Table 5.1:** Study cases summary.

| Set case study variation | Set case study name | Notes |
|---|---|---|
| Turbine spacing | 3D | The spacing values are presented in the rotor diameter multiple. |
| | Base case 4.3D | |
| | 6D | |
| | 8D | |
| | 10D | |
| | 12D | |
| | 14D | |
| | 16D | |
| | 18D | |
| Turbine height | ALLTRB_78m | ALLTRB meaning all of the wind farm turbines have the specified hub height. |
| | Base case ALLTRB_90m | |
| | ALLTRB_102m | |
| | ALLTRB_109m | |
| | WT1_90m<br>WT2_78m<br>WT3_90m<br>WT4_78m | |
| | WT1_102m<br>WT2_78m<br>WT3_102m<br>WT4_78m | |
| | WT1_102m<br>WT2_78m<br>WT3_78m<br>WT4_102m | |
| | WT1_109m<br>WT2_78m<br>WT3_109m<br>WT4_78m | |
| | WT1_109m<br>WT2_90m<br>WT3_109m<br>WT4_90m | |
| Wind farm layout | 4.3D_Dephased_1R | Dephased and Diamond signify the farm layout and R multiples specify the dephasing distances. |
| | 4.3D_Dephased_2R | |
| | 4.3D_Dephased_3R | |
| | 4.3D_Dephased_4R | |
| | 4.3D_Diamond_2R | |
| Dephased layout with different turbine spacings | 4.3D_Dephased_2R | |
| | 6D_Dephased_2R | |
| | 8D_Dephased_2R | |
| | 10D_Dephased_2R | |

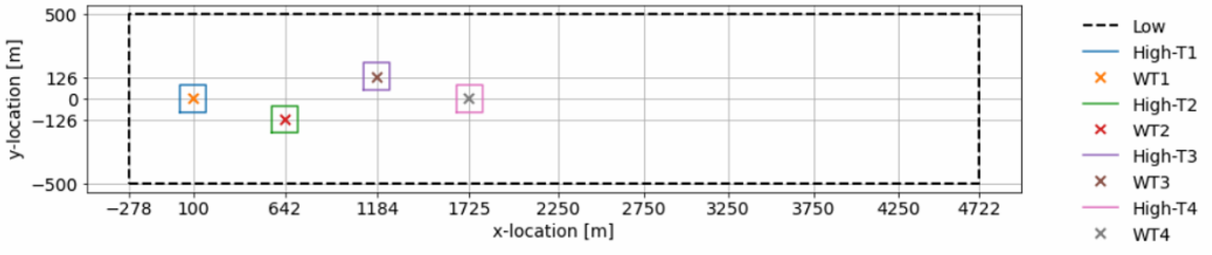

**Figure 5.2:** Dephased-2R wind farm layout case diagram. ”WT” stands for wind turbine; ”Low” stands for the low resolution domain boundary; and High-TX stands for high resolution domain for turbine X.

## 5.2 Base case results

### 5.2.1 Power generation and energy yield results

The simulated power generation of each turbine in the base case, which was described in Chapter 3, was taken to determine the power curves for all of the turbines, which are shown in Figure 5.3. The graph on the left represents the WT1 mean power values with error bars based on the standard deviation. The variations in turbine power are caused by the floating platform motions, different wakes impact, and the fact, that the generated inflow wind profiles are turbulent and do not have the same velocity parameters at every timestep. WT1 power curve along with the rotational speed and blade pitch angle presented in Figure 5.4 were compared with the nominal NREL 5 MW turbine values, presented in [89]. Based on the document, the rated wind speed for this turbine is equal to 11.4 m/s, therefore the turbine should start operating with its nominal power at the 11 m/s to 12 m/s range, and keep the power generation close to the rated values until 25 m/s wind speed. It is coherent with the acquired results. On the right graph in Figure 5.3, one can notice the differences in power curves for different turbines with WT1 having generated the highest power up to about 15 m/s, and WT2, WT3, and WT4 operating with lower power output. The second, third and fourth wind turbines generated 21.8%, 25.9%, and 27.2% less electricity per year respectively, in comparison to the first wind turbine in a row. Obtained values of rotational speed and blade pitch angles match the values presented by NREL [89].

The power curves presented in Figure 5.3 were used to calculate the annual electricity production per turbine and for the whole farm, along with the annual energy farm losses due to the wake effects, capacity factor, and energy yield density values, using the procedure described in Section 4.2. A summary of the results for the base case is presented in Table 5.2. It is noticeable that the subsequent turbines generate less electricity per year with the highest difference between the first and the second turbine. The wake losses percentage is equal to $\Delta AEP_{\text{wake}}$ = 18.7%. According to Barthelmie R. J. et. al. [113], typical annual wake losses in wind farms are ranging from 10% to 20%, so the results obtained are coherent with the reported values. The capacity factor of the farm is 34.6%, which is in accordance with the literature [114], stating that different studied cases' CF values range from 34.56% to 53.26%; and Kekana H. et. al. [112] having obtained similar values.

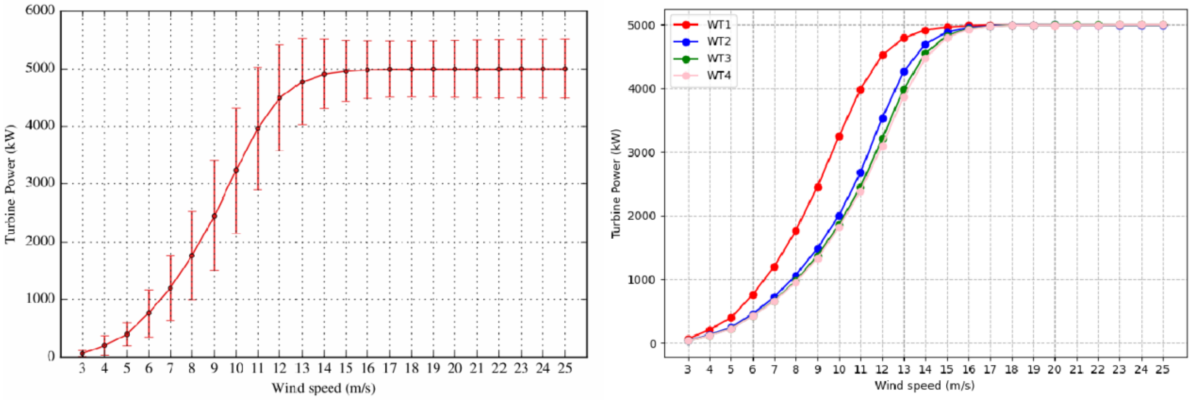

**Figure 5.3:** Base case wind turbine power simulations results. The left diagram shows the mean power generated by the first turbine (WT1) with the errorbars based on standard deviation. The right diagram shows the mean calculated values for every turbine.

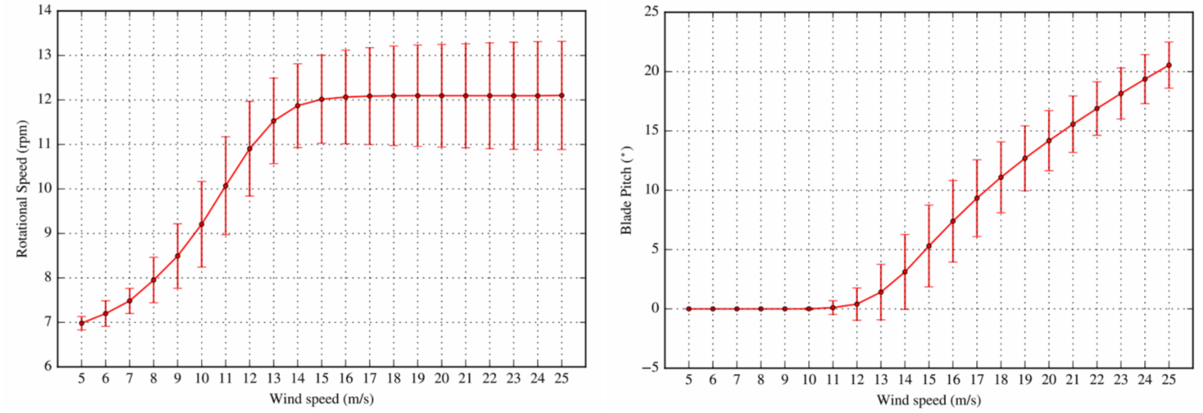

**Figure 5.4:** Base case wind turbine blade pitch and rotational speed results. The left diagram shows the mean rotational speed and the right one presented the first blade pitch of the first turbine (WT1) with the errorbars based on standard deviation.

**Table 5.2:** Electricity generation, wake losses, capacity factor and the energy yield density values for the base case simulation.

| Name | Value | Unit |
|---|---|---|
| $AEP_{\text{WT1}}$ | 20.6 | GWh/year |
| $AEP_{\text{WT2}}$ | 16.1 | GWh/year |
| $AEP_{\text{WT3}}$ | 15.3 | GWh/year |
| $AEP_{\text{WT4}}$ | 15.0 | GWh/year |
| $AEP_{\text{farm, gross}}$ | 335.6 | GWh/year |
| $AEP_{\text{farm, net}}$ | 302.9 | GWh/year |
| $AEP_{\text{farm, ideal}}$ | 412.9 | GWh/year |
| $\Delta AEP_{\text{wake}}$ | 18.7 | % |
| $CF$ | 34.6 | % |
| $EYD$ | 112.0 | GWh/(year $\cdot km^2$) |

### 5.2.2 Base case cost analysis

Using the model presented in section 4.3, total CAPEX and DECEX, and annual OPEX for the base case were calculated and are presented below. The sum of all of the costs needed for the construction, exploitation, and dismantling of the wind farm equals 712.30 M€. The total capital expenditures for the development phase and materials needed, shown in Table 5.3, amounted to 440.92 M€, of which the largest costs are for the SS platforms. Total installation costs associated with the construction of the wind farm were 43.29 M€. The OPEX are presented in Table 5.4 and amount to 223.31 M€ (95.35 M€ when discounted) during the project lifetime. It was found that the annual OPEX reached a value equal to 8.93 M€/year, of which wind farm operational expenditures were 3.17M€, and the maintenance costs were 5.76 M€. The DECEX amounted to 14.76 M€.

**Table 5.3:** CAPEX: material and installation costs calculated for the base case.

| **Name** | **Cost (M€)** |
|---|---|
| **Total material CAPEX** | **440.94** |
| Contingency cost | 40.25 |
| Project development cost | 8.14 |
| Construction insurance cost | 5.25 |
| Total Turbines cost | 122.00 |
| Total SS platforms cost | 190.00 |
| Material cost per platform | 8.69 |
| Direct labour cost per platform | 0.74 |
| Total transmission system cost | 43.1 |
| Total cost of cables | 21.64 |
| Offshore substation cost | 11.77 |
| Onshore substation cost | 5.88 |
| SCADA system cost | 1.79 |
| Grid connection cost | 2.00 |
| Total mooring system cost | 30.70 |
| Total anchoring system cost | 1.48 |
| **Total installation CAPEX** | **43.29** |
| Wind turbine installation | 0.13 |
| Floating platform installation | 8.10 |
| Total transmission system installation | 29.46 |
| Installation cost of array cables | 12.50 |
| Installation cost of export cable | 15.02 |
| Installation cost of onshore cables | 0.49 |
| Offshore substation cost | 0.42 |
| Onshore substation cost | 1.04 |
| Total mooring and anchoring inst. | 5.55 |

**Table 5.4:** OPEX and DECEX calculated for the base case.

| **Name** | **Cost** | **Unit** |
|---|---|---|
| **Total OPEX** | **223.31** | **M€** |
| **Total discounted OPEX** | **95.35** | **M€** |
| **Annual OPEX** | **8.93** | **M€/year** |
| **Total operational expenditures** | **3.17** | **M€/year** |
| Management | 0.08 | M€/year |
| Marine operations | 0.13 | M€/year |
| Weather forecasting | 0.01 | M€/year |
| Condition monitoring | 0.08 | M€/year |
| Operating facilities | 0.14 | M€/year |
| HSE monitoring | 0.05 | M€/year |
| Insurance | 2.18 | M€/year |
| Landlease | 0.50 | M€/year |
| **Total maintenance expenditures** | **5.76** | **M€/year** |
| Turbine reset cost | 1.58 | M€/year |
| Minor turbine repair cost | 1.17 | M€/year |
| Medium turbine repair cost | 0.34 | M€/year |
| Major turbine repair cost | 0.29 | M€/year |
| Major replacement cost | 1.74 | M€/year |
| Minor fundation repair cost | 0.01 | M€/year |
| Minor substation repair cost | 0.01 | M€/year |
| Major substation repair cost | 0.27 | M€/year |
| Cable repair cost | 0.36 | M€/year |
| **Total DECEX** | **14.76** | **M€** |
| Dismantling costs of the platforms | 5.70 | M€ |
| Dismantling costs of cables | 2.75 | M€ |
| Dismantling costs of substations | 3.75 | M€ |
| Dismantling costs of mooring and anchoring systems | 4.97 | M€ |

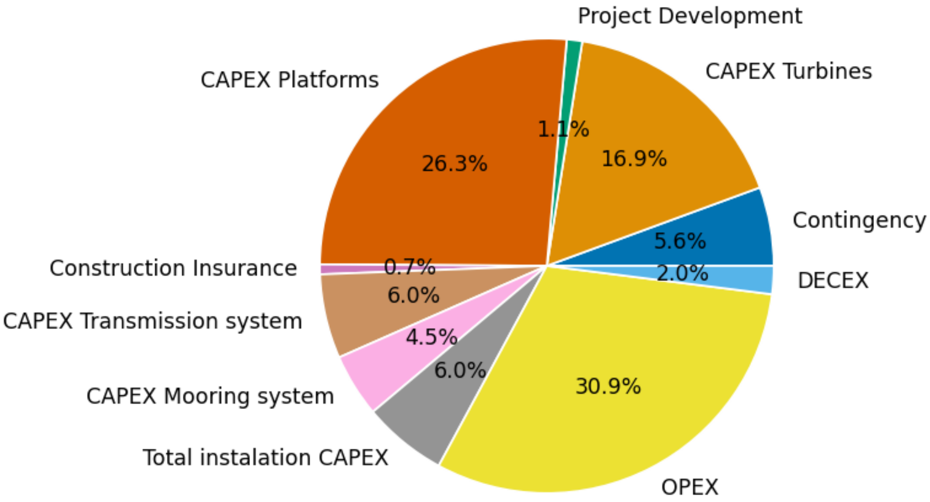

**Figure 5.5:** Base case total wind farm expenditures percentage shares estimated based upon the cost model in this thesis.

Based on the cost analysis, a pie chart, presented in Figure 5.5 was created, that shows the share of individual expenses in relation to the total costs of the project. The chart shows that the largest contribution to the total expenses for the wind farm makes the CAPEX, which together amount to as much as 67.1%. The OPEX expenses are equal to 30.9% and the DECEX cover 2% of the total expenses.

In order to verify the cost model, the obtained percentages were compared to the LCOE contribution factors presented in Figure 2.8 that was based on a study done by Tyler Stehly and Patrick Duffy from NREL [47]. The main components' comparison is summarized in Table 5.5. It can be noticed that the shares of different cost components obtained in this study are similar to the ones listed in the reference paper, especially the turbines and platforms expenses, installation and commissioning costs, OPEX and DECEX values. The transmission system values are undervalued in comparison to the NREL report. However, these expenses are deeply based on the cable lengths and the farm distance from the shore and are dependent on the specific farm designs.

**Table 5.5:** Comparison of selected costs components' shares between this thesis and NREL Report [47] for the cost model validation.

| | **Cost components percentage shares (%)** | |
|---|---|---|
| **Component** | **This thesis** | **NREL report** |
| Floating platforms | 26.3 | 27.1 |
| Turbines | 16.9 | 17.6 |
| Transmission system | 6.0 | 9.2 |
| Installation and commissioning | 6.0 | 6.4 |
| OPEX (O&M + landlease) | 30.9 | 29.8 |
| Decommissioning | 2.0 | 1.3 |

### 5.2.3 Base case LCOE values

Based on the presented cost analysis, the LCOE for the total lifespan of the farm (25 years) was **168.85 EUR/MWh**. To evaluate the LCOE, a discount rate, determined for developed countries, equal to WACC = 8% [13] was chosen. Obtained LCOE value for the wind farm under analysis is in line with the values published in the Offshore Wind Market Report [16] (presented in Figure 2.6), in which the values ranged from 80 USD/MWh to 190 USD/MWh. The calculated LCOE also falls within the range specified in the NREL Cost of Wind Energy Review report [47], which ranges from 71 USD/MWh to 173 USD/MWh for floating offshore wind farms.

## 5.3 Turbine spacing variations

Based on the work of Stanley APJ et. al. [53], increasing the turbines' spacing in a row, decreases the energy wake losses of the turbines, thus increasing the farm's annual electricity production and decreasing LCOE values. The reference study took the diameters ranging from 2D to 10D into consideration. This set of simulated cases considered turbines spacings equal to 3D, 4.3D (base case), 6D, 8D, 10D, 12D, 14D, 16D, and 18D, and the results of the first five cases are expected to match the tendencies obtained in the reference study. The obtained values of LCOE, capacity factor, wake losses, and energy yield density are presented in Figure 5.6. The annual net electricity production of the farm is presented in Table 5.6.

The AEP values in Table 5.6 present an increasing trend with the turbine spacing, which is coherent with the reference study [13]. The graphs presented in Figure 5.6 show that the LCOE, annual energy wake losses, and energy yield density decreased with increasing distance between the turbines in a given row and the capacity factor increased with the spacing distance for spacings from 3D to 10D and further until 18D. Therefore, the LCOE and wake losses decrease is in compliance with the reference study [13] as well.

**Table 5.6:** Net annual electricity farm production for different turbine spacing variations.

| **Turbine spacing** | $AEP_{\textbf{net, farm}}$ $\left(\frac{\textbf{GWh}}{\textbf{year}}\right)$ |
|---|---|
| 3D | 281.4 |
| Base case - 4.3D | 302.9 |
| 6D | 322.2 |
| 8D | 336.7 |
| 10D | 346.1 |
| 12D | 353.7 |
| 14D | 359.0 |
| 16D | 363.0 |
| 18D | 366.6 |

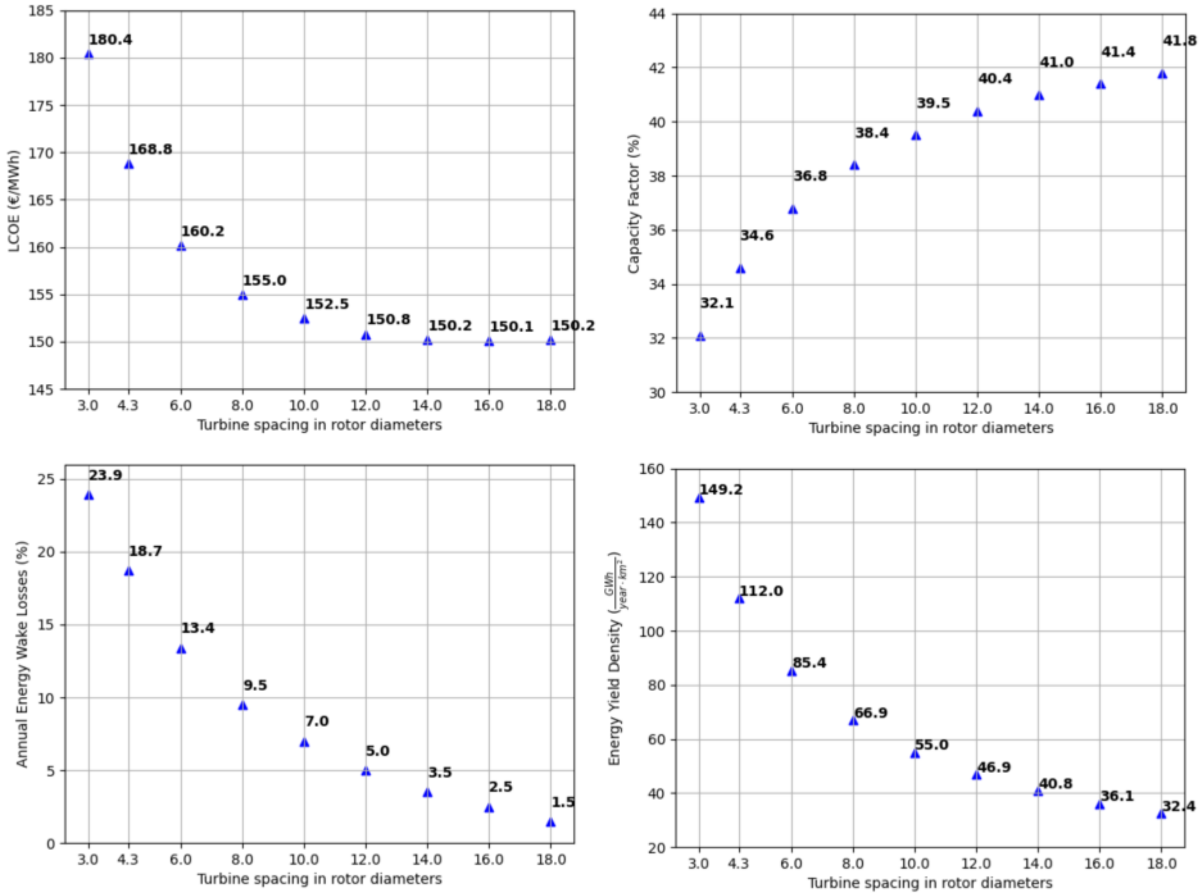

**Figure 5.6:** LCOE, capacity factor, AEP wake losses and energy yield density results for different wind turbine spacings in relation to the base case 4.3D.

As one can notice from the graph in Figure 5.6, increasing the distance between consecutive turbines in a row can significantly decrease the wake losses of the wind farm. Increasing the distance from the Base Case 4.3D to 18D can reduce the wake losses from 18.7% to 1.5%, which stands for a 17.2% difference. The decrease tends to be non-linear, as the wake turbulence in the wind starts to recover under the ambient wind influence downstream [56, 57]. Therefore, further turbine spacing increase would result in lower differences in wake losses reaching a point, where the losses decrease would be negligible. The LCOE values also tend to decrease with the turbine spacing distance, however, the decline is also non-linear, due to the non-linear decline of the wake losses explained above and increasing costs of components (e.g. array cables) and maintenance expenditures). Because of that, the LCOE values reach a point, where the wake losses differences become negligible, compared to the costs, and lead to a point, from which the continuously increasing expenditures will surpass the AEP gains from wake losses reduction. Analyzing the results in this study, this phenomenon occurs at the 14D to 16D spacing range, from where the LCOE values start to rise. Based on that and relatively low differences between capacity factors at this range, the most energy- and cost-efficient turbine spacings may lie within the 12D to 14D span, where the levelized cost of energy values can be decreased by 10.7% and 11.0% respectively, compared to the base case. However, this must be considered a qualitative observation, due to uncertainties associated with the assumed LCOE and energy calculations.

On the other hand, the energy yield values show a significant decrease with the spacing distance at lower spacings (3D - 10D), and a smoother decrease in the larger spacings. A larger wind farm area takes up more, which makes it more difficult for maritime vehicles to navigate through. It can also lead to longer installation and maintenance work times, which need to be addressed, but are difficult to quantitatively determine, due to a lack of commercially available information.

## 5.4 Turbine hub height variations

The next main variable considered in this study is the turbine hub height. The base case, which in this set of simulations is labeled as ALLTRB_90m, was used as the reference, so all of the characteristics, apart from the turbine hub height remained the same. The first four simulation cases, having all of the turbines (ALLTRB) equal to 78 m, 90 m (base case), 102 m and 109 m were done to verify the simulation settings in this set. It is expected that due to higher wind speeds at higher altitudes, an increase in turbine hub height would result in higher electricity production. The remaining cases present different configurations of turbines in a row in regards to their hub height, based on the concept presented in Section 2.7.3. The first configuration (90m_78m) has the first and the third turbines' hub height at 90 m, and the second and fourth turbines' hubs at 78 m height. The same arrangement applies to the 102m_78m, 109m_78m, and 109m_90m cases. The 102_78m_seq1221 case has a different hub height sequence, having the first and fourth turbines' hub at 102 m height and the remaining ones at 78 m.

In order to estimate the tower properties of different turbines used in this set of simulations, Solidworks models of 78 m, 90 m, 102 m, and 109 m turbine towers were designed, and based on them, specific tower diameters, wall thicknesses, and mass densities in different tower elevations were calculated. Based on that, approximations of the total tower mass for each of the turbines were done in order to use them in the cost model and calculate the $z$-direction center of mass of the platform for each of the cases. The adjustments were done in such a way, that the top diameter of the tower equal to 3.87 m was fixed, as per the original tower design, and the tower properties were changed from its base, following the same properties trend. In the cost model, the difference in tower mass of all of the turbines in a farm, multiplied by the cost of steel specified in Table 4.2 was either added or subtracted from the initial turbines' expenditures in the base case in order to obtain the final material expenditures for different turbines. The tower height and mass with the SS platform center of mass calculated for the different turbines used are presented in Table 5.7.

**Table 5.7:** Tower height, approximate tower mass and semi-submersible platform center of mass relative to the sea water level (SWL) for turbines with different hub heights used in the thesis.

| Hub height (m) | Tower height (m) | Tower mass (tons) | Platform CM (m) |
|---|---|---|---|
| 78 | 75.6 | 196.7 | -10.6 |
| 90 | 87.6 | 249.7 | -8.7 |
| 102 | 99.6 | 308.9 | -6.6 |
| 109 | 106.6 | 346.3 | -5.3 |

### 5.4.1 Hub height variations: Platform motions and tower base loads

The differences in the total mass of the turbine change the platforms' center of mass and higher towers increase the load moments induced on the bases of the turbines. A higher platform's center of mass may lead to increased values of maximum heave, pitch, roll, surge, sway, and yaw motions, which may lead to platform destabilization or mooring lines failure due to increased loads. In order to estimate the impact of higher hub heights on the platform movements, an analysis of minimum and maximum platform motion values was done using the results obtained from FAST.Farm. The examined results are presented in Figure 5.7. According to the performed simulations, the platform maintained its stability for every increased hub height case. Looking at the graphs, it can be noticed that the heave, pitch, roll, surge, and yaw extreme displacements are increased for the higher turbine hub heights. The biggest relative difference can be observed in the roll and yaw motion. When it comes to the surge motion, the differences are negligible. In regards to the mooring lines' loads, the platform movements obtained in this study were compared with the mooring load-displacement analysis performed by NREL [88] that is shown in Figure 5.8. None of the mooring lines' loads, exerted by the platform movements, surpassed the failure values. Therefore, based on the above analysis, it is assumed that the platform and the mooring lines maintained their stability and integrity in every analyzed hub height case.

In order to check the impact of the turbine heights on the moments exerted on the base of the turbine towers, maximum $x$-, $y$- and $z$-direction tower base moments were simulated using the FAST.Farm software. The results for the respective moment directions were presented in Figures 5.9, 5.10 and 5.12. It can be noticed that the 102 m and 109 m turbine hub height towers' $x$- and $y$-direction base load moments are significantly higher compared to the base case. The moments in the $z$-direction had similar values for all of the cases. Increased tower base moments escalate the fatigue on the turbine towers, which may lead to a decreased lifetime of the farm, or increased maintenance expenditures due to a higher probability of turbine malfunction. These factors may impact the LCOE of the wind farm. For that reason, it may be beneficial to conduct a more detailed fatigue analysis in the future, as it is outside the scope of this work.

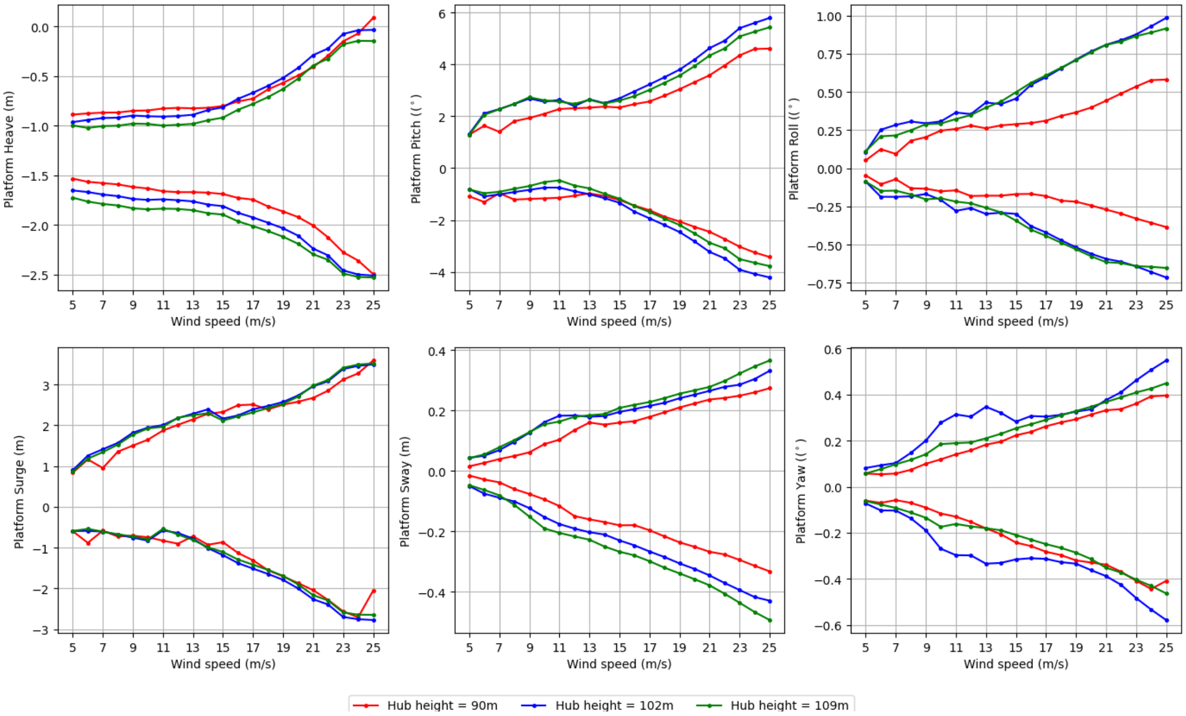

**Figure 5.7:** Simulated maximum and minimum platform movements for turbines with the 90 m, 102 m, and 109 m hub heights.

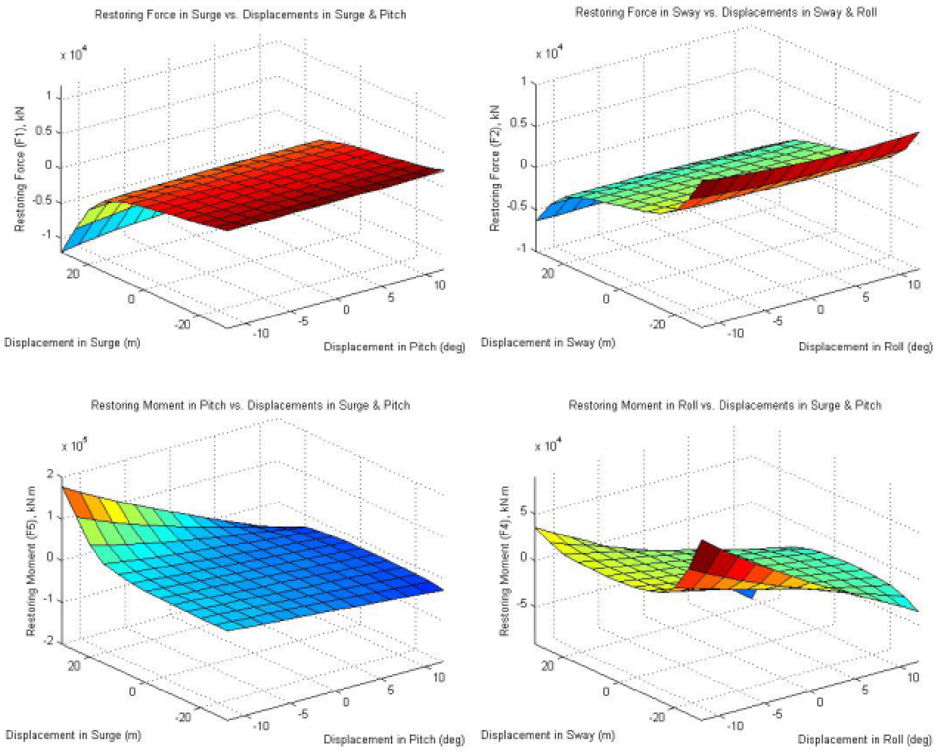

**Figure 5.8:** Platform motions dependent mooring loads analysis for the OC4 semi-submersible platform performed by NREL [88].

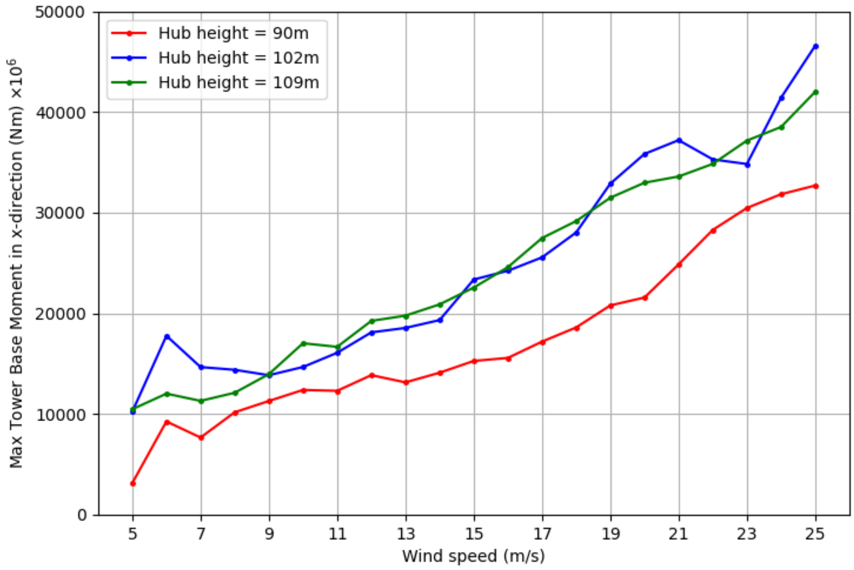

**Figure 5.9:** Maximum moments on the base of the turbine tower in the $x$-direction for turbines with 90 m, 102 m, and 109 m hub heights.

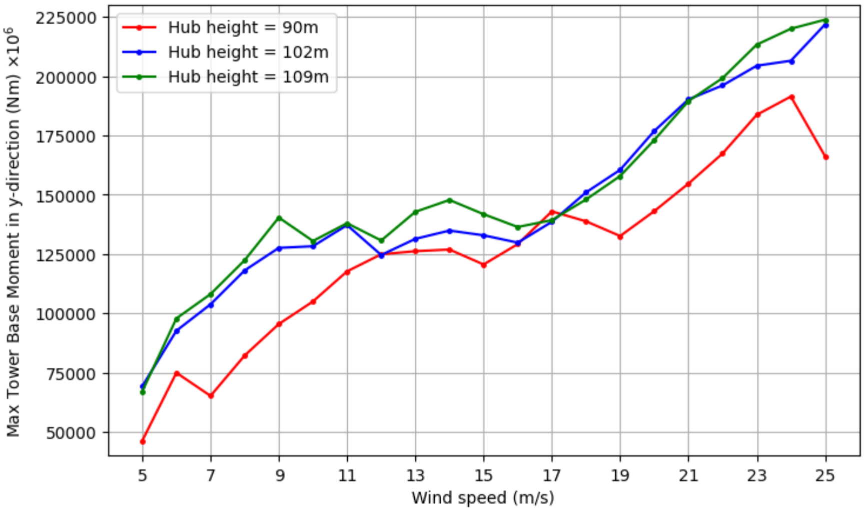

**Figure 5.10:** Maximum moments on the base of the turbine tower in the $y$-direction for turbines with 90 m, 102 m, and 109 m hub heights.

### 5.4.2 Hub height variations: AEP and LCOE results

The net AEP results for all of the cases are presented in Table 5.8. It can be noticed that, as expected, the ALLTRB configurations present an increase in AEP with the increase in hub height. Looking at the results, it can be noticed, that the highest and the lowest AEP were obtained when all of the turbines were at 109 m, and 78 m hub height respectively. Differentiation in consecutive turbine hub heights has shown lower annual electricity production values compared to their reference ALLTRB cases. The 90m_78m, 102m_78m, 109m_78m, and 109m_90m cases had obtained lower AEP values than the

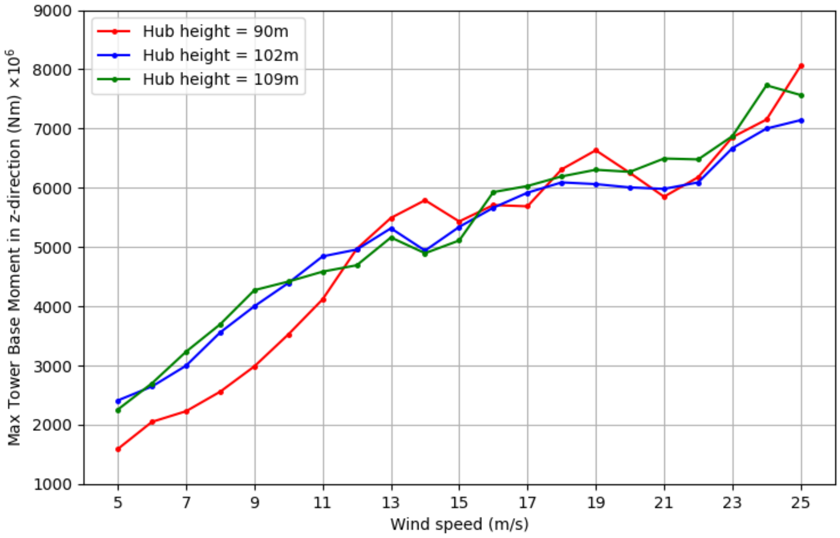

**Figure 5.11:** Maximum moments on the base of the turbine tower in the $z$-direction for turbines with 90m, 102m, and 109m hub heights.

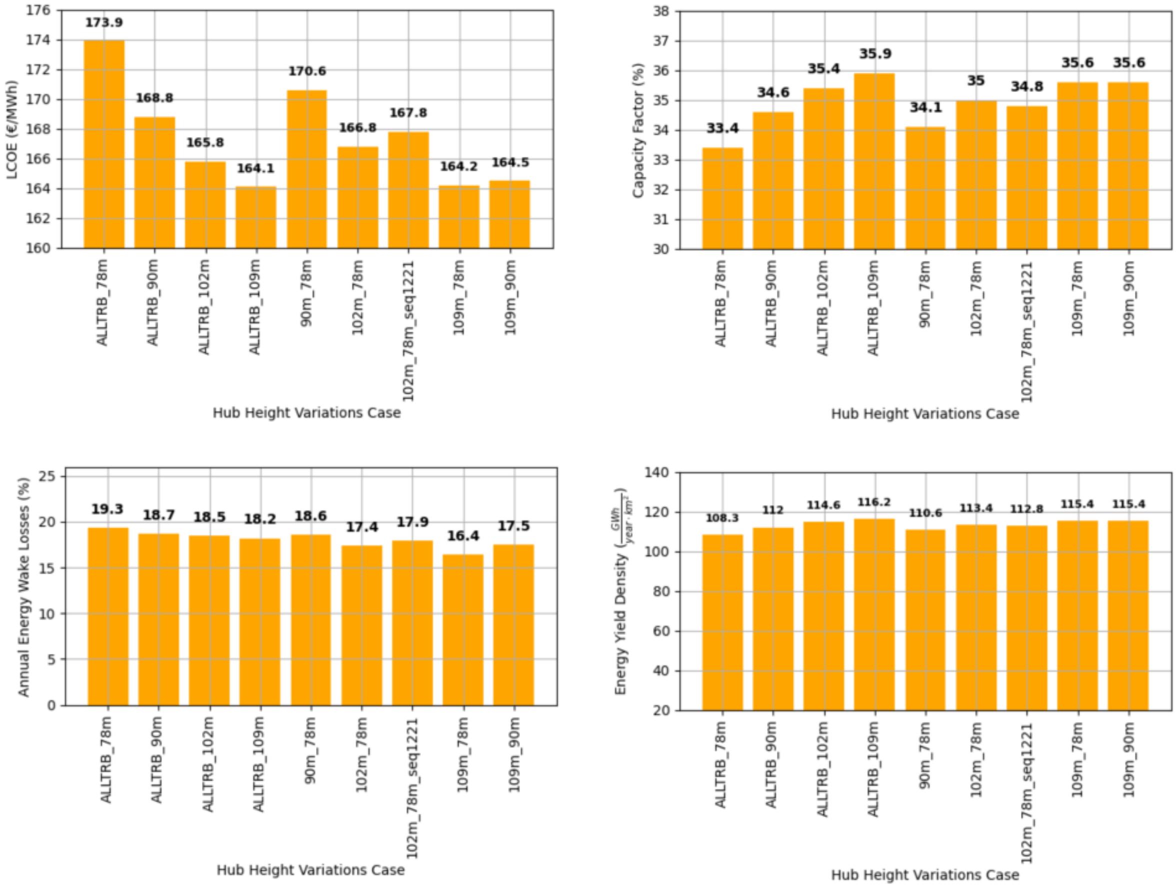

**Figure 5.12:** LCOE, capacity factor, AEP wake losses and energy yield density results for different wind turbine hub height variations in relation to the base case 4.3D (ALLTRB_90m).

ALLTRB_90m, ALLTRB_102m, and ALLTRB_109m respective cases. Looking at the results, one can notice that the increased energy yield gained from making the turbines' hub heights higher surpasses the relative reduction of energy wake losses accomplished by the WT2 and WT4 hub height reductions. For example, the ALLTRB_109m case, reaching the $AEP_{\text{net, farm}}$ = 314.1 (GWh/year) had a higher energy yield than the 109m_90m and the 109m_78m case, having the $AEP_{\text{net, farm}}$ = 312.1 (GWh/year). It means, that the energy wake losses reduction due to the differentiation in consecutive turbine hub heights is lower than the energy yield increase due to the higher hub heights. The 109m_90m and the 109m_78m configuration have both obtained the same annual electricity production. The 109m_78m variation has obtained lower wake losses than the 109m_90m configuration. However, the energy losses due to the wake effects are compensated by higher wind speeds at elevations of 90 m compared to 78 m, which result in higher power generation of the 90 m turbines in the 109m_90m variation compared to the other configuration, and this may be the cause of equal AEP values.

Having smaller turbine towers lowers the CAPEX of the wind farm, which is why the LCOE values need to be taken into consideration as well. The LCOE, along with the wind farm capacity factors, energy wake losses, and the energy yield density results are presented in Figure 5.12.

**Table 5.8:** Net annual electricity farm production for different turbine hub height variations.

| **Turbine hub height variation** | $AEP_{\textbf{net, farm}}$ $(\frac{\textbf{GWh}}{\textbf{year}})$ |
|---|---|
| ALLTRB_78m | 292.8 |
| Base case ALLTRB_90m | 302.9 |
| ALLTRB_102m | 309.9 |
| ALLTRB_109m | 314.1 |
| 90m_78m | 299.1 |
| 102m_78m | 306.7 |
| 102m_78m_seq1221 | 304.8 |
| 109m_78m | 312.1 |
| 109m_90m | 312.1 |

As one can notice, looking at the graph 5.12, the lowest LCOE values were obtained for the ALLTRB_109m case, followed by the 109m_78m, 109m_90m, and ALLTRB_102m cases. The highest capacity factors and EYD values were achieved in the same order of the cases. On the other hand, the lowest energy wake losses were obtained for the highest differences in consecutive turbine hub height configurations (109m_78m, 102m_78m, and 109m_90m), which means that the wake losses reduction can be obtained by varying the turbine hub heights in the farm. Nevertheless, this reduction of the wake losses is too small to make a significant power generation difference in the simulated cases. Additionally, the turbine material CAPEX savings are too low to compensate for the decreased energy yield of the lowered turbines.

Another important aspect that needs to be mentioned is the manufacturing process of turbines with different hub heights. As the industry is moving towards the automation of processes, including turbine tower manufacturing [115], large assembly and manufacturing systems would need to be reprogrammed and readjusted for a different tower height. This could increase the production time and costs of the turbines for a wind farm. Considering the results and the aforementioned higher fatigue issues, varying turbine hub heights may not provide a profitable and viable solution for wake losses and LCOE reductions. However, the cost model considers only the material cost, and not manufacturing and labor expenditures reductions, which may contribute to a levelized cost of energy reduction.

## 5.5 Wind farm layout variations

The last set of simulations considered different layouts of wind farms, namely the dephased and diamond configurations described at the beginning of this chapter. Firstly, both of the configurations were simulated for turbine dephasing equal to 2R. After that, in order to analyze the impact of different dephasing values, ranging from 1R to 4R, on the AEP and other evaluation factors, the dephased-1R, -3R, and -4R cases were prepared and simulated. The AEP results for the above-mentioned cases are presented in Table 5.9. Clear differences in $AEP_{\text{net, farm}}$ compared to the base case can be seen. As the dephasing radius increases, the value of annual electricity production increases. For the analyzed 4R-dephasing case, a 21% higher value was observed with respect to the base case. The dephased-2R layout demonstrated a slightly higher annual electricity production values $AEP_{\text{net, farm}} = 353.4$ (GWh/year) compared to the diamond-2R layout with $AEP_{\text{net, farm}} = 349.5$ (GWh/year). The analysis of the data obtained from the simulations performed showed that the highest AEP value was obtained for the dephased_4R wind turbine configuration.

**Table 5.9:** Net annual electricity farm production for different wind farm layout variations.

| **Farm layout variation** | $AEP_{\textbf{net, farm}}$ $(\frac{\textbf{GWh}}{\textbf{year}})$ |
|---|---|
| Base case - 4.3D | 302.9 |
| 4.3D_Dephased_1R | 331.1 |
| 4.3D_Dephased_2R | 353.4 |
| 4.3D_Dephased_3R | 363.3 |
| 4.3D_Dephased_4R | 366.4 |
| 4.3D_Diamond_2R | 349.5 |

Based on the simulated AEP results, the graphs representing LCOE, capacity factor, energy wake losses, and energy yield density values are presented in Figure 5.13 and Figure 5.14 in order to show the differences between dephased-2R and diamond-2R layouts, as well as the different R-dephasing values.

As one can notice from Figure 5.13, proposed layouts show a significant decrease of LCOE values compared to the base case, with 13.3% and 14.3% decrease for the diamond and dephased layout respectively. Energy wake losses were also significantly decreased to 6.1% and 5.1% for the diamond and dephased layouts, which correspond to the wake losses decrease of 10D - 12D turbine spacing. The differences in LCOE, $\Delta AEP_{\text{wake}}$, and capacity factors between both of the layouts are small. However, the energy yield density results showed a substantially higher value for the diamond layout compared to the dephased one. It is due to the fact, that the diamond layout reduces the turbine rows length by placing WT2 and WT3 at the same $y$-direction distance, reducing the total wind farm area. Based on the small differences in LCOE, CF, and wake losses between the two cases, and significantly higher EYD values in the diamond layout, it can be stated that the diamond layout is better and could be further researched.

When analyzing the results of different R-dephasing values, presented in Figure 5.14, it can be noticed that the higher the dephasing distance is, the lower the LCOE and wake losses values are, and the higher the capacity factor values are. It can be noticed, that dephasing the turbines significantly reduces the wake losses, even down to 1.6% for the 4R-dephasing compared to the base case 18.7%. The wake losses present a similar, non-linear trend to the turbine spacings simulation cases set, with small wake

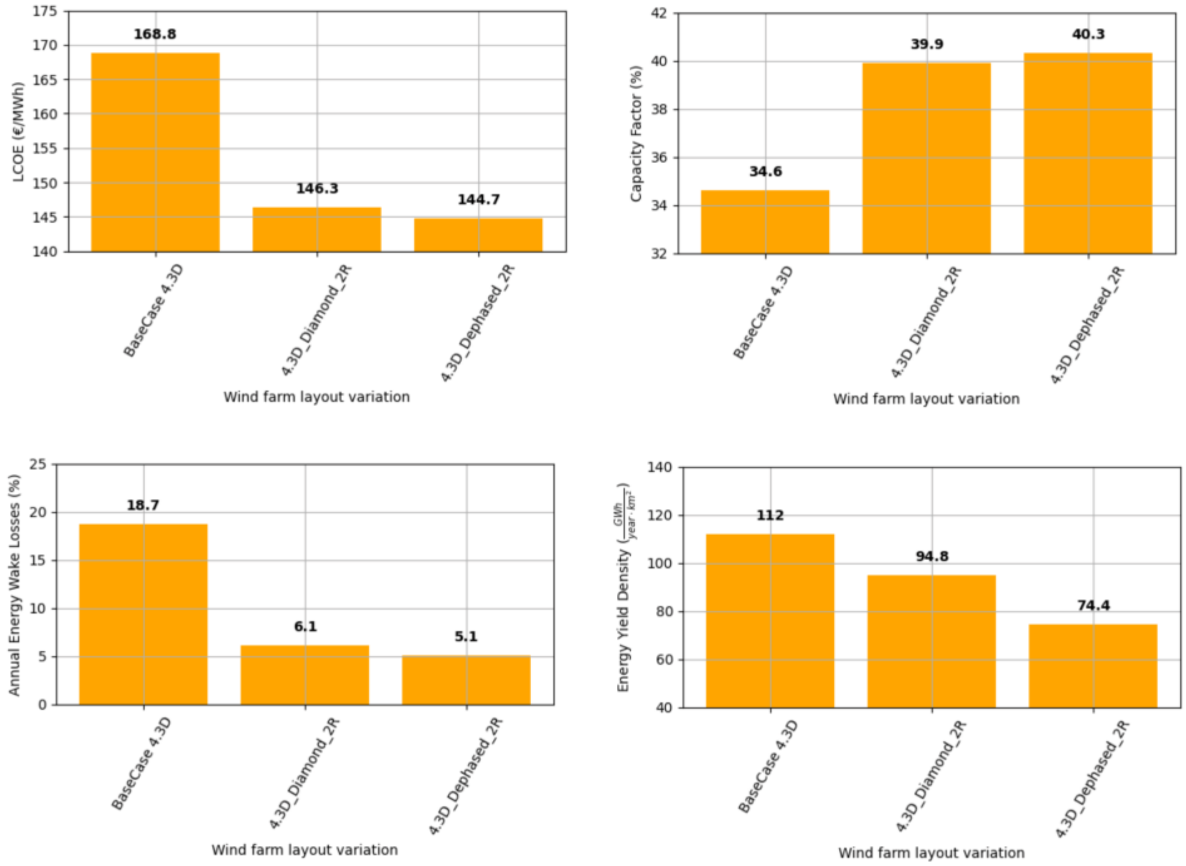

**Figure 5.13:** LCOE, capacity factor, AEP wake losses and energy yield density results for the 2R Dephased and Diamond wind farm layouts in relation to the base case 4.3D.

losses differences between the 3R- and 4R-dephasing. Therefore, the LCOE trend is non-linear and similar to the one obtained in the first case study set. That is why, it is expected that the wake losses reduction will become so small, that the increasing expenditures caused by larger farm areas will surpass the AEP gains from further turbine dephasing leading to a values change similar to the one obtained in Figure 5.6. As the LCOE, wake losses, and capacity factor differences between the 3R and the 4R case are negligible and the energy yield differences are significant, it can be stated that the highest profitable dephasing distance is 3R.

As mentioned in section 1.3 of the thesis, the simulations were done for only one row of a wind farm. That is why, in order to minimize the impact of the wake losses induced by the turbines in the other rows, the far dephased turbines in every row were placed at a vertical distance of 3.3D (based on the reference case) between each other. It may be possible to decrease the distance between the subsequent rows, thus decreasing the area of the farm, and the LCOE and increasing the energy yield density. In order to achieve that, further analysis needs to be done, that simulates the wake effects of one turbine row on the others and determines the minimal distance between the turbine rows for which subsequent rows are not affected by the wake of the other ones. However, this is outside of the scope of this work.

In order to determine the turbine spacing impact on the dephased layouts, simulations were performed for the 2R-dephased layout with 4.3D, 6D, 8D, and 10D turbine spacings. The results of AEP for the analyzed cases are shown in Table 5.10. As seen in the previous simulations set, compared to the base

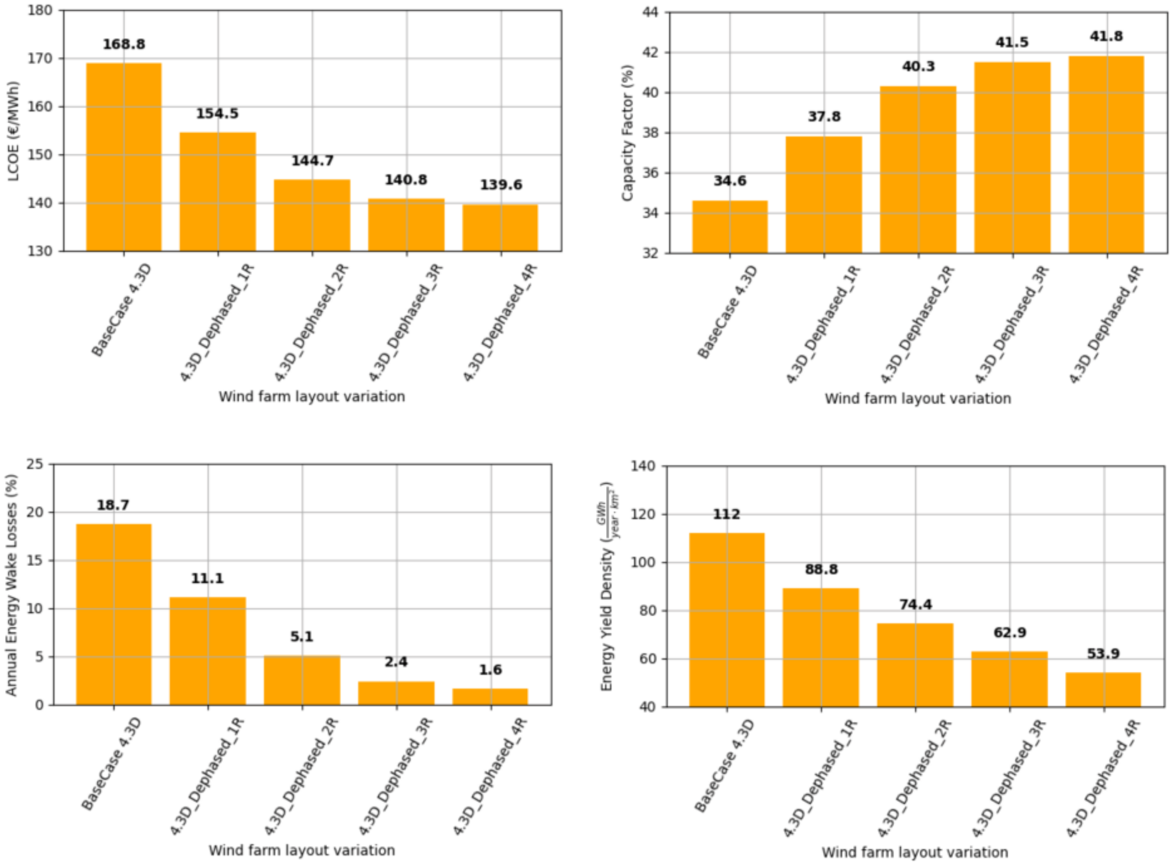

**Figure 5.14:** LCOE, capacity factor, AEP wake losses and energy yield density results for different R-dephasing values of the 4.3D Dephased farm layout in relation to the base case 4.3D.

case, the $AEP_{\text{net, farm}}$ values were significantly larger. However, longer distances between the turbines in a row showed exiguous differences between the analyzed configurations, indicating the negligible impact of the distribution of turbines in rows on the performance of dephased wind farms.

**Table 5.10:** Net annual electricity farm production for different turbine spacing in the 2R-Dephased wind farm layout.

| **Turbine spacing variation** | $AEP_{\textbf{net, farm}}$ ($\frac{\textbf{GWh}}{\textbf{year}}$) |
|---|---|
| Base case - 4.3D | 302.9 |
| 4.3D_Dephased_2R | 353.4 |
| 6D_Dephased_2R | 356.3 |
| 8D_Dephased_2R | 359.4 |
| 10D_Dephased_2R | 361.8 |

The graphs represented in Figure 5.15 illustrate the relationships between the turbine spacing for the 2R-dephased case and the values of LCOE, CF, energy wake losses, and EYD. The largest differences were registered in the case of the energy yield density analysis, with a decreasing trend observed. In regards to the other evaluation factors, the values' differences were negligible. The LCOE results, due to the larger farm areas and therefore, higher expenditures, showed a decreasing trend with the increasing turbine spacing in the 2R-dephased case. Based on the above, the impact of increased turbine spacing in this case is negative, although insignificant, and the most cost-efficient configuration analyzed in this simulation set is the 4.3D_Dephased_2R one.

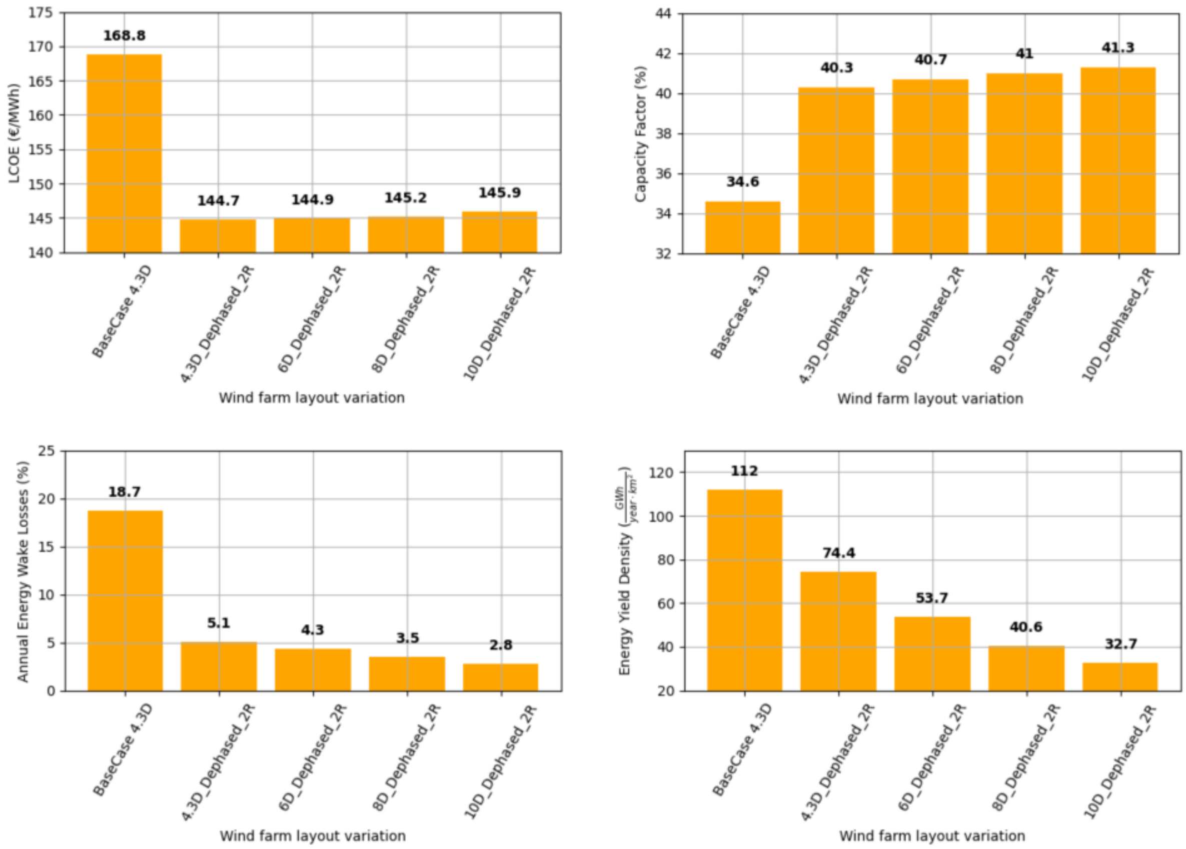

**Figure 5.15:** LCOE, capacity factor, AEP wake losses and energy yield density results for different turbine spacings in the 2R-Dephased farm layout in relation to the base case 4.3D.

## 5.6 Floating platform size variations

Before attempting to simulate additional cases with the floating platform size variations, a quick estimation of the LCOE values was done, based on the ALLTRB_78m case. Reducing the platform size may significantly increase its motions, due to its second moment of area reduction. Therefore, a case with smaller turbines (78 m) was chosen, because of its lower impact on the platforms' dynamic stability.

The energy yield was assumed to be the same as in the ALLTRB_78m case. It is expected, that the change in the platform size may slightly impact the power generation of the turbines, however, in this quick estimation, the variations in power generation were assumed to be negligible. Different platform size reductions, ranging from 2% to 10% with a 2% step, were applied to the cost model used in this thesis. The variable affected by the scaling was the platform structural mass. The results including the LCOE and LCOE reductions relative to the original platform size are presented in Table 5.11. It can be noticed, that the platform size reduction has a low impact on the levelized cost of energy, lowering the LCOE by 3.4% at a 10% platform size reduction. Such a reduction of the platform size may significantly impact the platforms' dynamic stability, and may lead to platforms' destabilization, especially when considering higher turbine hub heights. Considering the low impact of platform size reductions on the LCOE and the uncertainty over platforms' destabilization, the simulations of the platform size variations were not done in this thesis.

**Table 5.11:** Platform size reduction impact on LCOE based on the ALLTRB_78m case.

| Platform size reduction | LCOE (€/MWh) | LCOE reduction related to the original size |
|---|---|---|
| 0% | 173.9 | 0.0% |
| 2% | 172.7 | 0.7% |
| 4% | 171.6 | 1.3% |
| 6% | 170.4 | 2.0% |
| 8% | 169.2 | 2.7% |
| 10% | 168.0 | 3.4% |

## 5.7 Results summary

Based on the results for every simulation set, the best configurations, described in the above sections, for every set were selected. Their AEP, LCOE, CF, energy wake losses, and EYD values along with a percentage of AEP and LCOE differences compared to the base case, were summarized in Table 5.12. It can be noticed, that in the turbine spacing variation cases, the highest obtained AEP values were for the 12D and 14D simulation cases, however, due to the increasing CAPEX and OPEX, the LCOE values for these cases were not the lowest. The lowest levelized cost of energy was obtained in the 3R-dephased and 2R-diamond cases. The highest obtained capacity factor values were for the 3R-dephased, 14D, and 12D simulation cases. The highest energy yield density results were obtained in the ALLTRB_109m and the base case configurations.

**Table 5.12:** Selection of the best simulation cases in each of the conducted simulation sets. The AEP increase and LCOE reduction rows represent the relative differences in the mentioned values in comparison to the base case.

| Factor | Base case | 12D | 14D | ALLTRB_109m | Diamond_2R | Deph_3R |
|---|---|---|---|---|---|---|
| AEP (GWh/year) | 302.9 | 353.7 | 363.0 | 314.1 | 349.5 | 363.3 |
| AEP increase (%) | - | 16.8 | 19.8 | 3.7 | 15.4 | 20.0 |
| LCOE (€/MWh) | 168.8 | 150.8 | 150.2 | 164.1 | 146.3 | 140.8 |
| LCOE reduction (%) | - | 9.9 | 10.1 | 2.7 | 13.3 | 16.0 |
| Capacity factor (%) | 34.6 | 40.4 | 41.0 | 35.9 | 39.9 | 41.5 |
| Wake losses (%) | 18.7 | 5.0 | 3.5 | 18.2 | 6.1 | 2.4 |
| EYD ($\frac{GWh}{year \cdot km^2}$) | 112.0 | 46.9 | 40.8 | 116.2 | 94.8 | 62.9 |

# Chapter 6

# Conclusions

This Master's thesis was conceived to investigate different levelized cost of energy reduction factors in floating offshore wind farms. The work was motivated by the worldwide need for a carbon-neutral society, the fast development and huge technical potential of offshore wind energy, and the need for a faster energy transition.

The main objective of this thesis was to investigate the potential levelized cost of energy reduction factors in floating offshore wind farms. It aimed to identify and evaluate techno-economically different strategies that can contribute to the overall performance and profitability improvements of floating offshore wind farms. The investigation comprised the identification of different LCOE cost reduction factors, a robust techno-economical wind farm evaluation methodology, and recommendations for improvements in the wind farm assessment procedures.

These goals were achieved through the use of advanced aero-hydro-servo-elastic simulation software and a literature-based cost assessment model. The tools were used to prepare numerical simulations and cost-modeling of twenty-five different wind farm case studies, varying in turbine spacing distances, turbine hub heights, farm layouts, and the floating platform size. The main farm evaluation factors addressed in this thesis are the annual electricity production, farm energy losses due to the wake effects, farm capacity factor, the levelized cost of energy, and an energy yield density factor, that was introduced in this thesis. The energy yield density factor describes the relationship between the annual electricity production of a wind farm and its surface area. The findings of this work are summarized in this chapter.

In this thesis, a reference wind farm (base case) was defined. The definition of the case included the selection of the turbine (NREL 5 MW reference turbine), the floating platform (NREL OC4 semi-submersible platform), the transmission system, and other main components. A specific farm location, off the port of Leixões, was selected and its wave and wind data characteristics were determined. The reference farm layout was based on the existing Lillgrund wind farm. Based on the base case, the other case studies were determined and divided into three sets: the first considering different turbine spacings in a row, the second regarding different turbine hub height configurations, and the third addressing different wind farm layouts.

The FAST.Farm software was used in this thesis to estimate different wind farms' performance.

Preliminary simulations' results were compared with the results provided by NREL in order to verify the settings for the considered 5 MW reference turbine. The results showed a good agreement with the reference NREL values. In order to further verify the simulation settings used, annual energy wake losses and capacity factor were calculated for the base case and compared to literature findings, which matched the obtained values. The base case wake losses amounted to 18.7%, which is coherent with literature values ranging between 10% to 20%. The capacity factor was equal to 34.6%, which was compared to literature CF values ranging between 34.56% to 53.25%.

The literature-based cost model prepared in this paper was verified by comparing the levelized cost of energy values and specific components' expenditures shares available in the literature with the results obtained for the base case. The base case LCOE was equal to 168.8 €/MWh, which is coherent with the 80 USD/MWh to 190 USD/MWh or 71 USD/MWh to 173 USD/MWh ranges for the floating offshore wind, presented in the literature.

Simulations of different turbine spacings ranging from 3D to 18D were conducted in order to determine the most profitable solution, which was determined to be 12D and 14D measured in multiples of turbine diameter. There is a non-linear LCOE decline in regards to the turbine spacing, due to a decreasing decline of the wake losses and increasing costs of components (e.g. array cables) and maintenance expenditures. It can be noticed that the LCOE values reach a point, where the wake losses differences between subsequent spacings become negligible, and compared to the costs, lead to a LCOE function change, from which the continuously increasing expenditures surpass the AEP gains from wake losses reduction. The wake model settings were verified by comparing the wake losses and LCOE values of increasing turbine spacing in a row (ranging from 3D to 10D) with the literature.

The energy yield density values for different turbine spacing cases show a decreasing trend. A larger surface of a wind farm increases the operational area for maritime transport and can lead to longer installation and maintenance work times.

Simulations of different turbine hub heights, equal to 78 m, 90 m, 102 m, and 109 m were conducted in order to determine the annual electricity production impact of increased turbine heights and to verify the simulation settings. It was expected to get an increasing AEP trend with increasing turbine hub heights and such a relation was obtained. An AEP increase of 3.7% for the 109 m turbine compared to the base case 90 m turbine was obtained.

For the 90 m, 102 m, and 109 m turbine hub heights, a simulation of platform motions was done in order to make sure, that increasing the hub height, thus increasing the substructure center of mass and its movements, does not make the platform unstable and the mooring lines break. Based on the obtained results, and their comparison to the NREL semi-submersible platform definition document, the platform maintained its stability, and the mooring lines maintained their integrity for all of the simulated turbine hub heights. Additionally, the moments exerted on the turbine base were simulated in order to analyze the impact of increased turbine heights on them. It can be noticed, that the moments in the $x$- and $y$-direction on the turbine tower base significantly increase in 102 m and 109 m turbine height cases. Increased tower base moments, escalate the fatigue on the turbine towers, which may lead to a decreased lifetime of the farm, or increased maintenance expenditures. The exact turbine tower fatigue analysis and its impact are not quantitatively determined in this thesis, so further analysis may be required.

Different variations of turbine hub heights in a row showed small differences in terms of the energy wake losses. the lowest energy wake losses were obtained for the highest differences in consecutive turbine hub height configurations (109m_78m, 102m_78m, and 109m_90m), which means that the wake losses reduction can be obtained by varying the turbine hub heights in the farm. However, this reduction of the wake losses is too small to make a significant power generation difference in the simulated cases. Additionally, the turbine material CAPEX savings are too low to compensate for the decreased energy yield of the lowered turbines. Another important aspect in terms of turbine hub height differentiation, that needs to be addressed, is the manufacturing process of the turbines. As the industry is moving towards the automation of all of the processes, including turbine tower manufacturing, large assembly and manufacturing systems would need to be reprogrammed and readjusted to different tower heights. This could increase the production time and costs of the turbines for a wind farm.

Two different wind farm layouts were considered: i) a diamond and ii) a dephased configuration. The wind farm layouts' results showed considering improvements regarding the AEP and LCOE. A slight dephase (equal to 2 rotor diameters) of the second and third turbine from the row center-line can decrease the LCOE values by up to 14.3%. The energy wake losses were significantly decreased down to 6.1% and 5.1% for the diamond and dephased layouts, which corresponds to the wake losses decrease of the 10D - 12D turbine spacing. The energy yield density results showed a substantially higher value for the diamond layout compared to the dephased one. It is due to the fact, that the diamond layout reduces the turbine rows length by placing WT2 and WT3 at the same $y$-direction distance, reducing the total wind farm area. As the wake losses, LCOE, and capacity factor values differences between the two layouts were small and the energy yield density values were definitely higher for the diamond layout, it may be stated that the diamond wind farm layout compared to the base case and dephased layout is more better compared to the other studied wind farm layouts.

Increasing the distance of the WT2 and WT3 turbines from the row center-line significantly reduces the wake losses, even down to 1.6% for the 4R-dephasing compared to the base case 18.7%. A significant reduction in the LCOE can be noticed with 16% and 17.2% for the dephased_3R and dephased_4R cases. The wake losses present a similar, non-linear trend to the turbine spacings simulation cases set, with insignificant wake losses differences between the 3R- and 4R-dephasing. It is expected that the wake losses reduction will become so small, that the increasing expenditures caused by larger farm areas will surpass the AEP gains from further turbine dephasing. As the LCOE, wake losses, and capacity factor differences between the 3R and the 4R case are negligible and the energy yield differences are significant, a dephasing distance of about 3R is recommended.

The turbine spacing increase for the dephased turbine simulation cases resulted in negligible wake losses, LCOE, and CF differences, however, the energy yield density decreased significantly with the increasing spacing distance. Based on the above, the turbine spacing does not influence the performance and LCOE reduction of the wind farm when considering the dephased wind farm layouts, and the most cost-efficient configuration analyzed in this set of cases is the 4.3D_Dephased_2R one.

Based on an estimation done in regards to the platform size reduction, down-scaling of the floating platform may not have a high impact on the LCOE. The estimation done, using the cost model in this thesis, shows a 3.4% of LCOE decrease for a 10% platform size reduction. Furthermore, such a reduction of the platform size may significantly impact the platform dynamics and may lead to platforms' destabilization, especially when considering higher turbine hub heights and greater weight.

This study provides a good base for further, commercial analysis of different wind farm configurations, including the wind turbine row spacings, turbine hub heights, and wind farm layouts. Compared to the other theses and articles on this subject, it covers a wider range of possible wind farm configurations and addresses different wind farm evaluation factors.

### Recommendations for the future work

Based on the above conclusions, it is recommended to look into different wind farm layouts that could provide lower energy wake losses and LCOE values.

The introduced energy yield density factor can be further researched and used in the future in order to evaluate different wind farm layouts in regards to their surface area, and its implications in maritime spatial planning.

As the cost model used in this thesis is based on literature approximations, a commercially-based and publicly-available model, developed and supported by leading floating offshore wind farms' manufacturers and installers, could be created, in order to enable a more extensive scientific analysis.

In order to minimize the impact of the wake losses induced by the turbines in the other rows, the far dephased turbines in every row were placed at a vertical distance of 3.3D (based on the reference case) between each other. It may be possible to decrease the distance between the subsequent rows, thus decreasing the area of the farm, and LCOE and increasing the energy yield density. In order to achieve that, further analysis needs to be done, that simulates the wake effects of a complete farm to determine the minimal distance between the turbine rows for which subsequent rows are not affected by the wake of the other ones.

# Bibliography

[1] H.-O. Pörtner et al. *Climate Change 2022: Impacts, Adaptation, and Vulnerability. Contribution of Working Group II to the Sixth Assessment Report of the Intergovernmental Panel on Climate Change*. 2022.

[2] D. Resnik. *Climate Change: Causes, Consequences, Policy, and Ethics*. Mar. 2016, pp. 47–58. DOI: 10.1007/978-3-319-26167-6_4.

[3] H. Ritchie and M. Roser. “CO2 and Greenhouse Gas Emissions”. In: *Our World in Data* (2020). URL: https://ourworldindata.org/co2-and-other-greenhouse-gas-emissions.

[4] W. Lamb et al. “A review of trends and drivers of greenhouse gas emissions by sector from 1990 to 2018”. In: *Environmental Research Letters* 16 (July 2021). DOI: 10.1088/1748-9326/abee4e.

[5] IRENA. *Innovation landscape for a renewable-powered future: Solutions to integrate variable renewables*. 2019. URL: https://www.irena.org/publications/2019/Feb/Innovation-landscape-for-a-renewable-powered-future.

[6] United Nations. *Paris Agreement to the United Nations Framework Convention on Climate Change*. Dec. 2015. URL: https://www.un.org/en/climatechange/paris-agreement.

[7] United Nations. *Sustainable Development Goals*. URL: https://sdgs.un.org/goals.

[8] United Nations. *Theme Report on Energy Transition: : Towards the Achievement of SDG 7 and Net-zero Emissions*. Sept. 2021.

[9] IRENA. *Future of wind: Deployment, investment, technology, grid integration and socio-economic aspects (A Global Energy Transformation paper)*. 2019. URL: https://www.irena.org/publications/2019/Oct/Future-of-wind.

[10] V. N. Dinh and E. McKeogh. “Offshore Wind Energy: Technology Opportunities and Challenges”. In: *Proceedings of the 1st Vietnam Symposium on Advances in Offshore Engineering*. Ed. by M. F. Randolph et al. Singapore: Springer Singapore, 2019, pp. 3–22.

[11] J. Lee et al. *Global Offshore Wind Report 2021*. Sept. 2021.

[12] D. Zheng and S. Bose. *Offshore wind turbine design*. 2010. Chap. 11. DOI: 10.2495/978-1-84564-205-1/11.

[13] L. Cozzi et al. *Offshore Wind Outlook 2019*. Tech. rep. IEA, 2019. URL: https://www.iea.org/reports/offshore-wind-outlook-2019.

[14] R. Ramachandran et al. *Floating offshore wind turbines: Installation, operation, maintenance and decommissioning challenges and opportunities*. Oct. 2021. DOI: 10.5194/wes-2021-120.

[15] M Leimeister, A Kolios, and M Collu. “Critical review of floating support structures for offshore wind farm deployment”. In: *Journal of Physics: Conference Series* 1104 (Oct. 2018). DOI: 10.1088/1742-6596/1104/1/012007.

[16] W. Musial, P. Spitsen, and P. Beiter. *Offshore Wind Market Report: 2021 Edition*. U.S. Department of Energy, Office of Energy Efficiency and Renewable Energy, Wind Energy Technologies Office, by NREL.

[17] International Renewable Energy Agency (IRENA). *Renewable Power Generation Costs in 2020*. 2021.

[18] Akselos. *Akselos contracted by Shell and RWE to model Tetraspar Demonstrator*. Accessed: 31-10-2022. URL: https://www.akselos.com/news-detail/akselos-contracted-by-shell-and-rwe-to-model-tetraspar-demonstrator.

[19] General Electric. *GE Renewable Energy and TNO to test new research on blade tip improvements aimed at reducing levelized cost of energy (LCOE) of offshore wind power*. Accessed: 31-10-2022. URL: https://www.ge.com/news/press-releases/ge-renewable-energy-and-tno-test-new-research-blade-tip-improvements-aimed-reducing-lcoe-offshore-wind.

[20] State of Green. *Siemens Gamesa and Danish university to lead EU-funded wind research project*. Accessed: 31-10-2022. URL: https://stateofgreen.com/en/news/siemens-gamesa-and-danish-university-to-lead-eu-funded-wind-research-project/.

[21] J. Jonkman and K. Shaler. *FAST.Farm User’s Guide and Theory Manual*. Accessed: 31-10-2022. 2021. URL: https://www.nrel.gov/docs/fy21osti/78485.pdf.

[22] S. Afewerki. “Firm agency and global production network dynamics”. In: *European Planning Studies* 27 (Mar. 2019), pp. 1–20. DOI: 10.1080/09654313.2019.1588857.

[23] SAIPEM SpA. *HYWIND*. Accessed: 31-10-2022. URL: https://www.saipem.com/en/projects/hywind/.

[24] Z. Jiang. “Installation of offshore wind turbines: A technical review”. In: *Renewable and Sustainable Energy Reviews* 139 (Apr. 2021), p. 110576. DOI: 10.1016/j.rser.2020.110576.

[25] G. E. Barter, A. Robertson, and W. Musial. “A systems engineering vision for floating offshore wind cost optimization”. In: *Renewable Energy Focus* 34 (2020), pp. 1–16. ISSN: 1755-0084. DOI: 10.1016/j.ref.2020.03.002.

[26] E. Dornhelm, H. Seyr, and M. Muskulus. “Vindby—A Serious Offshore Wind Farm Design Game”. In: *Energies* 12 (Apr. 2019), p. 1499. DOI: 10.3390/en12081499.

[27] P. Plodpradit et al. “Suction Bucket Pile–Soil–Structure Interactions of Offshore Wind Turbine Jacket Foundations Using Coupled Dynamic Analysis”. In: *Journal of Marine Science and Engineering* 8 (June 2020), p. 416. DOI: 10.3390/jmse8060416.

[28] Y. Sokona et al. O. Edenhofer R. Pichs-Madruga. “IPCC Special Report on Renewable Energy Sources and Climate Change Mitigation”. In: (2011). ISSN: 978-1-107-60710-1.

[29] A. Shonberg et al. “Suction bucket jackets for offshore wind turbines: applications from in situ observations”. In: (Sept. 2017).

[30] Windfloat. *Floating offshore wind-power generating platform.* Accessed: 31-10-2022. 2021. URL: `https://www.edp.com/en/innovation/windfloat`.

[31] R. James and M. C. Ros. *Floating Offshore Wind: Market and Technology Review*. Prepared for the Scottish Government. June 2015.

[32] The Crown Estate Offshore Renewable Energy Catapult. *Guide to an offshore wind farm Updated and extended*. Apr. 2019.

[33] B. Skousen et al. *Technical Study: MSP as a tool to support Blue Growth. Sector Fiche: Offshore Wind Energy*. Final Version: 16.02.2018.

[34] American Bureau of Shipping. *ABS Guide For Building And Classing Floating Offshore Wind Turbines*. July 2020.

[35] T. Liang et al. “Life Cycle Assessment of Offshore Wind Farm Siting: Effects of Locational Factors, Lake Depth, and Distance from Shore”. In: *Journal of Industrial Ecology* 20.6 (2016), pp. 1370–1383. DOI: `10.1111/jiec.12400`.

[36] M. Roggenburg et al. “Techno-economic analysis of a hydraulic transmission for floating offshore wind turbines”. In: *Renewable Energy* 153 (2020), pp. 1194–1204. ISSN: 0960-1481. DOI: `10.1016/j.renene.2020.02.060`.

[37] European Commission. *A new Circular Economy Action Plan, For a cleaner and more competitive Europe*. Document 52020DC0098, COM/2020/98 final. Mar. 2020.

[38] International Renewable Energy Agency (IRENA). *Renewable capacity statistics 2021*. 2021.

[39] Principle Power Inc. *Kincardine Offshore Wind Farm*. Accessed: 31-10-2022. 2021. URL: `https://www.principlepower.com/projects/kincardine-offshore-wind-farm`.

[40] BW Ideol. *France’s First Offshore Wind Turbine And BW IDEOL’s First Demonstrator Floatgen*. Accessed: 31-10-2022. URL: `https://www.bw-ideol.com/en/floatgen-demonstrator`.

[41] Principle Power Inc. *Korea Floating Wind*. Accessed: 31-10-2022. URL: `https://www.principlepower.com/projects/korea-floating-wind`.

[42] Principle Power Inc. *Redwood Coast offshore Wind Project*. Accessed: 31-10-2022. URL: `https://www.principlepower.com/projects/redwood-coast-offshore-wind-project`.

[43] A. Martinez and G. Iglesias. “Multi-parameter analysis and mapping of the levelised cost of energy from floating offshore wind in the Mediterranean Sea”. In: *Energy Conversion and Management* 243 (2021), pp. 114–416. ISSN: 0196-8904. DOI: `10.1016/j.enconman.2021.114416`.

[44] C. Maienza et al. “A life cycle cost model for floating offshore wind farms”. In: *Applied Energy* 266 (2020), p. 114716. ISSN: 0306-2619. DOI: `10.1016/j.apenergy.2020.114716`.

[45] M. Shields et al. *The Cost and Feasibility of Floating Offshore Wind Energy in the O'ahu Region*. Oct. 2021.

[46] R. Wiser et al. “Expert elicitation survey predicts 37% to 49% declines in wind energy costs by 2050”. In: *Nat Energy* 6 (2021), pp. 555–565. DOI: 10.1038/s41560-021-00810-z.

[47] T. Stehly and P. Duffy. *2020 Cost of Wind Energy Review*. Accessed: 31-10-2022. 2021. URL: https://www.nrel.gov/docs/fy22osti/81209.pdf.

[48] B. H. Bulder et al. *Pathways to potential cost reductions for offshore wind energy*. Jan. 2021.

[49] D. L. Chandler. *A new method boosts wind farms' energy output, without new equipment*. URL: https://news.mit.edu/2022/wind-farm-optimization-energy-flow-0811.

[50] A. Ghigo et al. “Platform Optimization and Cost Analysis in a Floating Offshore Wind Farm”. In: *Journal of Marine Science and Engineering* 8 (Oct. 2020), p. 835. DOI: 10.3390/jmse8110835.

[51] T. Dann and P. Straehl. *Russia & Ukraine: Our Investment Research Views (Morningstar Managed Portfolios)*. URL: https://mp.morningstar.com/en-us/articles/blt47270398e01edf2b/russia-ukraine-our-investment-research-views.

[52] M. Yeghikian et al. “Wind Farm Layout Optimization with Different Hub Heights in Manjil Wind Farm Using Particle Swarm Optimization”. In: *Applied Sciences* 11 (Oct. 2021), p. 9746. DOI: 10.3390/app11209746.

[53] A. P. J. Stanley, A. Ning, and K. Dykes. “Optimization of turbine design in wind farms with multiple hub heights, using exact analytic gradients and structural constraints”. In: *Wind Energy* 22 (2019), pp. 605–619. DOI: 10.1002/we.2310.

[54] M. F. Howland, S. K. Lele, and J. O. Dabiri. “Wind farm power optimization through wake steering”. In: *Proceedings of the National Academy of Sciences* 116.29 (2019), pp. 14495–14500. DOI: 10.1073/pnas.1903680116.

[55] M. Al-Addous et al. “The Significance of Wind Turbines Layout Optimization on the Predicted Farm Energy Yield”. In: *Atmosphere* 11.1 (2020). ISSN: 2073-4433. DOI: 10.3390/atmos11010117.

[56] T. Göçmen et al. “Wind turbine wake models developed at the technical university of Denmark: A review”. In: *Renewable and Sustainable Energy Reviews* 60 (2016), pp. 752–769. ISSN: 1364-0321. DOI: 10.1016/j.rser.2016.01.113.

[57] S. Ivanell. *Wake Structures*. Springer Nature, 2022. Chap. 29, pp. 915–926. ISBN: 978-3-030-31306-7. DOI: 10.1007/978-3-030-31307-4.

[58] N. S. Ghaisas and C. L. Archer. “Geometry-Based Models for Studying the Effects of Wind Farm Layout”. In: *Journal of Atmospheric and Oceanic Technology* 33 (2016), pp. 481–501. DOI: 10.1175/JTECH-D-14-00199.1.

[59] H.Peng et al. “A review of offshore wind farm layout optimization and electrical system design methods”. In: *Journal of Modern Power Systems and Clean Energy* 7.5 (Sept. 2019), pp. 975–986. ISSN: 2196-5420. DOI: 10.1007/s40565-019-0550-5.

[60] A. C. Pillai et al. “Offshore wind farm layout optimization using particle swarm optimization”. In: *Journal of Ocean Engineering and Marine Energy* 4.1 (Feb. 2018), pp. 73–88. ISSN: 2198-6452. DOI: 10.1007/s40722-018-0108-z.

[61] A. Vasel-Be-Hagh and C. L. Archer. “Wind farm hub height optimization”. In: *Applied Energy* 195 (2017), pp. 905–921. ISSN: 0306-2619. DOI: 10.1016/j.apenergy.2017.03.089.

[62] Hexicon. *TwinWind Floating Technology*. URL: https://www.hexicongroup.com/twinwind/.

[63] X1 Wind. URL: https://www.x1wind.com/.

[64] Stiesdal. *Offshore TetraSpar platform*. URL: https://www.stiesdal.com/offshore/.

[65] J. Ledoux, S. Riffo, and J. Salomon. “Analysis of the Blade Element Momentum Theory”. In: *SIAM Journal on Applied Mathematics* 81 (June 2022), pp. 2596–2621. DOI: 10.1137/20M133542X.

[66] G. Schepers. *Pragmatic Models: BEM with Engineering Add-Ons*. Springer Nature, 2022. Chap. 13, pp. 393–436. ISBN: 978-3-030-31306-7. DOI: 10.1007/978-3-030-31307-4.

[67] E. Branlard. “The blade element momentum (BEM) method”. In: *Research Topics in Wind Energy* (Apr. 2017), pp. 181–211. DOI: 10.1007/978-3-319-55164-7_10.

[68] H. Glauert. “Airplane Propellers”. In: *Aerodynamic Theory: A General Review of Progress Under a Grant of the Guggenheim Fund for the Promotion of Aeronautics*. Springer Berlin Heidelberg, 1935, pp. 169–360. ISBN: 978-3-642-91487-4. DOI: 10.1007/978-3-642-91487-4_3.

[69] Emmanuel Branlard. “Momentum Theory”. In: Apr. 2017, pp. 157–180. ISBN: 978-3-319-55163-0. DOI: 10.1007/978-3-319-55164-7_9.

[70] L. Garcia et al. “Experiments in the wind turbine far wake for the evaluation of an analytical wake model”. In: *Journal of Physics: Conference Series* 854 (May 2017). DOI: 10.1088/1742-6569/854/1/012015.

[71] J. N. Sørensen. *Lecture series 2022-05: Aerodynamics of wind turbines: State of the art and future perspectives*. Lecture notes. Karman Institute for Fluid Dynamics, Sept. 2022. Chap. 8.

[72] G. C. Larsen. *Wake Meandering*. 2022. DOI: 10.1007/978-3-030-31307-4.

[73] N. Jensen. “A note on wind generator interaction”. In: 1983.

[74] I. Katic, J. Højstrup, and N.O. Jensen. “A Simple Model for Cluster Efficiency”. In: *EWEC’86. Proceedings. Vol. 1*. Ed. by W. Palz and E. Sesto. European Wind Energy Association Conference and Exhibition, EWEC ’86 ; Conference date: 06-10-1986 Through 08-10-1986. 1987, pp. 407–410.

[75] L. Tian et al. “Development and validation of a new two-dimensional wake model for wind turbine wakes”. In: *Journal of Wind Engineering and Industrial Aerodynamics* 137 (2015), pp. 90–99. ISSN: 0167-6105. DOI: 10.1016/j.jweia.2014.12.001.

[76] J. Schmidt and L. Vollmer. “Industrial Wake Models”. In: *Handbook of Wind Energy Aerodynamics* (2022), pp. 927–954. DOI: 10.1007/978-3-030-31307-4.

[77] P.-E. Réthoré. “Thrust and wake of a wind turbine: Relationship and measurements”. PhD thesis. Jan. 2006.

[78] S. Frandsen et al. “Analytical modelling of wind speed deficit in large offshore wind farms”. In: *Wind Energy* 9.1-2 (2006), pp. 39–53. DOI: 10.1002/we.189.

[79] X. Gao et al. “Comparisons of the accuracy of different wake models in wind farm layout optimization”. In: *Energy Exploration & Exploitation* 38.5 (2020), pp. 1725–1741. DOI: 10.1177/0144598720942852.

[80] B. Witha. “CFD-Type Wake Models”. In: *Handbook of Wind Energy Aerodynamics* (2022), pp. 1001–1038. DOI: 10.1007/978-3-030-31307-4.

[81] G. C. Larsen. “A Simple Wake Calculation Procedure”. In: (1988).

[82] G. C. Larsen. *A simple stationary semi-analytical wake model*. English. Denmark. Forskningscenter Risoe. Risoe-R 1713(EN). Risø National Laboratory for Sustainable Energy, Technical University of Denmark, 2009.

[83] G. C. Larsen et al. *Dynamic wake meandering modeling*. Denmark. Forskningscenter Risoe. Risoe-R 1607(EN). Risø National Laboratory, 2007. ISBN: 978-87-550-3602-4.

[84] I. Reinwardt et al. “Validation of wind turbine wake models with focus on the dynamic wake meandering model”. In: 1037 (June 2018). DOI: 10.1088/1742-6596/1037/7/072028.

[85] National Renewable Energy Laboratory. *OpenFAST Documentation*. Accessed: 31-10-2022. URL: https://openfast.readthedocs.io/en/main/.

[86] U.S. Department of Energy National Renewable Energy Laboratory. *OpenFAST*. Accessed: 31-10-2022. URL: https://www.nrel.gov/wind/nwtc/openfast.html.

[87] I. Katiċ et al. “A simple model for cluster efficiency”. In: *European Wind Energy Association Conference and Exhibition* (1986).

[88] A. Robertson et al. *Definition of the Semisubmersible Floating System for Phase II of OC4*. NREL, Sept. 2014.

[89] J. Jonkman et al. *Definition of a 5-MW Reference Wind Turbine for Offshore System Development*. NREL, Feb. 2009.

[90] YILPORT Holding INC. *Leixoes, Portugal*. Accessed: 31-10-2022. URL: https://www.yilport.com/en/ports/default/Leixoes-Portugal/114/0/0.

[91] Google LLC. *Google Earth*. Accessed: 31-10-2022. URL: https://earth.google.com/.

[92] National Oceanic and Atmospheric Administration. *West Portugal Coast Wind Data*. Accessed: 31-10-2022. URL: https://www.noaa.gov/.

[93] J. C. C. Portillo. “Oscillating-water-columns systems: single devices, arrays, and multi-purpose platforms”. PhD thesis. Instituto Superior Técnico, University of Lisbon, 2022.

[94] C. L. Archer and M. Z. Jacobson. “Spatial and temporal distributions of U.S. winds and wind power at 80 m derived from measurements”. In: *Journal of Geophysical Research: Atmospheres* 108.D9 (2003). DOI: 10.1029/2002JD002076.

[95] M. Argin et al. “Exploring the offshore wind energy potential of Turkey based on multi-criteria site selection”. In: *Energy Strategy Reviews* 23 (2019), pp. 33–46. ISSN: 2211-467X. DOI: `.1016/j.esr.2018.12.005`.

[96] Z. R. Shu and M. Jesson. “Estimation of Weibull parameters for wind energy analysis across the UK”. In: *Journal of Renewable and Sustainable Energy* 13.2 (2021). DOI: `10.1063/5.0038001`.

[97] World Weather. Accessed: 31-10-2022. URL: `https://world-weather.info/archive/portugal/porto/`.

[98] A. Sebastiani et al. “Data analysis and simulation of the Lillgrund wind farm”. In: *Wind Energy* 24.6 (2021), pp. 634–648. DOI: `10.1002/we.2594`.

[99] M. Rentschler et. al. “Parametric study of dynamic inter-array cable systems for floating offshore wind turbines”. In: *Marine Systems & Ocean Technology* 15 (Jan. 2020). DOI: `10.1007/s40868-020-00071-7`.

[100] IEC 61400-1. *Wind turbine generator systems-Part 1: Safety requirements*. 2nd edition, Geneva, Switzerland. 1999.

[101] B. J. Jonkman. *TurbSim User’s Guide: Version 2.00, Draft version*. Accessed: 31-10-2022. 2014. URL: `https://www.nrel.gov/wind/nwtc/assets/downloads/TurbSim/TurbSim_v2.00.pdf`.

[102] W. J. Pierson Jr. and L. Moskowitz. “A proposed spectral form for fully developed wind seas based on the similarity theory of S. A. Kitaigorodskii”. In: *Journal of Geophysical Research (1896-1977)* 69.24 (1964), pp. 5181–5190. DOI: `10.1029/JZ069i024p05181`.

[103] K. Hasselmann and D. Olbers. “Measurements of wind-wave growth and swell decay during the Joint North Sea Wave Project (JONSWAP)”. In: *Ergänzung zur Deut. Hydrogr. Z., Reihe A (8)* 12 (1973), pp. 1–95.

[104] D. Cevasco, S. Koukoura, and A. J. Kolios. “Reliability, availability, maintainability data review for the identification of trends in offshore wind energy applications”. In: *Renewable and Sustainable Energy Reviews* 136 (2021), p. 110414. ISSN: 1364-0321. DOI: `10.1016/j.rser.2020.110414`.

[105] A. Papadopoulos et. al. *Collection and transmission losses of offshore wind farms for optimization purposes*. 2015, pp. 6724–6732. DOI: `10.1109/ECCE.2015.7310601`.

[106] A. Castorrini et al. “Assessing wind turbine energy losses due to blade leading edge erosion cavities with parametric CAD and 3D CFD”. In: *Journal of Physics: Conference Series* 1618 (Sept. 2020). DOI: `10.1088/1742-6596/1618/5/052015`.

[107] J. Lappalainen. “Economic Potential of Offshore Wind Energy in the Gulf of Bothnia”. English. Master’s thesis. Aalto University. School of Electrical Engineering, 2019. URL: `http://urn.fi/URN:NBN:fi:aalto-201903172314`.

[108] RECHARGE News. Accessed: 31-10-2022. URL: `https://www.rechargenews.com/wind/were-all-in-trouble-wind-turbine-makers-selling-at-a-loss-and-in-a-self-destructive-loop-bosses-admit/2-1-1197217`.

[109] salary.com. *SBM Offshore Hourly Pay Rate*. Accessed: 31-10-2022. URL: https://www.salary.com/research/company/hourly-wage-for-sbm-offshore.

[110] Porto de Leixões. *Port Administration Tariffs*. Accessed: 31-10-2022. URL: http://www.apdl.pt/tarifas.

[111] L. Miranda, M. Mueller-Stoffels, and E. Whitney. "An Alaska case study: Electrical transmission". In: *Journal of Renewable and Sustainable Energy* 9 (Nov. 2017). DOI: 10.1063/1.4986582.

[112] H. Kekana and G. Landwehr. "Wind capacity factor calculator". In: *Journal of Energy in Southern Africa* 30.2 (June 2019), pp. 118–125. DOI: 10.17159/2413-3051/2019/v30i2a6451.

[113] R. J. Barthelmie et. al. "Modelling and measuring flow and wind turbine wakes in large wind farms offshore". In: *Wind Energy* 12.5 (2009), pp. 431–444. DOI: 10.1002/we.348.

[114] A. Al-Hinai, Y. Charabi, and K. S. H. Aghay. "Offshore Wind Energy Resource Assessment across the Territory of Oman: A Spatial-Temporal Data Analysis". In: *Sustainability* 13.5 (2021). ISSN: 2071-1050. DOI: 10.3390/su13052862.

[115] J. A. Sainz. "New Wind Turbine Manufacturing Techniques". In: *Procedia Engineering* 132 (Dec. 2015), pp. 880–886. DOI: 10.1016/j.proeng.2015.12.573.